

2015-01-01

# Hybrid Nano-Structure For Enhanced Energy Storage Devices

Mohammad Arif Ishtiaque Shuvo

*University of Texas at El Paso, mishuvo@miners.utep.edu*

Follow this and additional works at: [https://digitalcommons.utep.edu/open\\_etd](https://digitalcommons.utep.edu/open_etd)



Part of the [Materials Science and Engineering Commons](#), and the [Mechanics of Materials Commons](#)

---

## Recommended Citation

Shuvo, Mohammad Arif Ishtiaque, "Hybrid Nano-Structure For Enhanced Energy Storage Devices" (2015). *Open Access Theses & Dissertations*. 1158.

[https://digitalcommons.utep.edu/open\\_etd/1158](https://digitalcommons.utep.edu/open_etd/1158)

This is brought to you for free and open access by DigitalCommons@UTEP. It has been accepted for inclusion in Open Access Theses & Dissertations by an authorized administrator of DigitalCommons@UTEP. For more information, please contact [lweber@utep.edu](mailto:lweber@utep.edu).

# HYBRID NANO-STRUCTURE FOR ENHANCED ENERGY STORAGE DEVICES

MOHAMMAD ARIF ISHTIAQUE SHUVO

Environmental Science and Engineering Doctoral Program

APPROVED:

---

Yirong Lin, Ph.D., Chair

---

Juan C. Noveron, Ph.D.

---

Norman D. Love, Ph.D.

---

David A. Roberson, Ph.D.

---

Charles Ambler, Ph.D.  
Dean of the Graduate School

Copyright ©

by

Mohammad Arif Ishtiaque Shuvo

2015

## **Dedication**

To my parents and my wife.

HYBRID NANO-STRUCTURE FOR ENHANCED ENERGY STORAGE  
DEVICES

by

MOHAMMAD ARIF ISHTIAQUE SHUVO, M.S.

DISSERTATION

Presented to the Faculty of the Graduate School of  
The University of Texas at El Paso  
in Partial Fulfillment  
of the Requirements  
for the Degree of

DOCTOR OF PHILOSOPHY

Environmental Science and Engineering Doctoral Program

THE UNIVERSITY OF TEXAS AT EL PASO

December 2015

## **Acknowledgements**

At first I want to thank Department of Mechanical Engineering and Center for Space Exploration & Energy Research Center (cSETER), National Science Foundation (NSF), Pacific Northwest National Lab (PNNL) and Department of Energy (DOE) NETL for providing all kinds of support for pursuing my doctoral degree. I want to convey my special thanks to my advisor, Dr. Yirong Lin, for his continuous effort to make my way easier as a graduate student. His continuous monitoring and advising have enabled me to complete my doctoral degree in only three years. I would also like to thank Dr. Vijay Murugesan, Dr. Manjula Nandisiri, and Ashleigh M. Schwarz from PNNL for his intellectual contribution and other supports for this research. Special thanks to Dr. Noveron, Dr. Love and Dr. Roberson for serving as my committee members. Special thanks to all members from Dr. Noveron's lab. I would like to thank Dr. Peter Cook from New Mexico State University (NMSU) and Dr. Sudhir from UTEP chemistry department for TEM support. Special thanks to Mr. Tarek and Ms. Tahmina for supporting the research in many ways. I want to convey my thanks to my fellow mates, i.e. Mr. Gerardo, Mr. Ivan, Mr. Karim, Mr. Sarker, Mr. Delfin, Mr. Luis, Mr. Jose, Mr. Hossain, Mr. Jose Gonzalez, Mr. Rajib, Mr. Khan, & all other members. They always inspired me and helped in different situations of research. At last I want to thank all my friends and family members for providing me courage & enthusiasm for the completion of my doctoral degree.

## **Abstract**

The goal of this research is to develop electrode materials using various nano-structure hybrids for improved energy storage devices. Enhancing the performance of energy storage device has been gaining tremendous attention since it holds the key solution to advance renewable energy usage thus reduce the consumption of fossil fuels. The application of energy storage devices such as super-capacitor and Li-ion-battery has seen significant growth; however, it is still limited mainly by charge/discharge rate and energy density. One of the solutions is to use nano-structure materials, which offer higher power at high energy density and improved stability during the charge discharge cycling of ions in and out of the storage electrode material. In this research, carbon-based materials (e.g. porous carbon, graphene) in conjunction with metal oxides such as CeO<sub>2</sub> nanoparticles/TiO<sub>2</sub> nanowires are synthesized utilizing low temperature hydrothermal method for the fabrication of advanced electrode materials. Scanning Electron Microscopy (SEM), Transmission Electron Microscopy (TEM), X-ray Diffraction (XRD), Thermogravimetric Analysis (TGA), X-ray Photoelectron Spectroscopy (XPS), and Fourier Transformation Infrared Spectroscopy (FTIR) were used for materials characterization. Potentiostat, battery analyzer, and Electrochemical Impedance Spectroscopy (EIS) were used for evaluating the electrochemical performance. The testing results have shown that a maximum 500% higher specific capacitance could be obtained using porous carbon/CeO<sub>2</sub> instead of porous carbon for super-capacitor application and microwave exfoliated graphene oxide/TiO<sub>2</sub> nanowire hybrid provides up to 80% increment of specific capacity compared to porous carbon anode for Li-ion-battery application.

## Table of Contents

Acknowledgements.....	v
Abstract.....	vi
Table of Contents.....	vii
List of Figures.....	viii
Chapter 1: Introduction.....	1
1.1 Super-capacitor.....	1
1.2 Lithium Ion Battery.....	15
Chapter 2: Fabrication and Assembly.....	29
2.1 Electrode Fabrication for Super-capacitor.....	29
2.2 Super-capacitor Assembly.....	33
2.3 Electrode Fabrication for Lithium-ion-battery.....	35
2.4 Lithium-ion-battery Assembly.....	41
Chapter 3: Super-capacitor.....	44
3.1 Characterization.....	44
3.2 Testing and Discussion.....	54
Chapter 4: Lithium Ion Battery.....	71
4.1 Characterization.....	71
4.2 Testing and Discussion.....	77
Chapter 5: Conclusion.....	85
5.1 Super-capacitor.....	85
5.2 Lithium Ion Battery.....	86
References.....	89
Vita.....	95



## List of Figures

Figure 1.1: Schematic diagram of a conventional capacitor [20].	2
Figure 1.2: Schematic diagram of a conventional super-capacitor [20].	4
Figure 1.3: Ragone plot of energy storage devices [20].	5
Figure 1.4: Super-capacitor classification [20].	6
Figure 1.5: Electric double layer--charged and discharged states [23].	7
Figure 1.6: Comparison of typical electrolyte properties [21].	9
Figure 1.7: Properties of most common carbon materials used as electrode in EDLCs [21].	10
Figure 1.8: Example of Heading 8,h8 format [23].	11
Figure 1.9: Working principle of LIB (charging).	16
Figure 1.10: Commercial lithium-ion battery	17
Figure 1.11: Schematic open-circuit energy diagram of an aqueous electrolyte. $\phi_A$ and $\phi_C$ are the anode and cathode work functions. Eg is window of the electrolyte for thermodynamic stability. A $\mu_A > \text{LUMO}$ and/or a $\mu_C > \text{HOMO}$ requires a kinetic stability by the formation of an SEI Layer [62].	18
Figure 1.12: Non-aqueous electrolytes in LIBs [62].	19
Figure 1.13: (a) Availability and (b) capacities of elements that may host Li as electrodes [63].	22
Figure 1.14: Approximate range of average discharge potentials and specific capacity of some of the most common (a) intercalation-type cathodes (experimental), (b) conversion-type cathodes (theoretical), (c) conversion type anodes (experimental), and (d) an overview of the average discharge potentials and specific capacities for all types of electrodes [63].	23
Figure 2.1: Schematic illustration of porous carbon/ $\text{CeO}_2$ nanoparticle synthesis.	30
Figure 2.2: Two-electrode test cell configuration.	32
Figure 2.3: Schematic view of coin cell assembly.	33
Figure 2.4: Schematic view of coin cell assembly.	34
Figure 2.5: Schematic view of coin cell assembly.	36
Figure 2.6: Schematic illustration of porous carbon/ $\text{CeO}_2$ nanoparticle synthesis.	37
Figure 2.7: Schematic view of anode preparation.	40
Figure 2.8: Schematic view of anode preparation.	41
Figure 2.9: Schematic view of coin cell assembly.	42
Figure 2.10: Schematic view of coin cell assembly.	43
Figure 3.1: SEM of PC-CON sample.	45
Figure 3.2: SEM images, (a, b, and d) ZnO/Carbon Fiber, (c) Bare carbon fiber.	46
Figure 3.3: (a) SEM image of $\text{CeO}_2$ nanoparticles on porous carbon, (b) morphology of porous carbon, (c-d) TEM & HRTEM images of $\text{CeO}_2$ nanoparticles.	47
Figure 3.4: XRD results for PC-CON before and after heat treatment.	48
Figure 3.5: XRD result for ZnO NWs coated carbon cloth. Asterisk (*) peak is for carbon. The rest of the peaks belong to ZnO.	49
Figure 3.6: TGA of PC-CON sample.	50
Figure 3.7: High resolution XPS spectrum of Ce 3d for before and after testing electrodes.	51
Figure 3.8: XPS Ce 3d spectra of before testing electrode.	52
Figure 3.9: XPS Ce 3d spectra of after testing electrode.	53

Figure 3.10: EZ-stat for electrochemical testing.....	54
Figure 3.11: LCR meter used for electrochemical impedance spectroscopy. ....	55
Figure 3.12: Cyclic voltammetry of an EDLC super-capacitor [21]. ....	56
Figure 3.13: CV curves of PC and PC-CON at a scan rate of 50 mV/s.....	57
Figure 3.14: CV curves of PC and PC-CON at a scan rate of 100 mV/s.....	58
Figure 3.15: CV curves of PC-CON at different scan rates.....	59
Figure 3.16: Average specific capacitance of PC and PC-CON at different scan rates. ....	60
Figure 3.17: Cycling performance of PC and PC-CON electrodes at different scan rates. ....	61
Figure 3.18: Galvanostatic charge discharge curve for a super-capacitor. Inset: zoom-in of the current inversion region [17]. ....	62
Figure 3.19: Galvanostatic charge/discharge curves of PC and PC-CON at a current density of 0.5 A/g.....	64
Figure 3.20: Galvanostatic charge/discharge curves of PC-CON at different current densities. .	65
Figure 3.21: Typical cyclic voltammograms of (a) CF (b) CF-Au (c) CF-ZnO (d) CF-ZnO-Au electrode super-capacitor & galvanostatic charge discharge curve at 56 $\mu$ A within a voltage window of 0-0.5 V for (e) CF (f) CF-Au (g) CF-ZnO (h) CF-ZnO-Au electrode super-capacitor. .....	66
Figure 3.22: Stationary polarization curve (black bold line). A sinusoidal voltage is imposed over the steady state voltage and the resulting current is measured. A measurement is made at different frequency ( $f = \omega 2 \pi$ ) [21]. ....	67
Figure 3.23: Nyquist plot for PC-CON sample. ....	69
Figure 3.24: PC-CON equivalent circuit of EIS. ....	69
Figure 3.25: Nyquist plot for PC-CON sample. ....	70
Figure 4.1: SEM image of (a) MEGO, (b) PC, (c-d) MEGO-TON hybrid. ....	72
Figure 4.2: SEM images (a-b) Graphene Aerogel, (c-d) Graphene Aerogel with ZnO nanowire.	73
Figure 4.3: XRD result for MEGO-TON hybrid. ....	74
Figure 4.4: FTIR spectra of GO and MEGO. ....	76
Figure 4.5: MTI 8-channel battery analyzer. ....	77
Figure 4.6: Measurements of capacity and rate capability, (a) charge/discharge curve for PC electrode, (b) charge/discharge curve for MEGO-TON hybrid electrode, (c) comparison of specific capacity of the two anode materials as a function of cycle number: PC and MEGO-TON anode were cycled at 100mA/g, 200mA/g, 300mA/g, and 500 mA/g current density respectively for 40 cycles. ....	79
Figure 4.7: Measurements of capacity and rate capability, (a) charge/discharge curve for PC anode, (b) charge/discharge curve for PC-CON anode, (c) comparison of specific capacity of the two anode materials as a function of cycle number: PC anode was cycled at 100 for 40 cycles; PC-CON was varied among 100mA/g, 200mA/g, 300mA/g and 500mA/g consecutively after every 5 cycles (d) cycling performance of PC anode at 100mA/g for 40 cycles (e) specific capacity of PC CON at 100mA/g, 200mA/g, 300mA/g and 500mA/g consecutively after every 5 cycles.....	81
Figure 4.8: Measurements of capacity and rate capability. (a) charge/discharge curve for GA anodes (b) charge/discharge curve for GA with ZnO nanowires anode (c) comparison of specific capacity of the two anode materials as a function of cycle number. ....	83

## **Chapter 1: Introduction**

The present fossil fuel based economy is at a serious risk due to various factors, including the continuous demand of oil, the depletion of non-renewable resources and dependency on foreign oil and/or gas which creates national vulnerabilities that endanger social stability [1]. Another drawback for the fossil fuel usage is associated with the greenhouse gases (GHG) emissions, in particular CO<sub>2</sub> emissions which have been increasing at a constant rate causing the global temperature rise and climate changes. Renewable Energy Sources (RES), i.e. solar, wind, hydropower, geothermal, biomass, and marine energies, are considered as a means of reducing the use of fossil fuels [2-4]. They are the primary, domestic, and clean or inexhaustible energy sources. These sources require energy storage. Hence, developing high energy density energy storage device is the probable key solution for the utilization of alternative energy and thus for the replacement of fossil fuels and traditional energy sources. Therefore, there is an increasing demand for low cost, environment friendly, portable, and high performance energy storage/conversion systems. Numerous researches have been going on for the technological improvements in electrochemical energy storage devices such as batteries [5-10], capacitor [11-15], and super-capacitors [16-19]. The motivation of this research lies in the development of unique architectural electrode materials for next generation energy storage devices, i.e., super-capacitor and lithium-ion-battery, by optimizing the performance and lifetime of the devices.

This chapter discusses the scientific fundamentals of these two types of energy storage devices followed by a literature overview on recent technological development. The motivation of this research is also explained in later portion of this chapter.

### **1.1 Super-capacitor**

#### **1.1.1 Capacitor Principle**

Capacitor, originally known as condenser, is an energy storage device comprised of two electrodes separated by a dielectric material. When voltage is applied between the two electrodes,

static electric field is formed between the dielectric material causing positive and negative charges to get separated between two electrodes this storing energy. A schematic diagram for a conventional capacitor is shown in Figure 1.1.

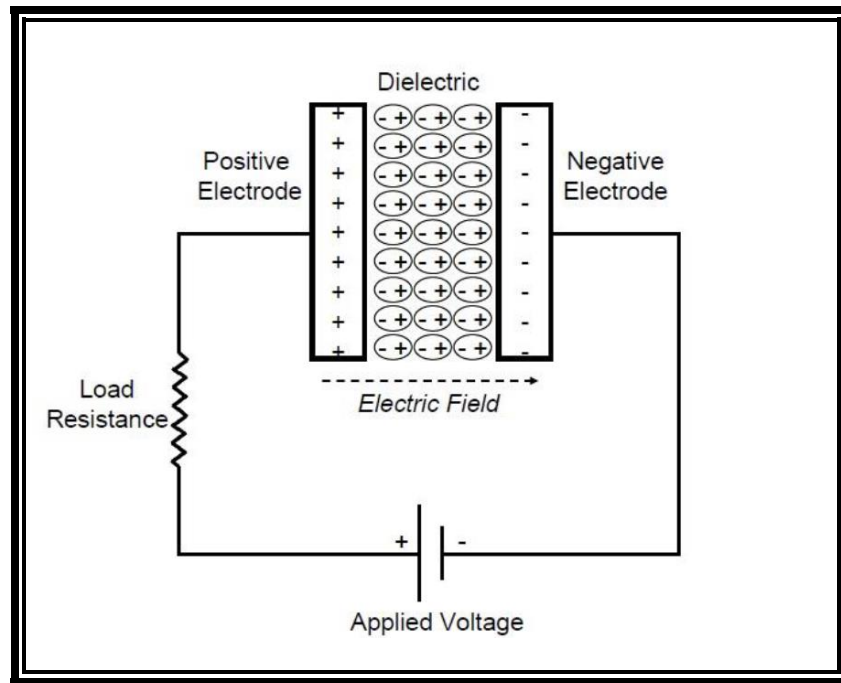


Figure 1.1: Schematic diagram of a conventional capacitor [20].

A dielectric capacitor is an energy storage device of simple construction. It is typically composed of two parallel plates and a dielectric medium in between the plates; its unit of measure is capacitance equal to 1 Farad per meter (F/m). There are several relationships that characterize and are characterized by the definition of capacitance. Capacitance ( $C$ ) is the ability of a material to store an electrical charge. In a parallel plate dielectric capacitor, capacitance can be described as the amount of charge ( $Q$ ) stored in the parallel plates with respect to the existing voltage ( $V$ ) between those plates.

$$C = Q/V$$

Capacitance ( $C$ ) is directly proportional to the area ( $A$ ) of the parallel plates (or electrodes), and inversely proportional to the distance ( $D$ ) between the electrodes:

$$C = \epsilon_0 \epsilon_r \frac{A}{D}$$

where  $\epsilon_0$ , is the permittivity of free space (vacuum) and it is a physical constant approximately equal to  $8.854 \times 10^{-12}$  Farads per meter (F/m). The relative permittivity is represented by  $\epsilon_r$ , which is the factor by which the electric field between the charges is decreased or increased relative to vacuum, thus it is also the ratio of the capacitance of a capacitor using a dielectric medium versus a similar capacitor that has free space only between the plates. The relative permittivity ( $\epsilon_r$ ) is also commonly known as the dielectric constant ( $k$ ), especially in the field of engineering. Therefore, there are three main factor which determine the capacitance of a capacitor:

- Area of the electrode
- Separation distance between the electrode
- Properties of the dielectric material

Energy will be stored in the capacitor when a voltage is applied between the two parallel plates, causing a separation of charges which is responsible for a net build-up of charges on both plates; resulting in a positively charged plate and a negatively charged plate whose charges now have the capability to do work once they are discharged. The energy stored in a capacitor can be described by the following relationship:

$$E = \frac{1}{2} CV^2$$

Maximum energy can be obtained when the  $V$  is at a maximum, which is also limited by the breakdown property of the separation material.

Rate of energy which can be delivered per unit time is known as the power( $P$ ). For a conventional capacitor: The internal components of the capacitor (e.g., current collectors, electrodes, and dielectric material), which is measured in aggregate by a quantity known as the equivalent series resistance (ESR), needs to be taken into account in order to determine ( $P$ ) for a

certain capacitor. The voltage during discharge is determined by these resistances. When measured at matched impedance ( $R = ESR$ ), the maximum power  $P_{max}$  for a capacitor is given by [21]:

$$P_{max} = \frac{V^2}{4 \times ESR}$$

### 1.1.2 Super-capacitor Construction

Super-capacitors are constructed from two high surface area carbon-based electrodes, an electrolyte and a separator (Figure 1.2). Thus super-capacitors utilize high surface area electrode materials and thin electrolytic dielectrics to achieve capacitances several orders of magnitude larger than conventional capacitors, in doing so, super-capacitors are able to attain greater energy densities while still maintaining the characteristic high power density of conventional capacitors [21, 22].

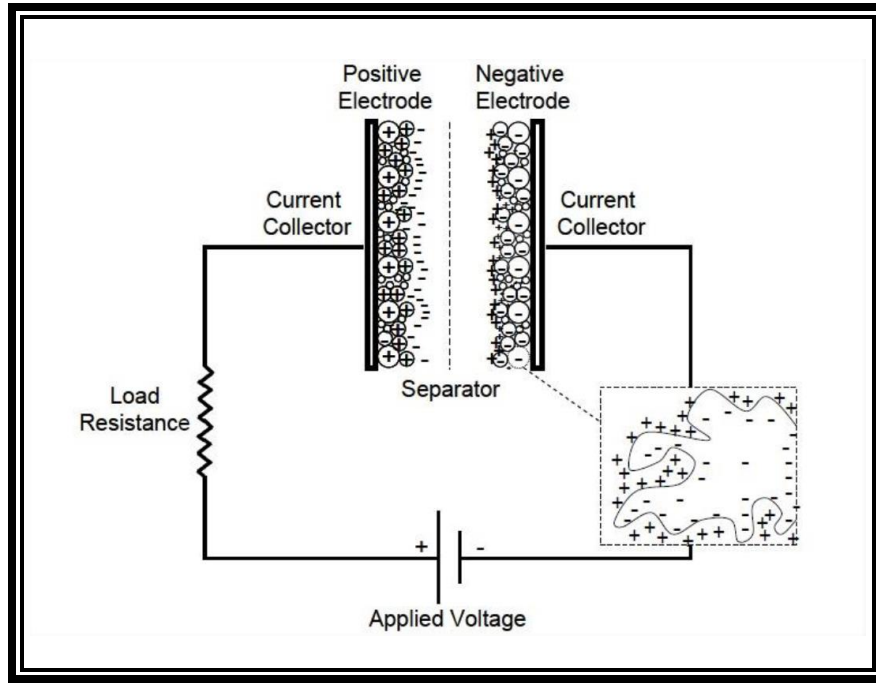


Figure 1.2: Schematic diagram of a conventional super-capacitor [20].

Super-capacitors and general capacitors are governed by same basic working principle and are suitable for rapid storage and release of energy. But, super-capacitors have electrodes with

much higher surface area and thinner dielectrics (thickness of double layer) and therefore, from the equations described above, this leads to an increase in both capacitance and energy, by a factor of 10000 or so than those achievable by regular capacitors. Super-capacitors bridge the significant performance gap between regular capacitors and batteries, as can be seen in Figure 1.3. Additionally, super-capacitors have several advantages over electrochemical batteries and fuel cells, including higher power density, shorter charging times, and longer cycle life and shelf life. Super-capacitors are also often referred to by a number of alternative names including electrochemical double layer capacitors, ultra-capacitors, power capacitors, gold capacitors, pseudo-capacitors, and power cache, however, these names are often given by different companies or brands regardless of their storage mechanism. NEC (Japan) was the first to produce commercial super-capacitor in the 1970s, while Pinnacle Research Institute first introduced super-capacitor in USA in the 1980s under the name “PRI Ultra-capacitor” [21].

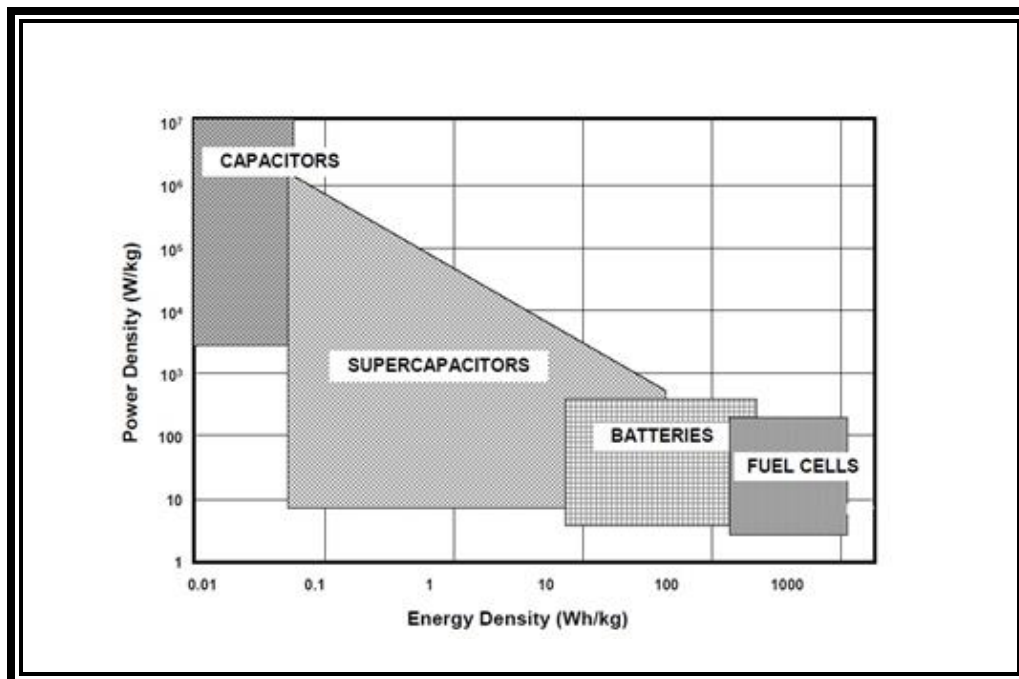


Figure 1.3: Ragone plot of energy storage devices [20].

### 1.1.3 Super-capacitor Classification

Based upon current research and development trends, super-capacitors can be divided into three general classes: electrochemical double-layer capacitors (EDLC), pseudo-capacitors, and hybrid capacitors; each class is characterized by its unique mechanism for storing charge [21]. These are, respectively, non-Faradaic, Faradaic, and a combination of the two [21]. Faradaic processes, such as oxidation-reduction reactions, involve the transfer of charge between electrode and electrolyte. A non-Faradaic mechanism, by contrast, does not use a chemical mechanism, rather, charges are distributed on surfaces by physical processes that do not involve the making or breaking of chemical bonds [21].

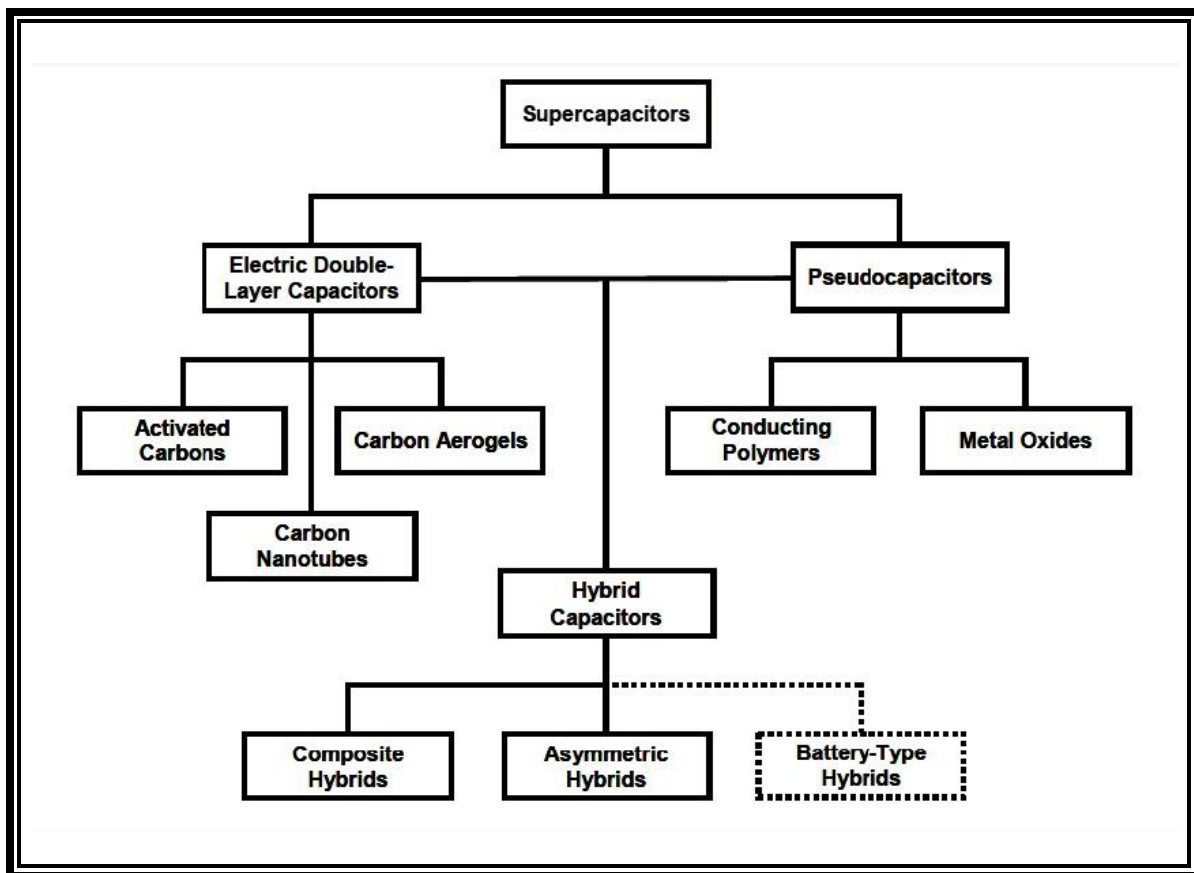


Figure 1.4: Super-capacitor classification [20].



Super-capacitors use electrostatic double-layer capacitance or electrochemical pseudo-capacitance or a combination of both instead and they do not have a conventional solid dielectric. The EDLC is the most widely used super-capacitor which is dominating the market. Various forms of carbon based materials are used for the electrode materials in commercial super-capacitor.

#### 1.1.4 Electric Double Layer Capacitor (EDLC)

Carbon based electrodes, electrolytes & a separator constitutes this kind of capacitor as shown in Figure 1.2. This kind of capacitor stores charges electro-statically without having any chemical bond formation between electrodes and electrolytes during charge and discharge or in short it follows a non-faradic process for energy storage. When voltage is applied, opposite charges accumulate on the electrode surface and complementary ions from the electrolytes diffuse into the electrodes but they don't form any chemical bond. Therefore, EDLC has higher reverse cycling ability ( $10^6$  cycles) compared to batteries ( $10^3$  cycles). That is why it can be used in remote areas where maintenance is tough such as deep sea, mountain, and desert [21].

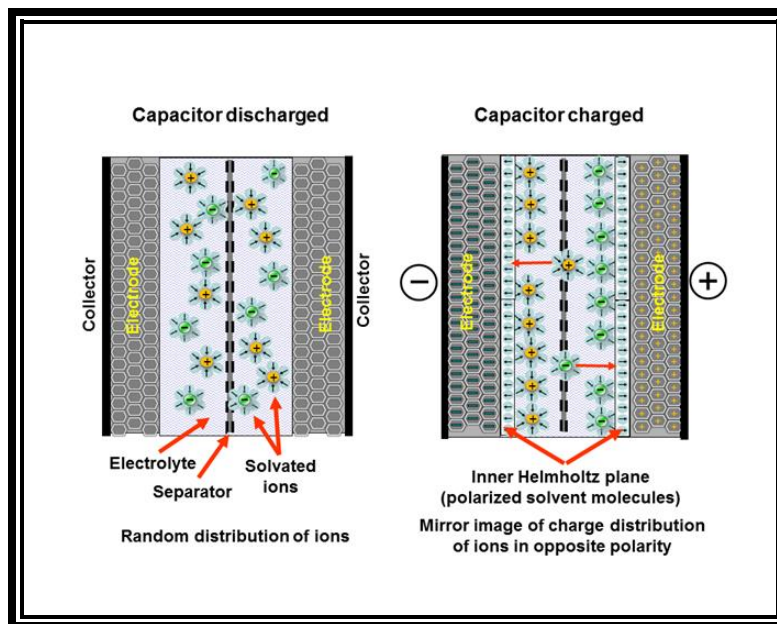


Figure 1.5: Electric double layer--charged and discharged states [23].

EDLCs store energy by means of charge separation, almost the similar way as a traditional capacitor. The significant high capacitance by EDLCs is achieved through the utilization of high surface area porous carbon materials in contrast to the two dimensional planar plates found in conventional capacitor. Following are the reasons for which EDLCs can store substantially more energy than a conventional capacitor-

- The increased amount of charge formed on the electrode surface due to the highly porous conductive surface area.
- Electrical double layer thickness formed at the interface between an electrode and the electrolyte is very small.

Typical EDLC construction is analogous to a battery, there are two electrodes immersed in an electrolyte with a impermeable separator membrane between the electrodes to prevent shorting. During charging, the electrolyte anions and cations move toward the opposite electrodes forming the two double layers, one at each electrode-electrolyte interface. A potential difference across the cell is formed due to this ion separation. Each electrode-electrolyte interface of this cell can be considered as a conventional capacitor, therefore, each cell can be considered as two capacitors connected in series. For EDLCs with identical electrodes, the cell capacitance will therefore be

$$\frac{1}{C_{cell}} = \frac{1}{C_+} + \frac{1}{C_-}$$

where,  $C_+$  and  $C_-$  are the capacitance of the positive and negative electrodes. Therefore, capacitance of the complete identical electrode super-capacitor cell is half of the capacitance of each individual electrode; that is,

$$C_{cell} = \frac{C_e}{2}$$

where  $C_e = C_+ = C_-$

The specific capacitance of an electrode,  $C_e$ , is given by

$$C_e = \frac{2 \times C_{cell}}{m_e}$$

where,  $m_e$  is the weight of the active material present in a single electrode. Therefore, unit for specific capacitance is  $\text{Fg}^{-1}$ .

Two main factors determine the performance of the EDLCs, i.e., the active material which determines the capacitance of the device and the electrolyte which determines the operational voltage window of the device [21]. These factors along with some additional sources influence the internal resistance (ESR) of the device including the following:

- The intrinsic electronic resistance of the electrode material
- Ionic resistance of the electrolyte
- Interfacial resistance between the active material and the current collector
- The ionic resistance of the ions moving into small pores
- The ionic resistance of the ions moving through the separator

Electrolyte	EW	$\kappa$	$\eta$	Cost	Assembly environment	Toxicity	Ion size	Pseudo-capacitance
Aqueous	$\leq 1$	H	L	L	Air	L	$\text{HSO}_4^-$ (aqueous) = 0.37 nm $\text{K}^+$ (aqueous) = 0.26 nm	Yes
Organic	2.5–2.7	L	M/H	M/H	Inert atmosphere	M/H	$\text{Et}_4\text{N}^+ \cdot 7\text{ACN}$ = 1.30 nm (solvated) (0.67 nm bare cation) $\text{BF}_4^- \cdot 9\text{ACN}$ = 1.16 nm (solvated) (0.48 nm bare anion)	No
ILs	3–6	VL	H	VH	Inert atmosphere	L	$\text{EMI}^+$ = $0.76 \times 0.43$ nm $\text{TFSI}^-$ = $0.8 \times 0.3$ nm	No

EW (electrochemical window, V);  $\kappa$  (experimental ionic conductivity at 20 °C, mS cm<sup>-1</sup>);  $\eta$  (viscosity at 20 °C, cP); L (low); M (moderate); H (high); VH (very high); VL (very low); ethylmethyldiazole ( $\text{EMI}^+$ ); bis(trifluoromethanesulfonyl)imide ( $\text{TFSI}^-$ ); and pseudocapacitance (pseudoC).

Figure 1.6: Comparison of typical electrolyte properties [21].

## Electrolyte

Three types of electrolytes can be used in EDLCs: (i) aqueous, (ii) organic, and (iii) ionic liquids [21]. Figure 1.6 shows a chart that summarizes the advantages and disadvantages of each electrolyte system.

Early EDLCs used aqueous based electrolyte. Recently there is a trend toward organic based electrolyte in order to achieve higher operational voltage window as well as higher specific energy.

## Electrode Materials

Most of the time carbon materials with good chemical stability, good electrical conductivity, availability, and low moderate cost are utilized for electrode materials for EDLCs. Variety of carbonization and activation procedures on different types of carbon bases is followed to acquire the electrode material. Following chart shows the properties of most common carbon materials used as electrode in EDLCs.

Electrode material	SA ( $\text{m}^2 \text{g}^{-1}$ )	C ( $\text{F g}^{-1}$ )		
		Aqueous	Organic	ILs
Activated carbons	1000–3000	200–400 [53, 54]	100–150 [55]	100–150 [30]
Templated carbons	500–2500	120–350	120–135	150
Carbon nanotubes (CNTs)	120–500	20–180	20–80	20–45 [56, 57]
Carbide-derived carbons	1000–1600	—	100–140 [28]	100–150
Carbon blacks	250–2000	<300 [58]	—	—
Aerogels/xerogels	400–1000	40–220 [59, 60]	<160	—

SA: surface area and C: gravimetric capacitance values.

Figure 1.7: Properties of most common carbon materials used as electrode in EDLCs [21].

### 1.1.5 Pseudo-capacitor

Unlike EDLCs, pseudo-capacitors experience chemical change between electrodes and electrolytes either by intercalation or reduction- oxidation or electro-sorption. For this Faradic process pseudo-capacitors gain significantly more capacitance and energy density compared to EDLCs. Metal oxides and conducting polymers are two major electrode materials used for pseudo-capacitors [21].

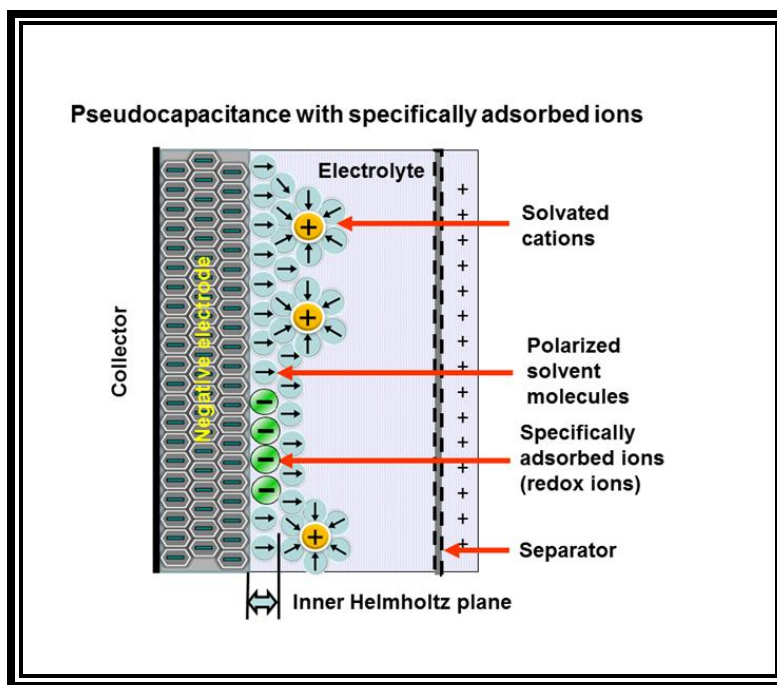


Figure 1.8: Schematic diagram for pseudo-capacitor [23].

While voltage is applied at the capacitor terminal, polarized ions or charged atoms move through the electrolyte towards the opposite polarized electrode. An electric double layer is formed between the surfaces of the electrode and the adjacent electrolyte. One layer of ions on the electrode surface and the second layer of adjacent polarized and solvated ions in the electrolyte move to the opposite polarized electrode; the two ion layers are separated by a single layer of electrolyte molecules [21]. A static field is formed between the two layers which results in double layer capacitance. Along with this phenomenon, some-desolvated ions pervade the separating

solvent layer and are adsorbed by the electrode's surface atoms. Thus, they are specifically adsorbed and transfer their charge to electrode. This phenomenon of faradic charge transfer which is originated by a fast sequence of redox reactions, electrosorptions or intercalation processes between electrolyte and the electrode surface is called pseudo-capacitance.

#### **1.1.6 Literature Review& Motivation for Super-capacitor Research**

##### **High-performance Porous Carbon/CeO<sub>2</sub> Nanoparticles Hybrid Super-capacitors for Energy Storage**

The current world has an increasing demand for low cost, environment friendly and high performance energy storage/conversion systems due to the environmental problems and depletion of fossil fuels [37]. Therefore, numerous researches have been going on for the technological improvements in electrochemical energy storage devices such as batteries [38, 39] capacitors [40, 41] and super-capacitors [42]. Among available technologies, super-capacitors can be a potential electrochemical energy storage solution owing to their sustainable cycle life, higher power densities and excellent cycling stability. They are the preferred choice in wide range of applications; i.e. electric vehicles, electronic devices, airplanes and other renewable energy storage systems [43, 44]. Based on the energy storage mechanism, super-capacitors could be classified into electrical double layer capacitors (EDLC) and pseudo-capacitors. In EDLC the capacitance comes from the electrostatic charge accumulation at the electrode-electrolyte interface which is a non-faradic process; while the pseudo-capacitors store energy through fast and reversible faradic reaction which originates from the transition metal oxide or conducting polymers present in the electrode materials [37]. Numerous researches have been done on electrode materials for super-capacitors, including carbonaceous materials, transition metal oxides and conducting polymers. Each type of electrode material has its advantage and disadvantage. For instance, carbon materials work under the EDLC mechanism for charge storage and have high power density and long cycle life while transition metal oxides work under the pseudo-capacitance mechanism for charge storage and can provide higher energy density than conventional carbon materials and better

cycling stability than conductive polymers [37, 45]. These unique properties of different materials have intrigued researchers to develop hybrid electrode materials via coupling carbonaceous materials and transition metal oxides as super-capacitor electrode. Coupling carbonaceous materials and transition metal oxides, gives the advantage of harnessing the best characteristics of both of these electrode materials into one hybrid electrode material. The hybrid material would thus possess the carbonaceous material's high power density and long cycle life, and the transition metal's high energy density. The hybridization of these properties is possible through the enhanced electrode/electrolyte interactions which gives the hybrid electrode material the ability to possess both SC capacitance mechanisms: EDLC (non-faradic) and pseudo-capacitance (faradic). The resulting hybrid electrode material would thus result in SCs with improved power density, energy density, cycling stability, and cycle life [37,42,43]. Hybrid carbon-metal oxide super-capacitors have been developed in a wide range of carbon-metal oxide combinations. Common metal oxides that have been researched include:  $\text{RuO}_2$ ,  $\text{MnO}_2$ ,  $\text{NiO}$ ,  $\text{Co}_3\text{O}_4$ ,  $\text{SnO}_2$ ,  $\text{ZnO}$ ,  $\text{TiO}_2$ ,  $\text{V}_2\text{O}_5$ ,  $\text{CuO}$ ,  $\text{Fe}_2\text{O}_3$ ,  $\text{WO}_3$ , etc. Not only is there a vast selection of metal oxides, there is also many forms of carbon that can be used, these include: zero-dimensional carbon (e.g. activated carbon, carbon nanospheres, and mesoporous carbon), one-dimensional carbon nanostructures (e.g. carbon nanotubes (CNTs) and nanofibers), two-dimensional carbon nanosheets (e.g. graphene and reduced graphene oxides (rGO)), and three-dimensional carbon (e.g. porous carbon nano-architectures, 3-D porous carbon). Researchers have explored all of these areas of hybrid electrode material for use in SCs [45].

But many of the metal oxides are expensive, scarce and toxic in nature which limits their broad applications [43].  $\text{CeO}_2$  can be one of the most attractive candidates because of its low cost, environmental friendliness and high redox potential. As nano-particle  $\text{CeO}_2$  could have higher pseudo-capacitive effect due to its excellent electrochemical redox characteristics [43]. A simple one step hydrothermal method for synthesizing porous carbon/ $\text{CeO}_2$  nanoparticle (PC-CON) hybrids for super-capacitor electrode is presented here. The prepared PC-CON hybrid electrodes

were investigated for super-capacitor applications within organic electrolyte and compared against pristine porous carbon electrodes.

### **Nanowire Modified Carbon Fibers for Enhanced Electrical Energy Storage**

The The evolving interest on portable and flexible electronic devices in recent times has intrigued researchers for developing lightweight, bendable and environment friendly energy storage devices, such as batteries [24, 25] and super-capacitors [26-28]. The electrical double layer capacitor (EDLC) or super-capacitor has become an excellent candidate among these devices with fast charging/discharging rate, high power density, sustainable cycling life and excellent cycling stability [26-30]. It has higher capacitance than general capacitor and can deliver more power than batteries [31, 32]. However, conventional super-capacitors are typically separated parts from load bearing structures, besides, they are heavy and bulky thus leading to system complexity and extra add-on weight [33]. Therefore, there is an increasing need to embed these energy storage devices such as super-capacitor into the load bearing structures to form multifunctional materials.

Prototypes of some thin flexible super-capacitors have been proposed in literature [22, 34]. Carbonaceous material such as graphene [35-39] and carbon nanotubes [40-42], hybrid composites [43-45], conducting polymers [19, 46-48] and transition metal oxides [49-51] inclusion with carbonaceous material have been used for developing flexible electrodes. Chen et al. fabricated hybrid  $\text{In}_2\text{O}_3$  nanowires/carbon nanotubes films on polyethylene terephthalate (PET) as flexible electrodes for super-capacitor with 1 M  $\text{LiClO}_4$  as electrolyte [52]. Transparent graphene/PET film was used as flexible electrodes for super-capacitor with 2 M KCl as electrolyte by Yu et al. [37]. Single wall carbon nanotube suspension was coated on both sides of a printing paper pretreated by polyvinylidene fluoride (PVDF) for flexible paper based electrodes by Hu et al. [53]. For this approach they used coffee bag to encapsulate the electrodes and electrolyte for super-capacitor fabrication. But all these developed super-capacitors could not carry mechanical loads. Recently, Lin et al. developed a ZnO/Carbon fiber hybrid that has shown improved structural



properties [54], however, its energy storage property has not been studied yet. Therefore, this paper investigates electrochemical performance of ZnO/Carbon fiber hybrid for super-capacitor electrode, aiming at developing multifunctional composites with embedded energy storage functionalities.

Herein, we report a simple two-step hydrothermal method for growing uniformly distributed ZnO nanowires (ZnO NWs) on carbon fiber cloth, compared with bare carbon fiber for super-capacitor electrode. This low temperature growth of ZnO NWs on carbon fiber cloth is biocompatible, environmentally friendly and could provide more specific surface area for highly efficient super-capacitor [55-59]. For improved performance, Au was coated on nanowire/carbon fiber electrode and bare carbon fiber electrode. Coated nanowire/carbon fiber electrode showed about 65.9% better performance than bare carbon fiber cloth in super-capacitor application with 5.5 M KOH aqueous electrolyte.

## **1.2 Lithium Ion Battery**

### **1.2.1 Working Principle**

Lithium ion battery stores energy by converting electrical energy into electrochemical energy. Figure 1.9 shows the basic working principle of a lithium ion battery. Main components of a lithium ion battery system: cathode, anode, separator and electrolyte.

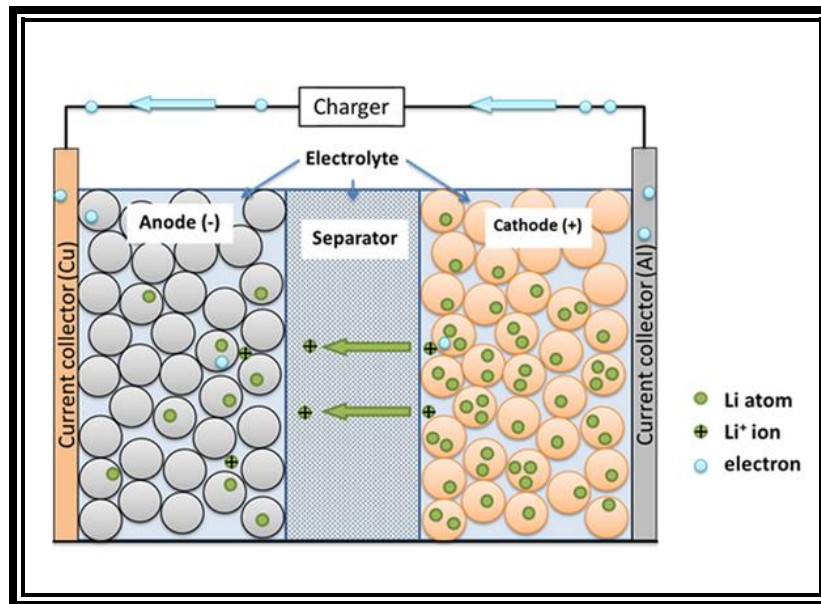


Figure 1.9: Working principle of LIB (charging).

Intercalation materials are most widely used for both anode and cathode materials of lithium ion battery. The cathode materials consist of a largely unchangeable host with specific sites for lithium, usually made of transition metal oxides. For anode the host material which is commercially used as host material is graphite. While the battery is in discharged state, all Li ions are in the cathode site. During charging, Li ions move toward the anode host for intercalation through the non-aqueous electrolyte from the cathode. At the same time, electrons move from cathode to anode. While the Li ions reach the anode, the chemical potential is much higher in anode than in cathode and this is how the electrical energy is stored in the form of electrochemical energy. During discharging, the opposite phenomenon occurs, all Li ions move towards the cathode for intercalation through the electrolyte, converting electrochemical energy into electrical energy. An impermeable micro-porous membrane is usually used to prevent shorting between the two electrodes and to facilitate ion diffusion at the same time. The electrolyte serves for the ion transportation and it should be electronically insulating in principle, properties for electrolyte is very important for lithium ion battery performance and it is very complicated [60, 61].

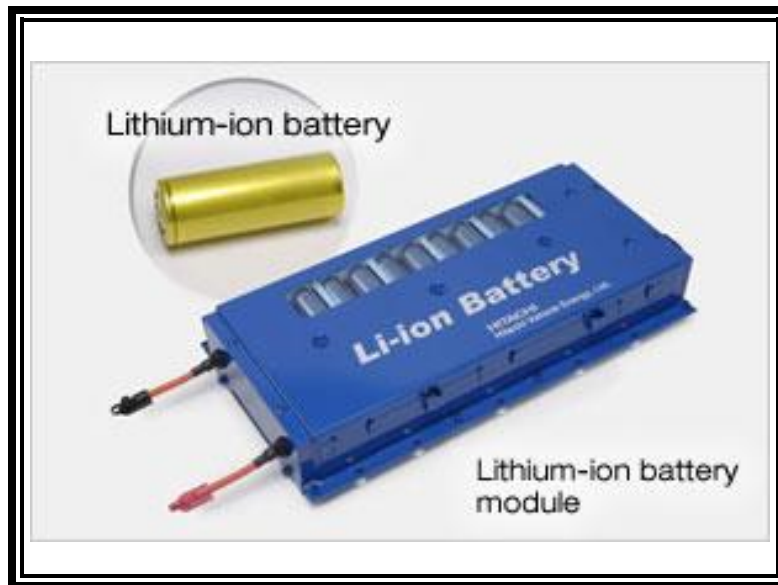


Figure 1.10: Commercial lithium-ion battery

### 1.2.2 Preliminary Considerations for Battery Design

Relative energies in the electrode and the electrolyte of a thermodynamically stable battery cell having an aqueous electrolyte are schematically shown in Figure 1.10.

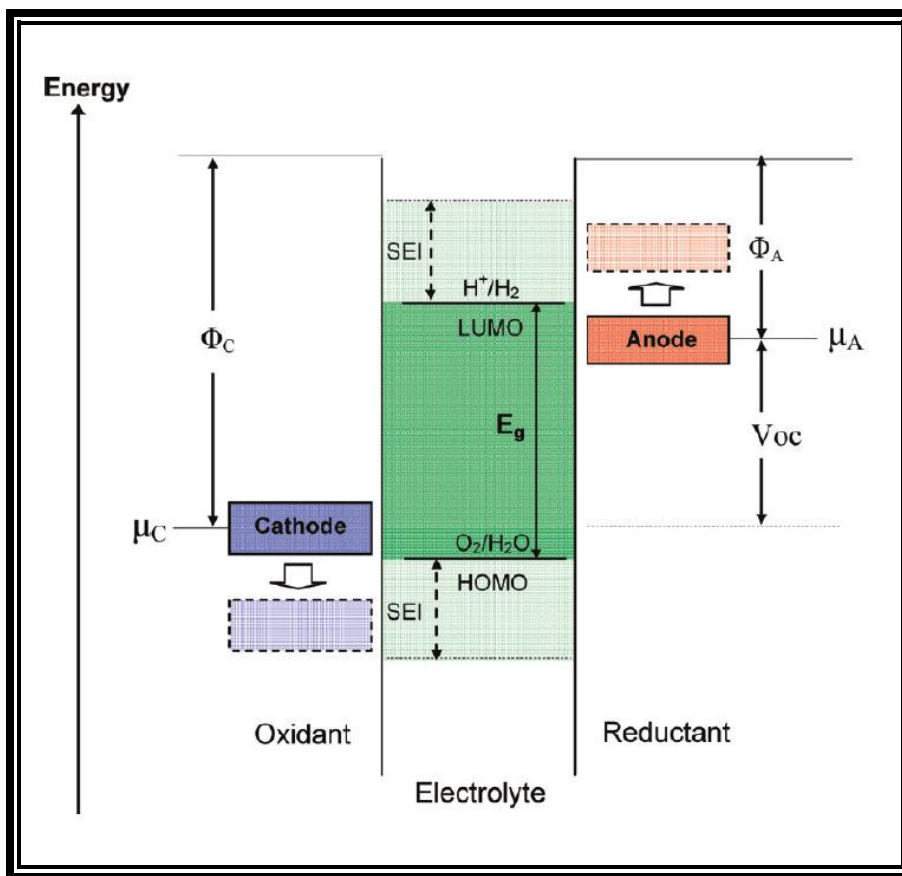


Figure 1.11: Schematic open-circuit energy diagram of an aqueous electrolyte.  $\phi_A$  and  $\phi_C$  are the anode and cathode work functions.  $E_g$  is window of the electrolyte for thermodynamic stability. A  $\mu_A > LUMO$  and/or a  $\mu_C > HOMO$  requires a kinetic stability by the formation of an SEI Layer [62].

The cathode is the oxidant and the anode is the reductant, and the voltage window of the electrolyte is determined by the energy separation  $E_g$  of the lowest unoccupied molecular orbital (LUMO) and the highest occupied molecular orbital (HOMO) of the electrolyte. Both electrodes are electronic conductors and the electrochemical potential for the anode is  $\mu_A$  and the cathode is  $\mu_C$ . If  $\mu_A$  of the anode is more than the energy level that of LUMO of the electrolyte, it is going to reduce the electrolyte unless a passivation layer forms a barrier to electron transfer from the anode material to the LUMO of the electrolyte. If  $\mu_C$  of the cathode is lower than the energy level that of HOMO of the electrolyte, it is going to oxidize the electrolyte unless a passivation layer forms a barrier to electron transfer from HOMO of the electrolyte to the cathode material [62].

Therefore, it is very essential to select electrode materials with electrochemical potential within the voltage window of the electrolyte. Hence, the open circuit voltage of a battery cell would be as follows:

$$eV_{oc} = \mu_A - \mu_C \leq E_g$$

where,  $e$  is the magnitude of the electron charge. If  $E_g - eV_{oc}$  is not too large, a passivating solid/electrolyte-interface (SEI) layer at the electrode electrolyte boundary can give kinetic stability to a larger  $V_{oc}$ .

Electrolytes	Example of classical electrolytes	Ionic conductivity ( $\times 10^{-3}$ s/cm) at room temp	Electrochemical window (V) vs $\text{Li}^+/\text{Li}^0$		Remark
			Reduction	Oxidation	
Liquid organic	1M $\text{LiPF}_6$ in EC:DEC (1:1)	$7^3$	$1.3^7$	$4.5^6$	Flammable
	1M $\text{LiPF}_6$ in EC:DMC (1:1)	$10^3$	$1.3^7$	$> 5.0^3$	
Ionic liquids	1M $\text{LiTFSI}$ in EMI-TFSI	$2.0^{15}$	$1.0^{15}$	$5.3^{15}$	Non-flammable
	1M $\text{LiBF}_4$ in EMI- $\text{BF}_4$	$8.0^{15}$	$0.9^{16}$	$5.3^{16}$	
Polymer	$\text{LiTFSI}$ -P(EO/MEEGE)	$0.1^{24}$	$< 0.0^{24}$	$4.7^{24}$	Flammable
	$\text{LiClO}_4$ -PEO <sub>8</sub> + 10 wt % $\text{TiO}_2$	$0.02^{26}$	$< 0.0^{26}$	$5.0^{26}$	
Inorganic solid	$\text{Li}_{4-x}\text{Ge}_{1-x}\text{P}_x\text{S}_4$ ( $x = 0.75$ )	$2.2^{28}$	$< 0.0^{28}$	$> 5.0^{28}$	Non-flammable
	$0.05\text{Li}_4\text{SiO}_4 + 0.57\text{Li}_2\text{S} + 0.38\text{SiS}_2$	$1.0^{30}$	$< 0.0^{30}$	$> 8.0^{30}$	
Inorganic liquid	$\text{LiAlCl}_4 + \text{SO}_2$	$70^{20}$	-	$4.4^{20}$	Non-flammable
Liquid organic + Polymer	$0.04\text{LiPF}_6 + 0.2\text{EC} + 0.62\text{DMC} + 0.14\text{PAN}$	$4.2^{38}$	-	$4.4^{38}$	Flammable
	$\text{LiClO}_4 + \text{EC} + \text{PC} + \text{PVdF}$	$3.0^{39}$	-	$5.0^{39}$	
Ionic liquid + Polymer	1M $\text{LiTFSI} + \text{P}_{13}\text{TFSI} + \text{PVdF-HFP}$	$0.18^{43}$	$< 0.0^{43}$	$5.8^{43}$	Less flammable
Ionic liquid + Polymer + Liquid organic	56 wt % $\text{LiTFSI}$ - $\text{Py}_{24}\text{TFSI} + 30$ wt % $\text{PVdF-HFP} + 14$ wt % EC/PC	$0.81^{44}$	$1.5^{44}$	$4.2^{44}$	Less flammable
Polymer + Inorganic solid	2 vol % $\text{LiClO}_4$ -TEC-19 + 98 vol% 95 (0.6 $\text{Li}_2\text{S} + 0.4\text{Li}_2\text{S}$ ) + 5 $\text{Li}_4\text{SiO}_4$	$0.03^{46}$	$< 0.0^{46}$	$> 4.5^{46}$	Non-flammable
Ionic liquid + Liquid organic <sup>19</sup>		-	-	-	Non-flammable

Figure 1.12: Non-aqueous electrolytes in LIBs [62].

The energy density of a battery is the product of  $V_{oc}$  and  $\Lambda$ ; where  $\Lambda$  is the capacity of reversible charge transfer per unit weight (Ah/g) of the between the anode and cathode. The

electronic current flow through the outer circuit should must be matched by the internal ionic current within the battery. As the electronic current density is much higher than the ionic current density of the electrolyte and electrodes, including the rate of ion transfer across the electrode/electrolyte interface, the electrodes and electrolyte have large surface area and a small thickness. The ionic motion within an electrode and/or across an electrode/electrolyte interface is too slow for the charge distribution to reach equilibrium at high current densities. This is why the reversible capacity decreases with the increase of current density in the battery. In order to achieve a battery with higher energy density, it is necessary to select an electrolyte with higher  $V_{oc}$ . Hence, non-aqueous solvents where Li salts are soluble are desirable for Li-ion battery. Therefore, HOMO of the electrolyte as well as the salt will determine the  $\mu_C$  of the cathode [62].

After determining the voltage window of the electrolyte, it is necessary to select electrode materials that have their  $\mu_C$  and  $\mu_A$  well matched to the LUMO and HOMO of the electrolyte. As Li is most positive metal on earth, it could be the most suitable anode material for LIBs but the  $\mu_A$  (is same as fermi energy) of Li lies above the LUMO, a passivating SEI layer is formed due to the electron transfer from metallic Li to electrolyte. In addition, later with charging-discharging dendrites are formed breaking the SEI which leads to short circuit within the cell. Following conditions must be satisfied for designing a high energy density battery with better reversible capacity:

- A cathode with electrochemical potential  $\mu_C$  matched to the HOMO of the electrolyte and an anode with electrochemical potential  $\mu_A$  matched to the LUMO of the electrolyte.
- A stable SEI layer which permits first Li-ion transfer along with self-healing property when broken due to the change in electrode material volume.

## Electrolytes

Along with higher voltage window with higher Li-ion conductivity, the electrolyte should also satisfy some other requirements as follows:

- An electronic conductivity  $\sigma_{Li} \leq 10^{-10} \text{S/cm}$
- Electrode/electrolyte interface retention during charging-discharging while volume of the electrode materials are changing
- Over the temperature range of battery operation, the Li-ion conductivity should be more than  $10^{-4} \text{S/cm}$
- A transference number  $\sigma_{Li}/\sigma_{total} \approx 1$ , where  $\sigma_{total}$  includes conductivities by other ions in the electrolyte as well as  $\sigma_{Li} + \sigma_e$
- Chemical stability at all temperature ranges and temperature in the battery under high power
- Low cost and environmentally benign material
- Non-flammable and non-explosive materials which are safe

Figure 1.12 shows the chart for different non-aqueous electrolytes for LIBs with different properties.

### Electrode Materials

As LIBs are of great importance for energy storage in many applications, improving their cost and performance can increase their applications and enable new technologies which depend on energy storage. Therefore, intense research is going on for the electrode materials of LIBs. Electrodes with higher rate capability, suitable electrochemical potential within the electrolyte voltage window, and higher charge capacity can improve the energy and power densities of LIBs and make them smaller and cheaper.

Wholesale price for various metals and the abundance of elements as a fraction of the Earth's crust are shown in Figure 1.13 and relative price differences among different elements can be understood from here. As electrodes are mostly fabricated from compounds not from pure metal ingots, relative price differences among different elements can be used to determine relatively cheaper compounds. Co is clearly much expensive than Mn, explaining the cost difference in the cathode materials made from these two metals. A limitation on the availability of the element can

also be found from the abundance value of the elements. The theoretical specific and volumetric capacities of the elements which undergo conversion reaction with Li are shown in Figure 1.14. These two charts can be very useful to determine suitable abundant electrode material with high specific capacity.

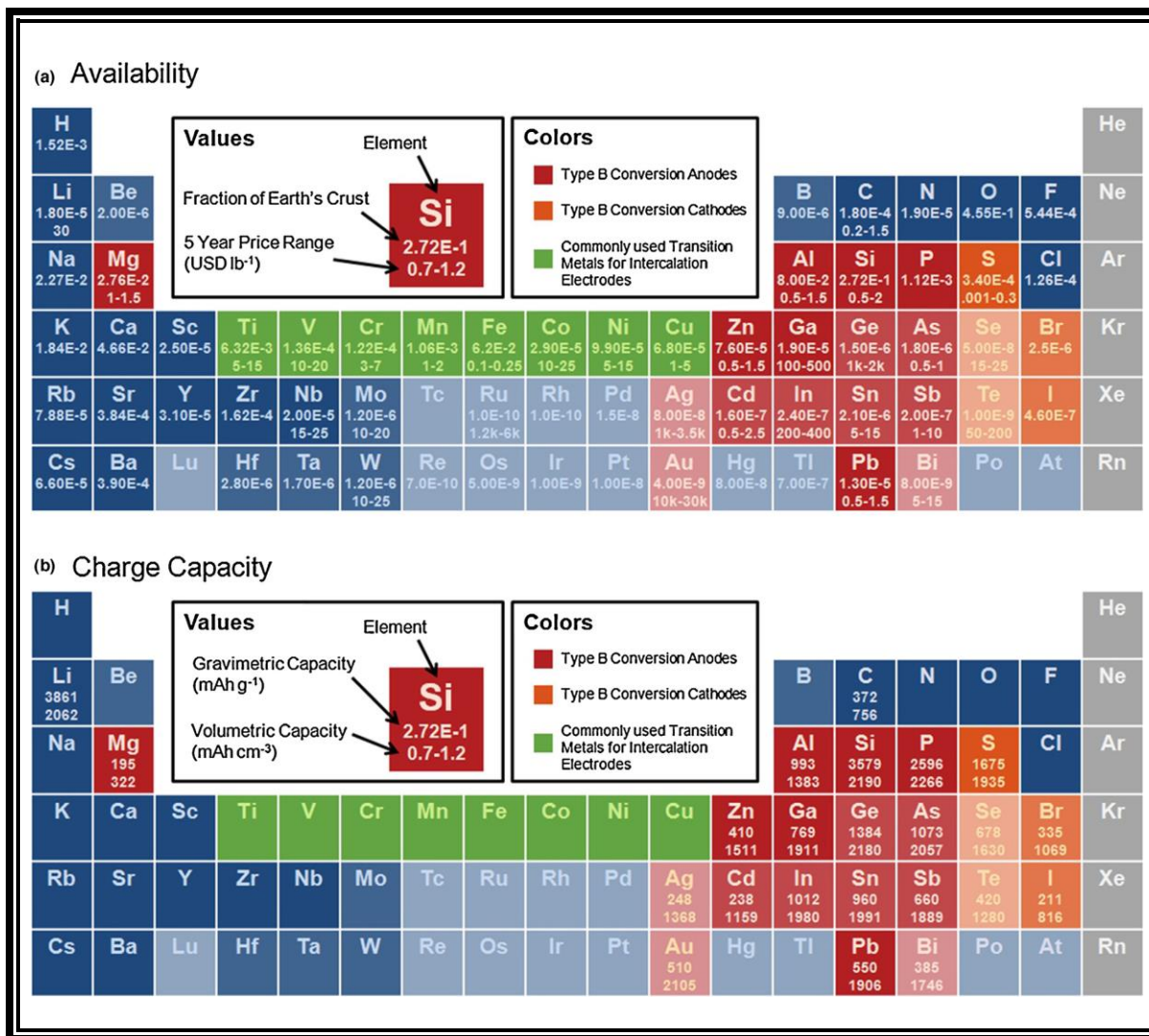


Figure 1.13: (a) Availability and (b) capacities of elements that may host Li as electrodes [63].



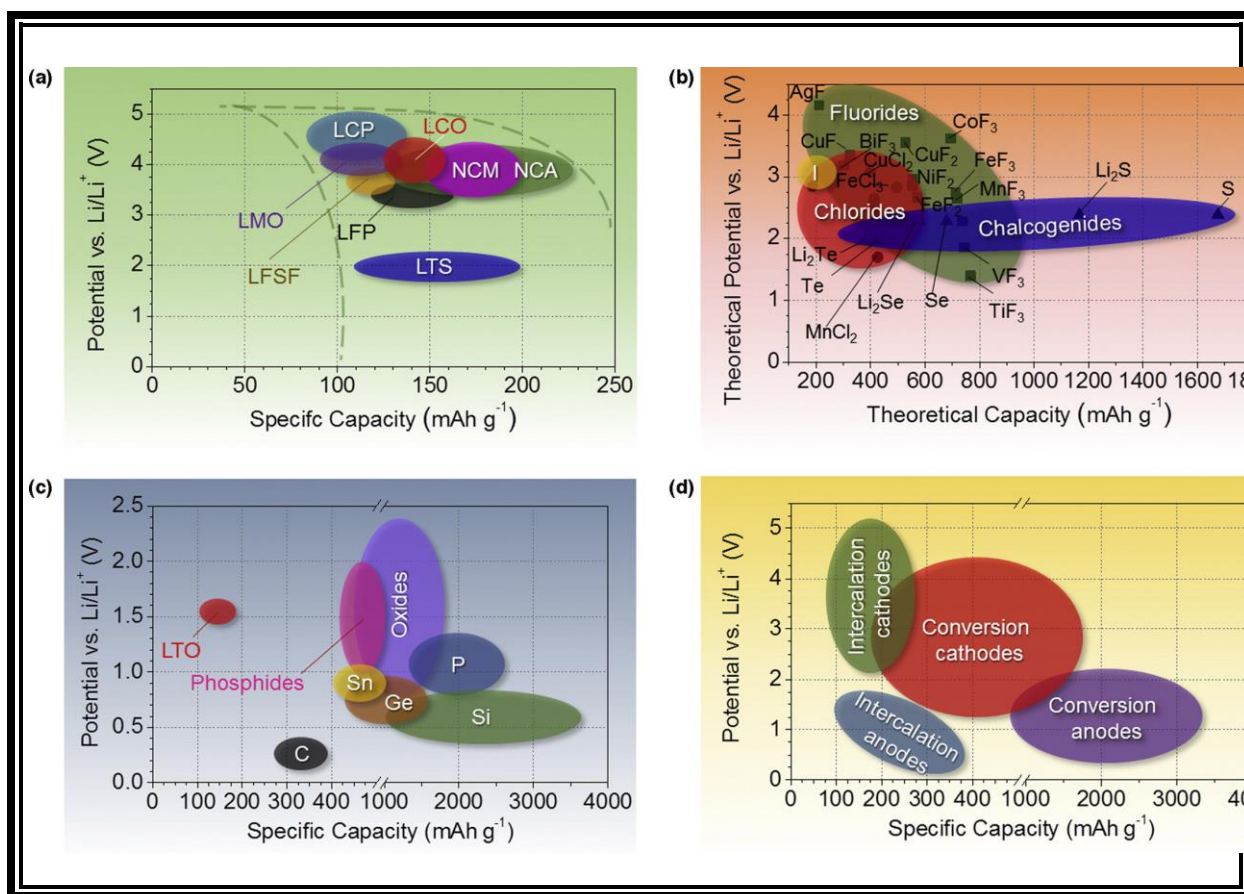


Figure 1.14: Approximate range of average discharge potentials and specific capacity of some of the most common (a) intercalation-type cathodes (experimental), (b) conversion-type cathodes (theoretical), (c) conversion type anodes (experimental), and (d) an overview of the average discharge potentials and specific capacities for all types of electrodes [63].

Figure 1.14 depicts average electrode potential against experimentally accessible (for anodes and intercalation cathodes) or theoretical (for conversion cathodes) capacity. It can be very much useful for evaluating various anode and cathode combinations and their theoretical cell voltage, capacity, and energy density. This chart is also suitable for selecting electrolytes, additives, and current collector for the electrode materials.

### **1.2.3 Literature Review and Motivation for Lithium-ion-battery Research**

#### **Microwave Exfoliated Graphene Oxide/TiO<sub>2</sub> Nanowire Hybrid for High Performance Lithium Ion Battery**

Developing high energy density energy storage device is one of most important research goals as energy storage is the probable key solution for the utilization of alternative energy and thus for the replacement of fossil fuels and traditional energy sources [39-42, 46-48]. Lithium-ion-battery (LIB) is a potential candidate for energy storage application and LIB has wide range of applications due to its high energy density, light weight, and long cycle life [33, 39, 49, 50]. The route towards innovating future LIB depends on either synthesizing novel electrode materials or formulating a unique electrolyte with higher voltage window. Presently, graphite is widely used as anode materials for the commercial productions of LIBs but lithium storage capacity of graphite is limited. The multilayer nature of graphite materials limits Li-ion diffusion, resulting in low charge-discharge rate performance for the battery [33, 39].

To improve the charge-discharge rate, extensive research has been done focusing on Li-ion and/or electron transport in electrode. Carbon based materials are broadly studied for LIB anode materials because of their desirable features, such as low cost, light weight, thermal and chemical stability [33, 39, 49, 51-54]. Ji et al. showed that porous carbon nanofibers have better reversible capacity and cycling performance than conventional graphite anode due to the porous structure that facilitates the ion transport [51]. Yang et al. showed that porous carbon structure is an excellent candidate for anode materials for high power density LIB [55]. In addition, various nanomaterials of metal oxides have been used as anode materials for LIB [39, 47, 52]. TiO<sub>2</sub> nanomaterials demonstrated its effectiveness as anode materials and this metal oxide is abundant in nature, low cost, and environmentally benign [39, 56-58]. Hybrid nanostructures electrodes which interconnect nanostructured electrode materials with conductive additive nanophases, is another way of improving Li-ion insertion properties [39, 50, 59]. For example, hybrid nanostructures, such as Mn<sub>3</sub>O<sub>4</sub>-graphene hybrids or LiFePO<sub>4</sub>-RuO<sub>2</sub> nano-composite, combined

with conventional carbon additives (e.g., acetylene black), have demonstrated an increased Li-ion insertion/extraction capacity in hybrid electrodes at high charge/discharge rates [47, 60].

Graphene, a single layer of graphite with perfect 2D crystal of sp<sup>2</sup> hybridized carbon atoms, has been found to have extraordinary properties that could further enhance LIB performance. It has high specific surface area (2600 m<sup>2</sup>/g) and can sustain at a current density up to six times that of copper [33, 39, 47, 61, 62]. Therefore, graphene has been found as the ideal conductive additive for hybrid nanostructured electrode. However, synthesizing graphene through chemical vapor deposition (CVD) method or thermal reduction of graphene oxide is expensive and time consuming, leading to high cost and limited scale application.

A highly efficient and low cost synthesize method of fabricating a hybrid anode structure using microwave exfoliated graphene oxide (MEGO) and TiO<sub>2</sub> nanowires is presented here. The MEGO was obtained through microwave treatment of solution processed graphene oxide (GO). Later, a simple hydrothermal method was utilized to obtain TiO<sub>2</sub> nanowires on exfoliated graphene oxide sheet. This obtained microwave exfoliated graphene oxide/TiO<sub>2</sub> nanowire (MEGO-TON) hybrid electrode material was compared with porous carbon (PC). The MEGO-TON hybrid has shown higher reversible capacity and rate capacity than PC when used in LIB as anode material. This simple hybrid anode material synthesis method has the potential to be utilized for large-scale anode material production for LIBs.

### **Porous carbon/CeO<sub>2</sub> composites for Li-ion battery application**

The ever-increasing demand for portable electronic devices is the drive force behind the technological improvements in electrochemical energy storage devices such as batteries [25, 26] capacitors [27-29] and supercapacitors [30, 31]. These energy storage devices have a wide range of applications starting from wireless phones, laptops, camcorders to electric and hybrid electric vehicles. Although significant amount of research is focused on developing next generation passive sensors [32], batteries and capacitors are still the most widely used energy source for different sensors and sensor networks. Lithium-ion batteries are widely considered as the

technology of choice owing to its high energy density, lightweight and flexible design and longer lifespan. Although Li is the most electropositive metal [26] (-3.04V), Li metal batteries suffered from dendritic Li growth, which led to explosion hazards, and it was necessary to find an alternative solution. Use of carbonaceous material for anode and  $\text{Li}_x\text{MO}_2$  for cathode material solved the issue as Li is present as Li ion rather than the metal form [26, 33], however the specific capacity and specific energy is considerably lower than the Li metal batteries. Numerous investigations have been being carried out to address this issue. Porous carbon is considered one of the most promising materials for anode application as it has a high specific surface area (2000  $\text{m}^2/\text{g}$ ), which enables higher charge-discharge rate along with high charge capacity. It has been also demonstrated that use of metal oxides nanowires or nanoparticles can increase the reversible capacity and rate capacity of a Li-ion battery (LIB) [34]. Cerium oxide ( $\text{CeO}_2$ ) or Ceria is a rare earth oxide that has high oxygen storage capacity, high electrical conductivity and diffusivity and high thermal stability [35, 36]. It offers high potential as an anode material for LIB due to its fast transformation between Ce(III) and Ce(IV) oxalates which have relatively low decomposition temperature in air, good structural stability and are of low cost [34]. In this work, a facile one step hydrothermal method is used to synthesize Ceria nanoparticles on Porous Carbon for LIB electrodes and the performance is compared with bare porous carbon electrodes.

### **Investigation of modified graphene for energy storage applications**

Electrochemical energy storage devices such as batteries and capacitors have been receiving great attention for electronic vehicles, cell phones and other mobile electronic devices as energy sources. As a leading candidate among energy storage devices, lithium-ion-batteries (LIB) are in the highlighted area of research due to their lightweight and high specific energy [64]. Therefore, there is an increasing demand of research for developing potential LIB electrode materials with fast Li-ion diffusion, high electron transportability and low resistance at the interface of electrode/electrolyte at high charge-discharge rates. Commercially, graphite is being used as the anode material for LIB which interacts (intercalation/de-intercalation) with Li-ions

during the electrochemical process. A graphite anode accepts sufficient Li-ions to form  $\text{LiC}_6$  during charging as Li-ions intercalate into the anode material and during discharging Li-ions diffuse from the anode to the cathode. The extent to which this is carried out determines the specific energy density for the cell, therefore, amount of Li-ion diffusion is important for cell performance [65]. The multilayer nature of graphite materials limits Li-ion diffusion resulting in low charge-discharge rate performance for the battery.

Graphene, a single layer of graphite with perfect 2D crystal of  $sp^2$  hybridized carbon atoms, has been found to have extraordinary properties which can enhance LIB performance [66]. It has high specific surface area ( $2600 \text{ m}^2/\text{g}$ ) and can sustain at a current density up to six times that of copper [67, 68]. It has also shown to have ballistic electron transportability with electron mobility as high as  $15,000 \text{ cm}^2/(\text{V} \cdot \text{sec})$  and also has incredible mechanical and thermal properties [69-71]. For having high specific surface area and excellent conductivity, graphene based anode materials give rooms to Li-ion in anode for better diffusion, thus obtain enhanced battery performance. On contrary graphene sheets are prone to agglomeration due to van der Waals forces which may form graphite again, thus hindering Li intercalation. Therefore, different metal oxides ( $\text{Mn}_3\text{O}_4$ ,  $\text{Fe}_2\text{O}_3$ ,  $\text{Co}_3\text{O}_4$  etc.) had been grown on graphene sheets in the form of nanowires/nanoparticles to prevent agglomeration [72-75]. These grown nanoparticles enable graphene nanosheets of high conductive surface area leading to high electrode-electrolyte contact area and fast Li-ion diffusion rate. Previously, synthesis methods such as electrophoretic deposition, sol-gel, template based method and hydrothermal growth have been developed for nanowire synthesis [6, 76, 77]. But in previous approaches nanoparticles were distributed randomly in graphene sheets which limit LIB performance.

Herein, we report a facile two step hydrothermal method for growing uniformly distributed aligned ZnO nanowires (ZnO NWs) on graphene aerogel for LIB electrodes, compared with bare graphene electrode. ZnO in various structures have shown high reversible capacity and rate capacity when used in LIB as anode materials [78]. Moreover, to our best knowledge, anode material with aligned ZnO NWs has not yet been reported. A low temperature hydrothermal

method was used for growing these aligned nanowire arrays with open space which allows easy diffusion of Li-ions into the inner region of electrode, resulting in improved energy density and performance. Also, since each nanowire is vertically grown on the substrate, it is directly contacted with the current collector substrate and each nanowire could participate in energy conversion process, resulting in significantly increased charge and discharge rates for LIB upon future investigation.

## **Chapter 2: Fabrication and Assembly**

One major portion of this research is the chemical synthesis route for the development of electrode materials. This chapter will discuss on all chemical synthesis which were carried out for the preparation of electrode materials for both super-capacitors and Lithium-ion-batteries. Later, electrode fabrication procedure is also elaborately described. At last, procedures for coin cell assembly for the both electrochemical devices are also discussed.

### **2.1 Electrode Fabrication for Super-capacitor**

For electrode fabrication for the first worked described, at first electrode material was synthesized through chemical route. Porous carbon from ACS Material, LLC and Ammonium Cerium Nitrate  $(\text{NH}_4)_2\text{Ce}(\text{NO}_3)_6$  (99.5%) from Arcos Organics were purchased for the chemical synthesis. Later, a thermo-scientific tube furnace was employed for the heat treatment of the synthesized material in Argon environment. At last, the prepared materials were mixed with binding materials and coated on aluminum foil for the final electrode.

#### **2.1.1 High-performance Porous Carbon/CeO<sub>2</sub> Nanoparticles Hybrid Super-capacitors for Energy Storage**

##### **Porous Carbon/ Cerium Oxide Nanoparticle (PC-CON) Hybrid Synthesis**

The PC/CON hybrid synthesis is a one-step hydrothermal method. At first 100mg of porous carbon (ACS Material, LLC) was dispersed in 200mL of deionized water (DI) water. Then 150mL of 0.02M Ammonium Cerium Nitrate  $(\text{NH}_4)_2\text{Ce}(\text{NO}_3)_6$  was added to the solution and the solution was sonicated (Branson Sonifier 450) for 45 minutes. The mixture was then separated by centrifugation. At this stage  $\text{Ce}(\text{OH})_4$  was formed into the pores and on the surfaces of the porous carbon. Then the product was mixed with 100mL 5M NaOH solution and transferred into a Teflon lined autoclave. After heating the mixture for 45 hours at 180° C, the solution was separated by centrifugation, washed with DI water for three times. Then the remnant was dried at 70° C. At last

the product was heated at 450° C in Argon for 2 hours [79, 80]. Figure 2.1 shows the schematic illustration of PC-CON synthesis.

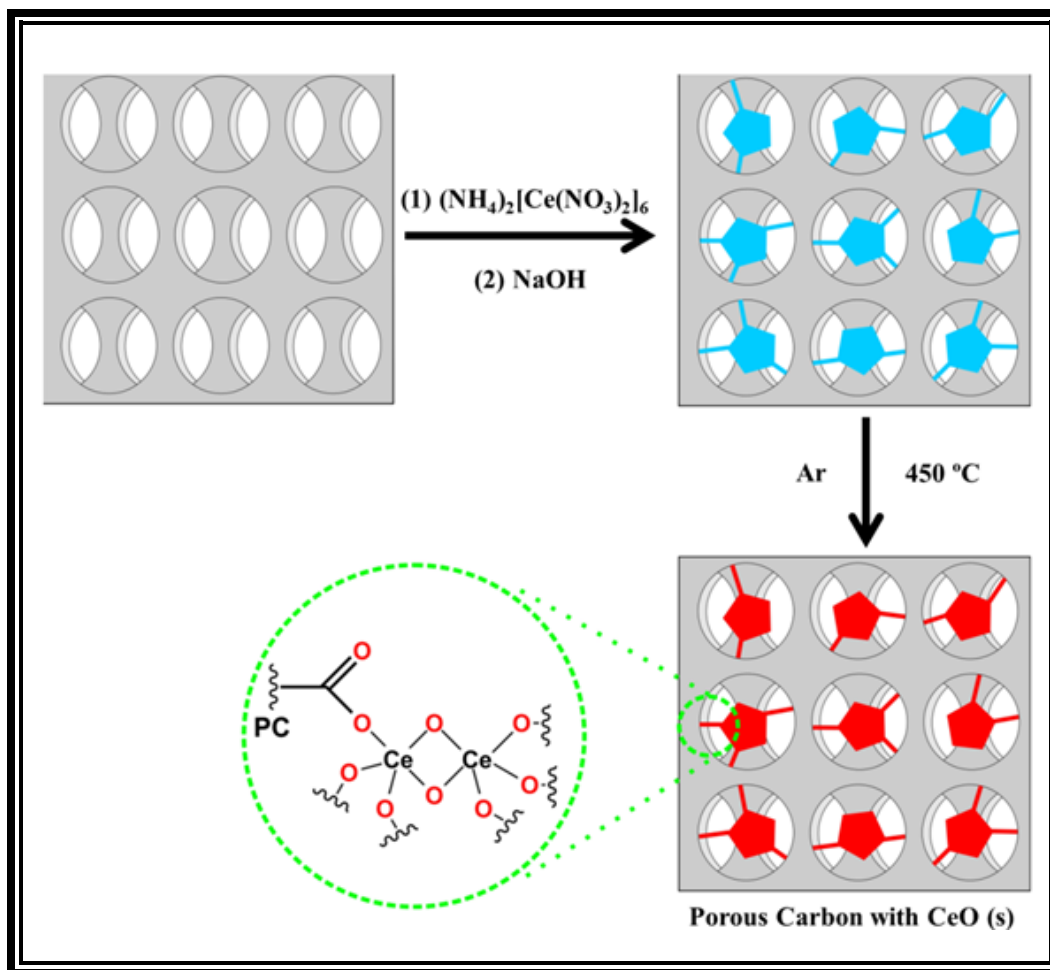


Figure 2.1: Schematic illustration of porous carbon/CeO<sub>2</sub> nanoparticle synthesis.

## 2.1.2 Nanowire Modified Carbon Fibers for Enhanced Electrical Energy Storage

### Carbon fiber/Zinc oxide nanowire hybrids Synthesis

The ZnO nanowire growth is a two-step hydrothermal growth method including seeding and nanowire growth. Briefly, ZnO nanoparticle seeds were first synthesized in an organic solution, and then the seeding process was performed to coat ZnO nanoparticles onto carbon fiber cloth. The seeded carbon cloth was transferred to ZnO nanowire hydrothermal growth solution at



elevated temperature and atmospheric pressure. After the nanowire growth, the nanowire/carbon fiber was rinsed extensively and dried in air for super-capacitor assembly.

#### *ZnO seed particles*

Carbon cloth (made of carbon fiber, diameter  $\sim 7\ \mu\text{m}$ ) of 50 mm X 30 mm was glued (Devcon, 5 minutes epoxy) on the edges. Then carbon cloth was first cleaned in bath sonication (Branson, 2510). Acetone, Deionized water (DI) and ethanol were used as cleaning solvent. Carbon cloth was placed in a beaker with cleaning solvent and bath sonication was performed for 10 minutes using each solvent. Then carbon cloth was dried at ambient temperature in open air. The clean carbon cloth was taken on a glass petri dish to soak in the nanoparticle solution for 10 minutes and subsequently annealed on a hot plate at 150 °C for 10 minutes to enhance adhesion between the substrates and nanoparticles. This soaking and annealing was repeated two more times to ensure the mass coating of ZnO nanoparticle all over the carbon fibers [54, 81].

#### *ZnO nanowires*

After seeding, hydrothermal growth of ZnO nanowires was performed using a low temperature hydrothermal method detailed elsewhere <sup>4</sup>. Briefly, an aqueous solution of 25 mM zinc nitrate hexahydrate ( $\text{Zn}(\text{NO}_3)_2 \cdot 6\text{H}_2\text{O}$ , 99.9% purity, Sigma-Aldrich), 25 mM hexamethylenetetramine (HMTA) ( $\text{C}_6\text{H}_{12}\text{N}_4$ , 99.9% purity, Sigma-Aldrich) and 5-7 mM Polyethylenimine (PEI, Branched) were prepared at room temperature. Carbon fiber cloth was immersed in growth solution when the temperature was at 85 °C. The time duration of this growth was 2 hours for all the carbon fiber samples. After the reaction had been completed, carbon fiber samples were taken out of the solution and rinsed with DI water and dried at 100 °C on a hot plate for 2 hours.

### 2.1.2 Electrode preparation

#### High-performance Porous Carbon/CeO<sub>2</sub> Nanoparticles Hybrid Super-capacitors for Energy Storage

A two-electrode testing set up was prepared using coin cells (CR 2032) because it provides accurate measure for an electrode's performance for electrochemical capacitors [82]. For making both PC and PC-CON electrodes, polyvinylidene fluoride (PVDF, MTI corp., purity  $\geq 99.5\%$ ) was used as binding material. PVDF was dissolved in N-Methyl-2-pyrrolidone (NMP, MTI corp., purity  $\geq 99.5\%$ ) at a 1:2.5 weight ratio by heating at 80 °C. Later, 80 wt% active material and 10 wt% activated carbon were dispersed in 10 wt% PVDF with excess NMP to prepare homogenous slurry using a homogenizer. Then, the slurry was coated on Aluminum foil (MTI Corp. , 15  $\mu\text{m}$  thickness) and dried at 100 °C on a hot plate. Next, a precision disc cutter from MTI Corporation was used to cut anodes with 13 mm diameter, and the pieces were kept overnight in vacuum oven. Figure 2.2 shows the schematic view of electrode preparation.

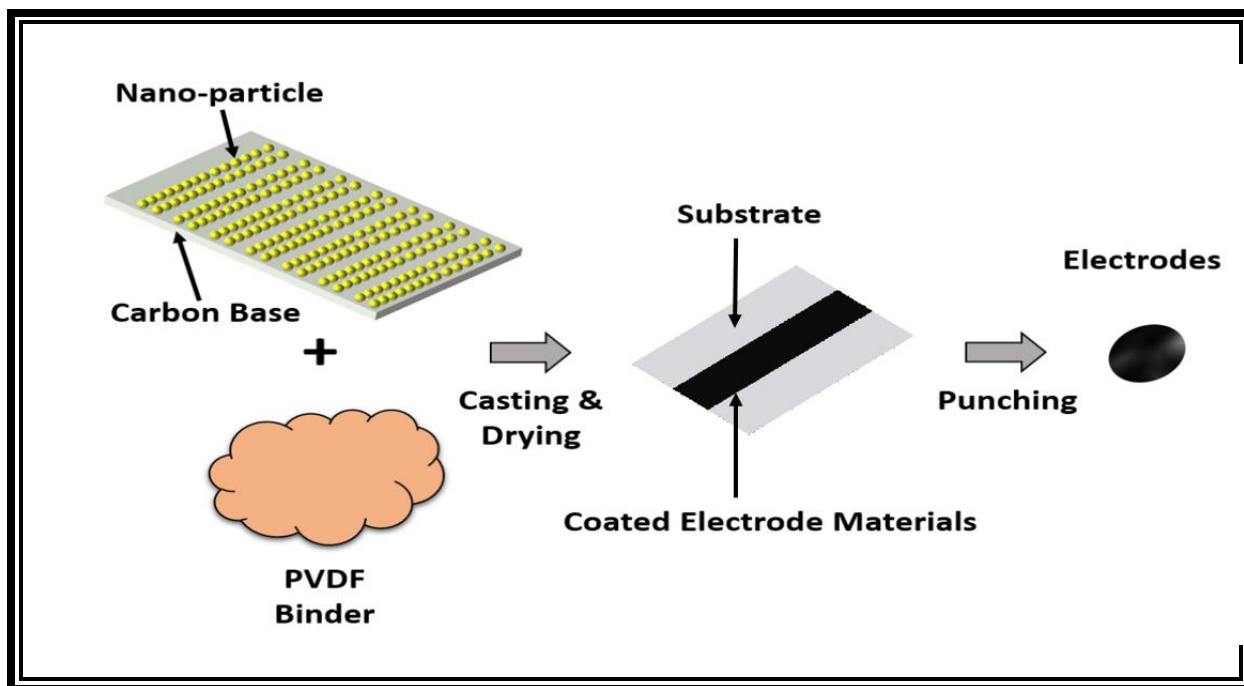


Figure 2.2: Two-electrode test cell configuration.

## 2.2 Super-capacitor Assembly

### High-performance Porous Carbon/CeO<sub>2</sub> Nanoparticles Hybrid Super-capacitors for Energy Storage

All the electrodes were brought into an Argon filled glovebox (Unilab, MBraun) for the super-capacitor coin cell assembly. CR 2032 coin cell cases were purchased from MTI Corporation for the preparation of coin cell super-capacitor. A Hydraulic crimping machine from MTI Corp. was used for the coin cell assembly. For precision measurement of the electrolyte, a micro-pipette was used. Celgard 2500 (25  $\mu\text{m}$  microporous monolayer membrane) with uniform pore structure was used as the separator. Oxygen and moisture level were kept less than 0.1 ppm inside the glovebox. 1M Tetraethylammonium Tetrafluoroborate (TEABF<sub>4</sub>) (Sigma Aldrich) in acetonitrile was prepared inside the glovebox for the electrolyte.

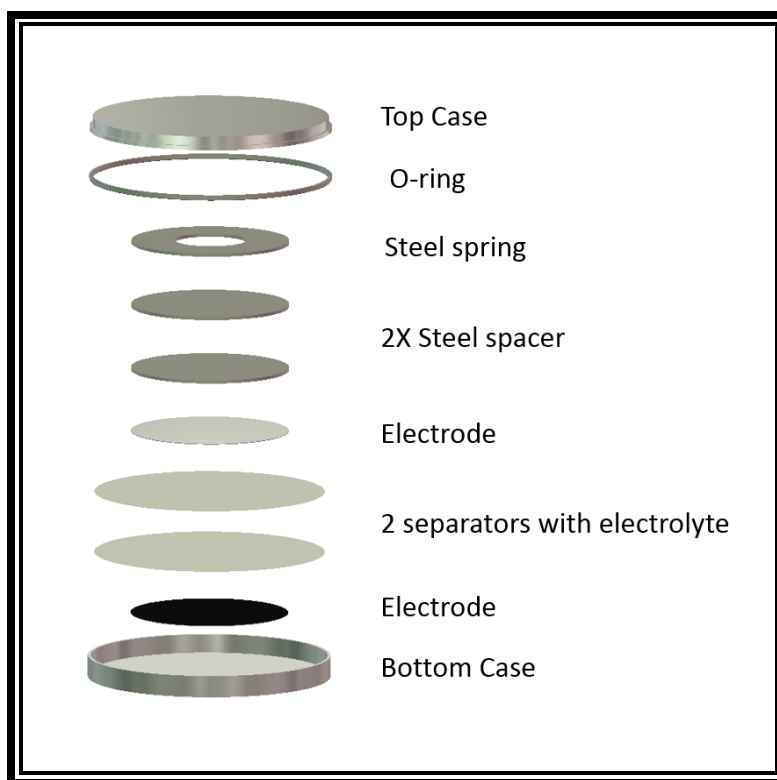


Figure 2.3: Schematic view of coin cell assembly.

A very specific sequence is followed for the assembly of SC shown in figure 2.3. An electrode is placed on bottom case facing the active material up. 35  $\mu\text{l}$  of electrolyte is added on electrode followed by two separators and in between them another 35  $\mu\text{l}$  of electrolyte is added. After that another electrode facing downward is placed on the separator. The rest of the sequence is as follows: two spacers, spring and top case. Coin cells are sealed by applying 750 psi pressure with a crimping machine (MTI corp.). Excess electrolyte is wiped off after the crimping.

### **Nanowire Modified Carbon Fibers for Enhanced Electrical Energy Storage**

A two electrode testing set up was prepared as shown in figure 1 because it provides most accurate measure for an electrode's performance for electrochemical capacitors [83]. Both bare carbon fiber (CF) and ZnO NWs on carbon fiber samples were sputtered with gold (Au) for 120 seconds to prepare four kinds of electrodes, i.e., a) carbon fiber (CF), b) carbon fiber coated with Au (CF-Au), c) ZnO nanowires on carbon fiber (ZnO-CF), and d) ZnO nanowires on carbon fiber coated with Au (ZnO-CF-Au). A hand punch with 19mm diameter was used for preparing circular electrodes and copper tape was used as current collector. An aqueous solution of 5.5 M KOH was prepared for electrolyte and Celgard 3501 was used as separator.

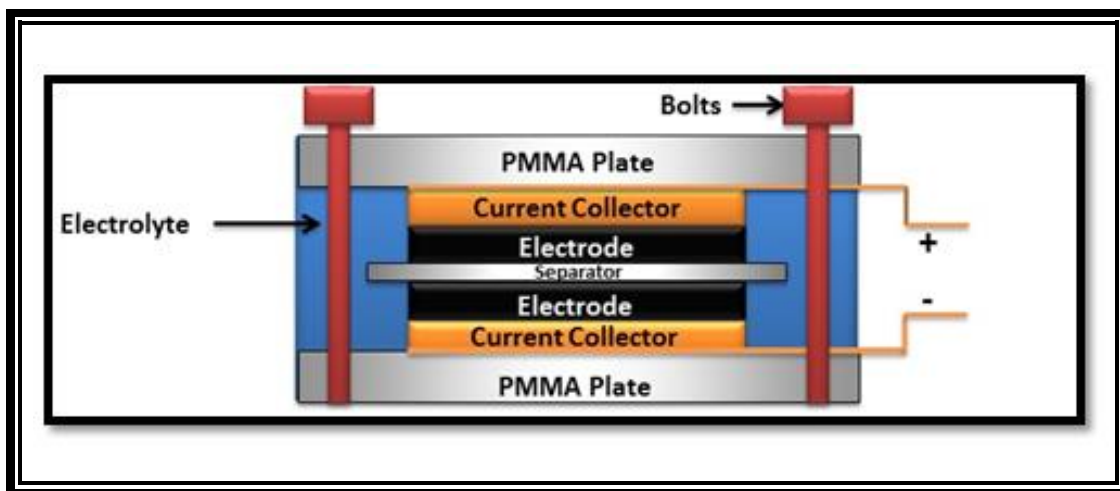


Figure 2.4: Schematic view of coin cell assembly.

## **2.3 Electrode Fabrication for Lithium-ion-battery**

### **2.3.1 Microwave Exfoliated Graphene Oxide/TiO<sub>2</sub> Nanowire Hybrid for High Performance Lithium Ion Battery**

#### **Microwave Exfoliated Graphene Oxide/TiO<sub>2</sub> Nanowire (MEGO-TON) Synthesis**

##### **Synthesis of Graphene Oxide (GO)**

Improved Hummer's method was utilized for the synthesis of GO [84]. A 9:1 mixture of concentrated H<sub>2</sub>SO<sub>4</sub>/H<sub>3</sub>PO<sub>4</sub> (360:40 ml) (Fisher Scientific/EM Science, respectively) was added to a mixture of graphite flakes (3.0 g, 1wt. equiv.) (Alfa Aesar, natural, 10 mesh, 99.9%) and KMnO<sub>4</sub> (18.0 g, 6 wt. equiv.) (Fisher Scientific). The reaction was then heated to 50°C in a water bath and stirred for 12 hrs. The reaction was cooled to room temperature and poured onto ice and D.I. water mixture (~400 ml) with 30% H<sub>2</sub>O<sub>2</sub> (3 ml). The mixture was then thoroughly mixed and centrifuged to decant away supernatant. The remaining solid material was then washed in succession with 200 ml of water, 200 ml of 30% HCl (diluted: 37.3% Assay, Fischer Scientific), and then several general washes with water to drive away any traces of sulfur. The remaining solid material was vacuum dried overnight at 50°C.

##### **Microwave Exfoliation of Graphene Oxide**

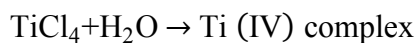
GO obtained from improved Hummer's method were treated in a microwave oven (Haier, Model: MWMM0701TB) in ambient condition at 700 W for 1 min. A large volume expansion of GO was observed. Due to the microwave radiation the GO was exfoliated and became fluffy black powder which indicates reduction of the GO.

##### **Synthesis of TiO<sub>2</sub> Nanowires on MEGO**

The TiO<sub>2</sub> nanowires were synthesized following a simple hydrothermal method [85]. Microwave reduced graphene oxide (0.5 g) was transferred to a 250 mL Pyrex glass bottle and mixed with a 100 mL solution containing DI water and concentrated hydrochloric acid (HCl, 37.3% Assay, Fischer Scientific) in a 1:1 volume ratio. Subsequently, 5 mL of the titanium tetrachloride (99.0% purity, Sigma Aldrich) was added drop-wise to this solution. The glass bottle was then placed inside an aluminum cylinder and transferred into an oven at 160 °C for 4 hours.

After that, the resulting materials were rinsed several times with DI water and dried at 90 °C for 30 minutes.

The as-prepared samples were characterized using powder X-ray diffraction (XRD, B8 Discover, Bruker) and scanning electron microscopy (SEM, S-4800, Hitachi). In the above reaction condition, the formation of TiO<sub>2</sub> nanowires takes place as follows-



Later, the obtained materials were heated at 450 °C for 2 hours in Argon environment for complete reduction of the MEGO. Schematic representation for the MEGO-TON hybrid synthesis is shown in Figure 2.5.

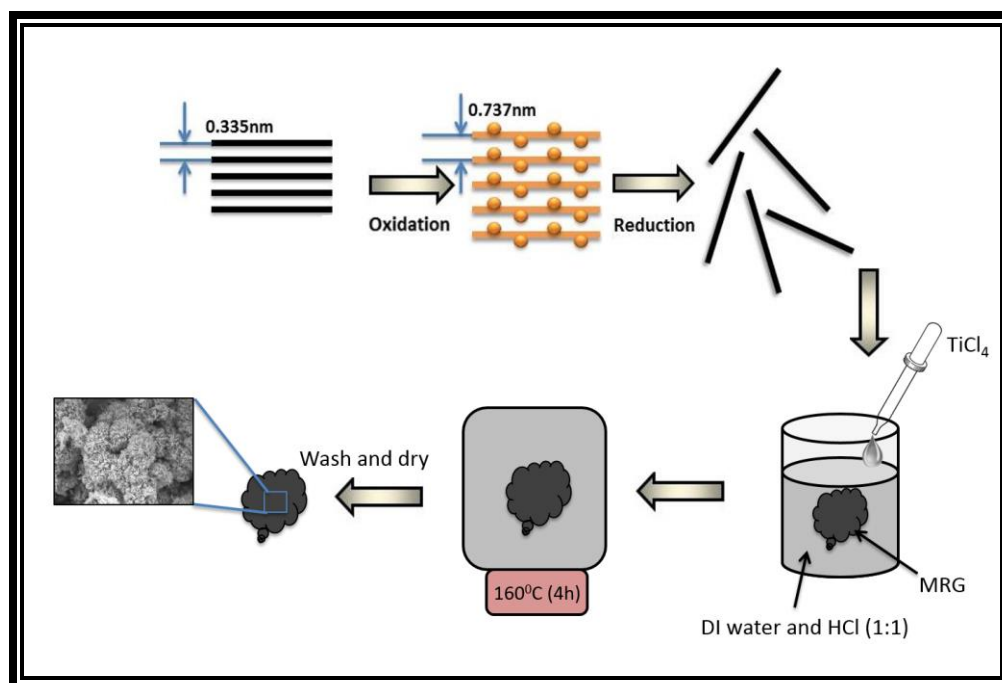


Figure 2.5: Schematic view of coin cell assembly.

### 2.3.2 Porous carbon/CeO<sub>2</sub> composites for Li-ion battery application

#### Porous Carbon/ Cerium Oxide Nanoparticle (PC-CON) Hybrid Synthesis

The PC/CON hybrid synthesis is a one-step hydrothermal method. At first 100mg of porous carbon (ACS Material, LLC) was dispersed in 200mL of deionized water (DI) water. Then 150mL of 0.02M Ammonium Cerium Nitrate  $(\text{NH}_4)_2\text{Ce}(\text{NO}_3)_6$  was added to the solution and the solution was sonicated (Branson Sonifier 450) for 45 minutes. The mixture was then separated by centrifugation. At this stage  $\text{Ce}(\text{OH})_4$  was formed into the pores and on the surfaces of the porous carbon. Then the product was mixed with 100mL 5M NaOH solution and transferred into a Teflon lined autoclave. After heating the mixture for 45 hours at 180° C, the solution was separated by centrifugation, washed with DI water for three times. Then the remnant was dried at 70° C. At last the product was heated at 450° C in Argon for 2 hours [79, 80]. Figure 2.1 shows the schematic illustration of PC-CON synthesis.

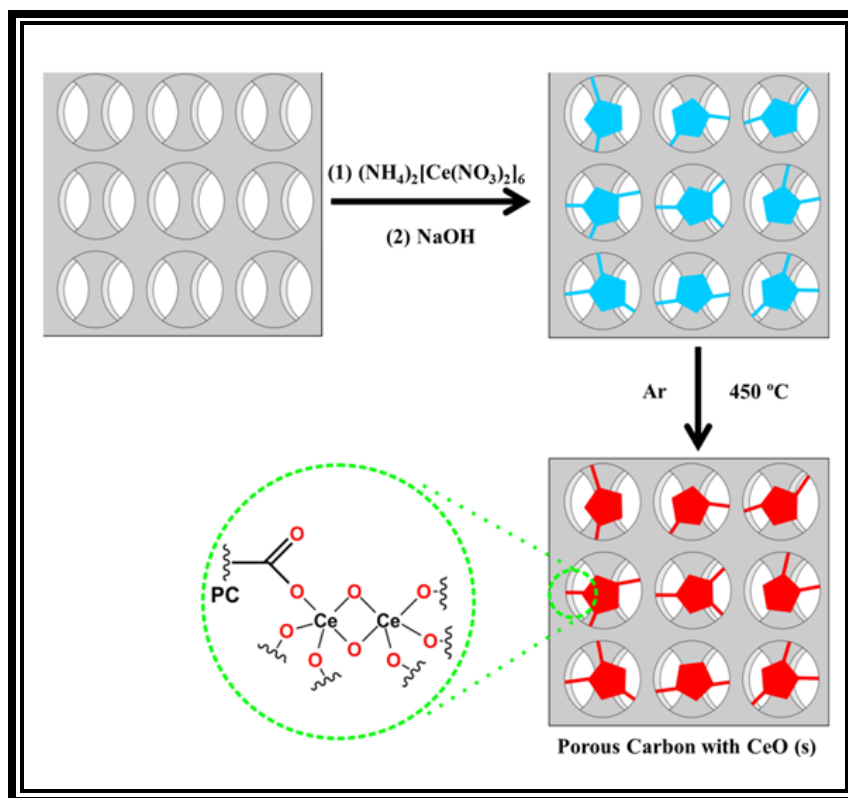


Figure 2.6: Schematic illustration of porous carbon/CeO<sub>2</sub> nanoparticle synthesis.

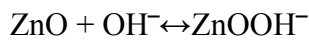
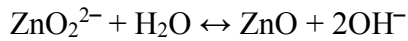
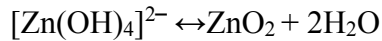
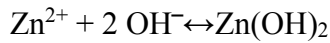
### 2.3.3 Investigation of modified graphene for energy storage applications

#### Graphene/Zinc oxide nanowire hybrids Synthesis

The ZnO nanowire growth is a two-step hydrothermal growth method including seeding and nanowire growth. Briefly, ZnO nanoparticle seeds were first synthesized in an organic solution, and then the seeding process was performed to coat ZnO nanoparticles onto graphene aerogel. Those seeded graphene aerogels were transferred to ZnO nanowire hydrothermal growth solution at elevated temperature and atmosphere pressure. After the nanowire growth, the nanowire/graphene aerogel were rinsed extensively and dried in air for LIB anode fabrication.

##### *ZnO seed particles*

A 12.5 mM zinc acetate (98.0% purity, Sigma Aldrich) dehydrate ethanol solution was prepared at 50 °C under vigorous stirring [54]. After completely dissolved, the solution was cooled down to room temperature and diluted to a concentration of 1.4 mM by adding extra ethanol. 20 mM of sodium hydroxide (Acros) ethanol solution was prepared at 60 °C under vigorous stirring and cooled down to room temperature, additional ethanol was added in order to dilute to 5.7 mM. These two solutions were mixed at a volume ratio of 18:7 at a temperature of 55 °C for 30 minutes to form ZnO nanoparticle seeds. The reactions involved in formation ZnO seed particles are as follows:

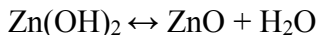
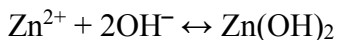
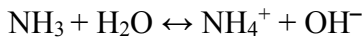
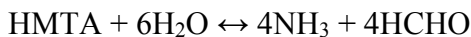


##### *ZnO nanowires*

The first step of the nanowire growth is seeding process. GA was dipped in the seed solution for 5 minutes and subsequently annealed on a hot plate at 150 °C for 10 minutes to enhance adhesion between the GA and nanoparticles. Hydrothermal growth of ZnO nanowires was performed using a low temperature hydrothermal method detailed elsewhere [4]. Briefly, an



aqueous solution of 25 mM zinc nitrate hexahydrate ( $\text{Zn}(\text{NO}_3)_2 \cdot 6\text{H}_2\text{O}$ , 99.9% purity, Sigma-Aldrich), 25 mM hexamethylenetetramine (HMTA) ( $\text{C}_6\text{H}_{12}\text{N}_4$ , 99.9% purity, Sigma-Aldrich) and 5-7 mM Polyethylenimine (PEI, Branched) were prepared at room temperature. GAs were immersed in growth solution when the temperature was at  $85^\circ\text{C}$ . The time duration of this growth was 2 hours for all the GA samples. After the reaction had been completed, GA samples were taken out of the solution and rinsed with de-ionized water and dried at  $100^\circ\text{C}$  on a hot plate for 2 hours. Chemical reactions involved in formation of ZnO nanowires are as follows:



#### 2.3.4 Electrode preparation for Lithium-ion-battery

##### **Microwave Exfoliated Graphene Oxide/TiO<sub>2</sub> Nanowire Hybrid for High Performance Lithium Ion Battery**

For making anodes for both PC and MEGO-TON hybrid electrodes, Polyvinylidene Fluoride (PVDF, MTI corp., purity  $\geq 99.5\%$ ) was used as binding material. PVDF was dissolved in N-Methyl-2-pyrrolidone (NMP, MTI corp., purity  $\geq 99.5\%$ ) at a 1:2.5 weight ratio by heating at  $80^\circ\text{C}$ . Later 80 wt% active material and 10 wt% activated carbon were dispersed in 10 wt% PVDF with excess NPM to prepare homogenous slurry using a homogenizer. Then the slurry was coated on Copper foil and dried at  $100^\circ\text{C}$  on a hot plate. Next, a precision disc cutter from MTI Corporation was used to cut anodes with 13 mm diameter. Later the anodes were kept overnight in a vacuum oven. The anode preparation view is schematically shown in Figure 2.7.

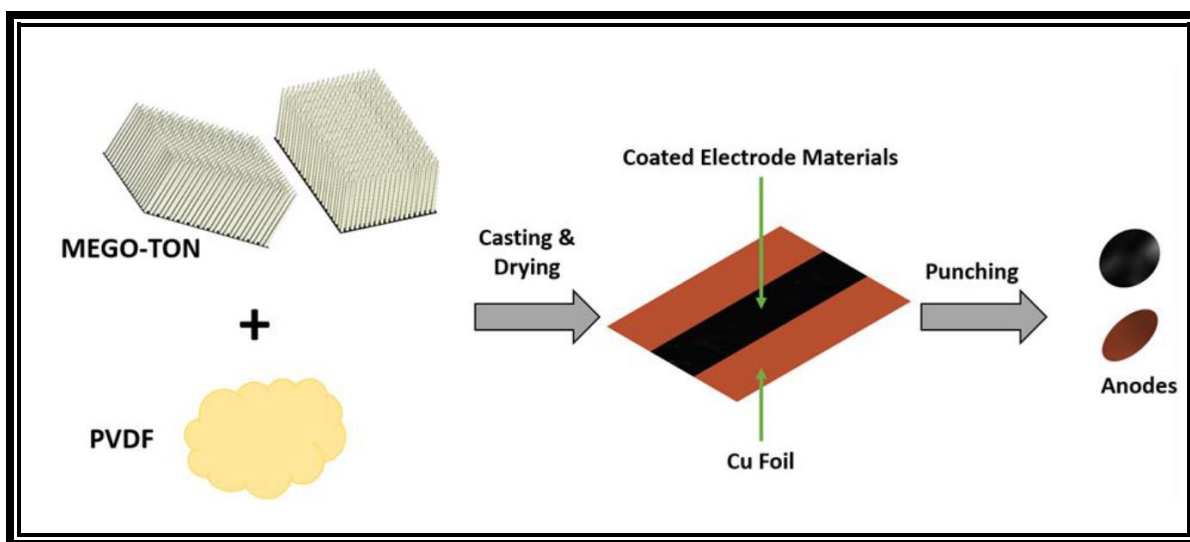


Figure 2.7: Schematic view of anode preparation.

### Porous carbon/CeO<sub>2</sub> composites for Li-ion battery application

For making anodes for both PC and PC-CON electrodes, Polyvinylidene Fluoride (PVDF, MTI corp., purity  $\geq 99.5\%$ ) was used as binding material. PVDF was dissolved in N-Methyl-2-pyrrolidone (NMP, MTI corp., purity  $\geq 99.5\%$ ) at a 1:2.5 weight ratio by heating at 80 °C. Later 80 wt% active material and 10 wt% activated carbon were dispersed in 10 wt% PVDF with excess NPM to prepare homogenous slurry using a homogenizer. Then the slurry was coated on Copper foil and dried at 100 °C on a hot plate. Next, a precision disc cutter from MTI Corporation was used to cut anodes with 13 mm diameter. Later the anodes were kept overnight in vacuum oven.

### Investigation of modified graphene for energy storage applications

For making both graphene and ZnO NWs coated graphene anodes, polyvinylidene fluoride (PVDF, MTI corp., purity  $\geq 99.5\%$ , Molecular Weight 600,000) was used as binding material. PVDF was dissolved in N-Methyl-2-pyrrolidone (NMP, MTI corp., purity  $\geq 99.5\%$ ) at a 1:10 weight ratio by heating at 80 °C. Slurry of 90 wt. % of graphene and 10 wt. % of PVDF was made by using PVDF-NMP solution. For ZnO NWs/graphene, 80: 20 wt. % ratios was used with PVDF. Excess NMP was used to ease the mixing of slurry. Both horn and bath sonication were used to make a homogeneous mixture. Slurry was casted on copper foil and subsequently dried over night

at 120 °C. Precision disc cutter from MTI Corporation was used to cut anodes with 12mm diameter.

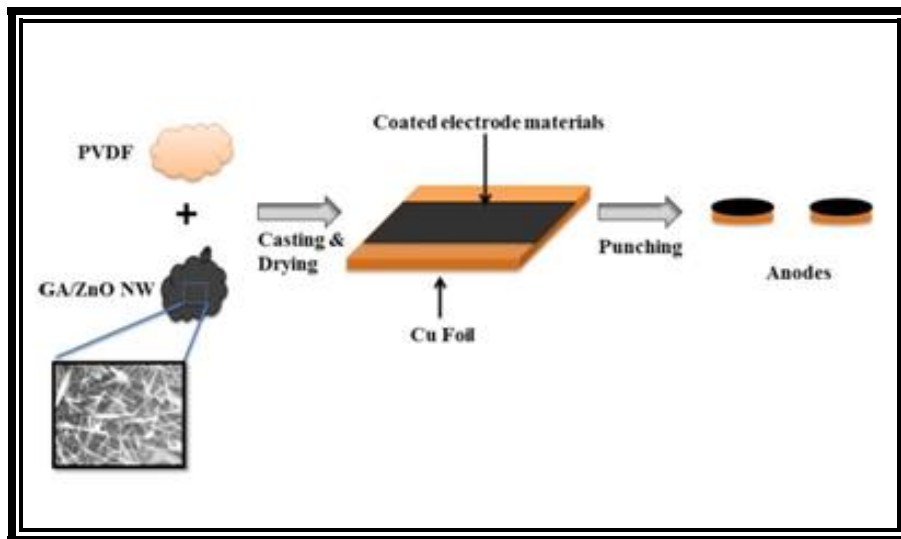


Figure 2.8: Schematic view of anode preparation.

## 2.4 Lithium-ion-battery Assembly

### 2.4.1 Microwave Exfoliated Graphene Oxide/TiO<sub>2</sub> Nanowire Hybrid for High Performance Lithium Ion Battery

All the electrodes were brought into an Argon filled glovebox (Unilab, MBraun) for the super-capacitor coin cell assembly. CR 2032 coin cell cases were purchased from MTI Corporation for the preparation of coin cell lithium-ion-battery. A Hydraulic crimping machine from MTI Corp. was used for the coin cell assembly. For precision measurement of the electrolyte, a micro-pipette was used. Celgard 2500 (25  $\mu\text{m}$  microporous monolayer membrane) with uniform pore structure was used as the separator. Oxygen and moisture level were kept less than 0.1 ppm inside the glovebox. One molar  $\text{LiPF}_6$  in ethylene carbonate (EC), dimethyl carbonate (DMC), and diethyl carbonate (DEC) organic solvent at 1:1:1 volume ratio was used as electrolyte as received (MTI corp.). Metallic lithium foil was used as counter electrode.

A very specific sequence is followed for the assembly of LIBs as shown in Figure 2.9. An anode is placed on positive case facing the active material up. 35  $\mu\text{l}$  of electrolyte is added on anode followed by two separators and in between them another 35  $\mu\text{l}$  of electrolyte is added. After that a lithium foil is placed on the as the counter electrode. The rest of the sequence is as follows: two spacers, spring and top case. Coin cells are sealed by applying 750 psi pressure with a crimping machine (MTI corp.). Excess electrolyte is wiped off after the crimping.

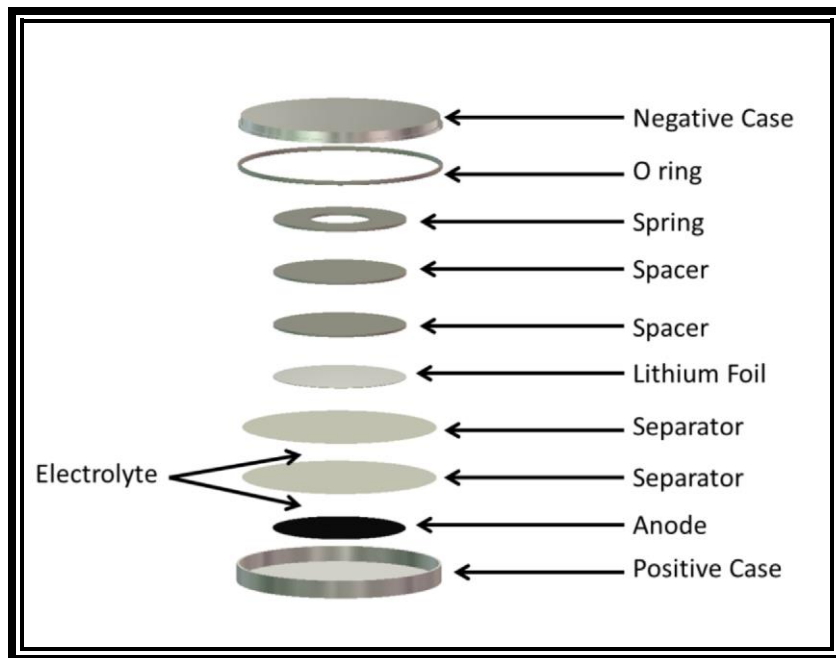


Figure 2.9: Schematic view of coin cell assembly.

#### 2.4.2 Porous carbon/CeO<sub>2</sub> composites for Li-ion battery application

Coin cells (CR 2032) were assembled using either PC anodes or PC-CON anodes inside an Argon filled glovebox (Unilab, MBraun). Oxygen and moisture level were kept less than 0.1 ppm inside the glovebox. One molar LiPF<sub>6</sub> in ethylene carbonate (EC), dimethyl carbonate (DMC), and diethyl carbonate (DEC) organic solvent at 1:1:1 volume ratio was used as electrolyte as received (MTI corp.). Celgard 2500 was used as the separator.

### 2.4.3 Investigation of modified graphene for energy storage applications

All Coin cells (CR 2032) were assembled using either bare graphene anode or ZnO NWs arrays/graphene anode. Each of the anodes was investigated against 12 mm diameter single side LiCoO<sub>2</sub> coated on Al foil as cathode (MTI corp., 0.1 mm thickness). 1 M LiPF<sub>6</sub> in ethylene carbonate (EC), dimethyl carbonate (DMC), diethyl carbonate (DEC) organic solvent at 1:1:1 volume ratio was used as electrolyte as received (MTI corp.). All the batteries were made inside of argon (Purity 99.999%) filled glove box (LABstar, MBraun) where oxygen and moisture content were kept less than 0.01 ppm. Cross sectional view for coin cell assembly is shown in Figure 2.10.

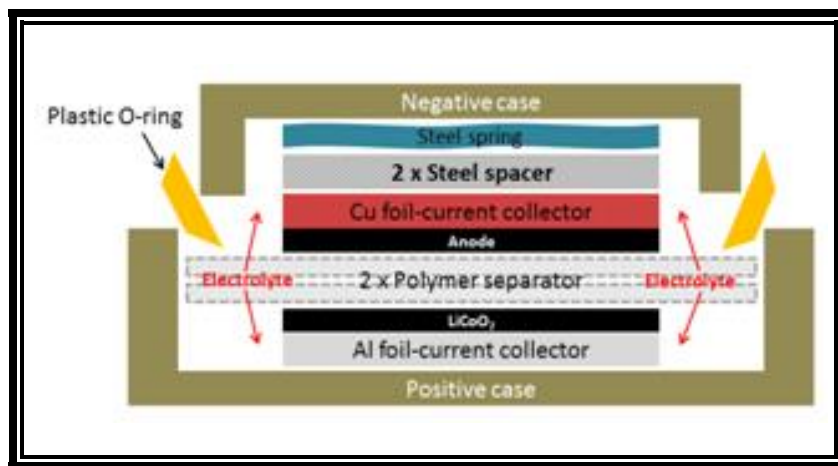


Figure 2.10: Schematic view of coin cell assembly.

## **Chapter 3: Super-capacitor**

This chapter is intended to describe all the characterization procedures which were performed to determine the morphology, crystal information, and gravimetric analysis of the samples after the chemical synthesis. Scanning Electron Microscopy (SEM) and Transmission Electron Microscopy (TEM) were performed to see the morphology and acquire information regarding the particle sizes of the sample. X-ray Diffraction was also performed to determine the crystal structure of the sample. Later, Thermo-gravimetric Analysis (TGA) was also carried out to quantify the amount of nanoparticles were present within the sample.

The next portion of this chapter discusses the principles of the electrochemical testing procedures. Three types of electrochemical techniques, i.e., Cyclic Voltammetry (CV), Galvanostatic Charge-discharge Testing, and Electrochemical impedance Spectroscopy (EIS) were utilized for this research for evaluating the super-capacitor performance. Later, all results from these testing are presented and discussed to for understanding the electrochemical kinetics of the super-capacitors.

### **3.1 Characterization**

#### **3.1.1 Scanning Electron Microscopy (SEM)**

##### **High-performance Porous Carbon/CeO<sub>2</sub> Nanoparticles Hybrid Super-capacitors for Energy Storage**

Hitachi S-4800 Scanning Electron Microscope used to characterize the samples. Figure 3.1 is the SEM image for the PC-CON sample. The black surface belongs to the porous carbon and it is clearly visible from the image that white spheres are on the surface and nooks of the sample. The morphology of the porous carbon is clearer from Figure 3.3 (a) and figure 3.2 (b) shows that there was good amount of CeO<sub>2</sub> coverage all through the samples. The particle size was determined out of the transmission electron microscopic (TEM) images.

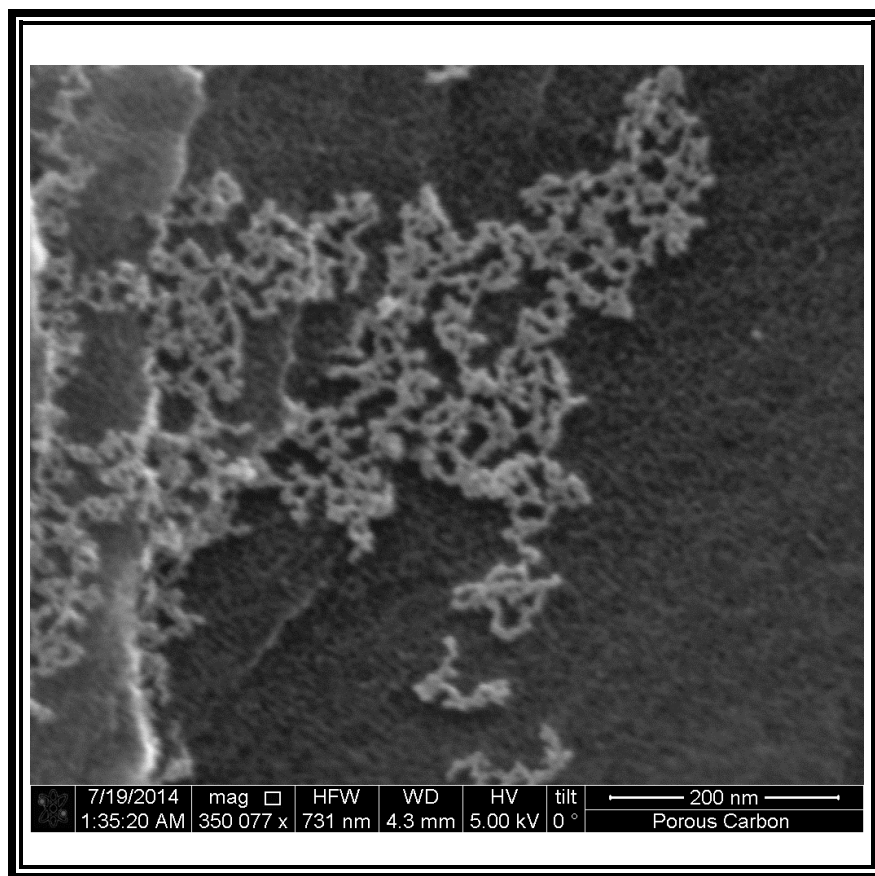


Figure 3.1: SEM of PC-CON sample.

### **Nanowire Modified Carbon Fibers for Enhanced Electrical Energy Storage**

The morphology of zinc oxide nanowires grown on carbon cloth was analyzed with scanning electron microscope as shown in Figure 3.2. As indicated by the figure, ZnO nanowires were grown uniformly throughout the carbon fiber. The nanowires had a length between 1 to 3.14  $\mu\text{m}$  and diameter between 40 to 110 nm. No residue or flower was found.

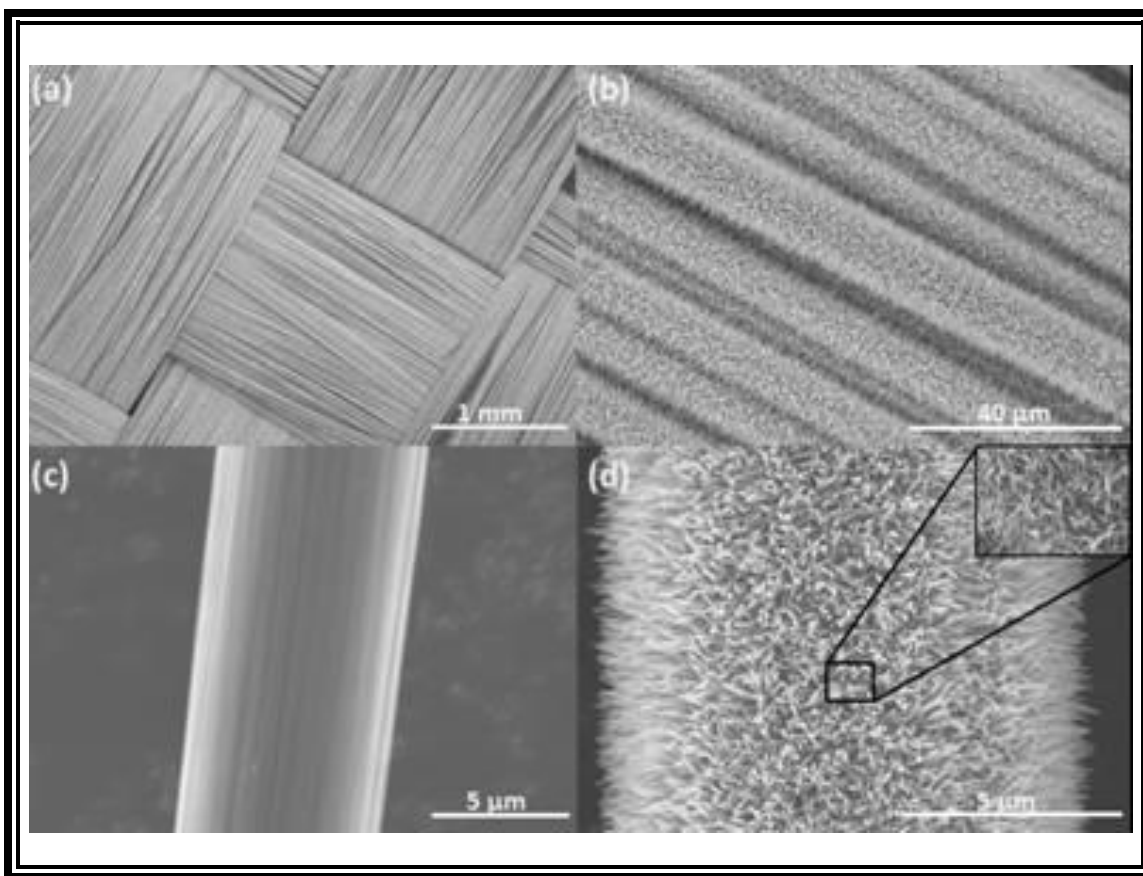


Figure 3.2: SEM images, (a, b, and d) ZnO/Carbon Fiber, (c) Bare carbon fiber.

### 3.1.2 Transmission Electron Microscopy (TEM)

#### High-performance Porous Carbon/CeO<sub>2</sub> Nanoparticles Hybrid Super-capacitors for Energy Storage

A TEM was used to observe the particle size and lattice fringes in the sample through TEM and HRTEM images. The powder sample was mounted through a copper grid in the TEM. Figure 3.3 (c) shows the TEM image for the CeO<sub>2</sub> nanoparticles which had a diameter between 6 to 8 nm. Clear lattice fringes were observed in HRTEM image (Figure 3.3 (d)), which confirms the formation of crystalline particles formed in the hydrothermal reaction. The lattice spacing of 0.31 nm confirms that single crystal CeO<sub>2</sub> was synthesized.



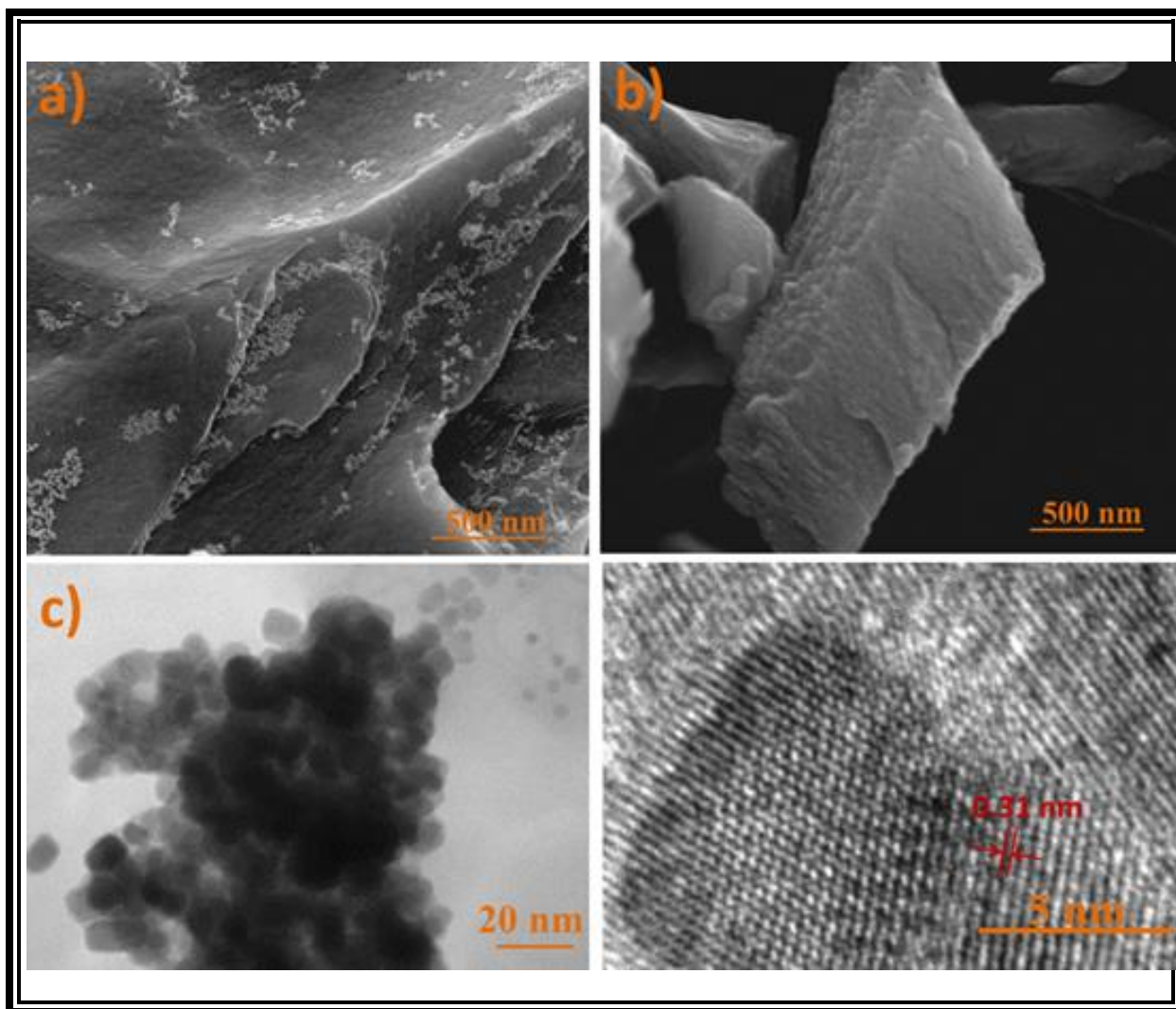


Figure 3.3: (a) SEM image of CeO<sub>2</sub> nanoparticles on porous carbon, (b) morphology of porous carbon, (c-d) TEM & HRTEM images of CeO<sub>2</sub> nanoparticles.

### 3.1.3 X-ray Diffraction (XRD) for PC-CON

#### High-performance Porous Carbon/CeO<sub>2</sub> Nanoparticles Hybrid Super-capacitors for Energy Storage

The crystal structures of the PC-CON hybrid before and after heat treatment were determined utilizing a Bruker D8 Discover XRD using Cu K $\alpha$  radiation (Figure 3.4). The precursor sample shows very weak crystal peaks, indicating more amorphous nature, whereas the sample after heat treatment exhibit XRD peaks that correspond to the (111), (200), (220), (311), and (222) planes of a cubic fluorite structure CeO<sub>2</sub> (space group: Fm3m), which is in agreement

with the JCPDS file for  $\text{CeO}_2$  (JCPDS 34-0394). It is shown that the reflection peaks become sharper and narrower after heat treatment, indicating that the crystal size increases, and the crystallinity of  $\text{CeO}_2$  becomes better defined. The values of lattice parameters  $a$  calculated from the XRD spectra before and after heat treatment are 0.534 and 0.544 nm respectively. It is noted that the values of lattice parameter  $a$  for the sample before heat treatment is lower than the heat treated sample. Our results are in agreement with those of Leoni et al., who reported that the lattice parameter of nano-crystalline  $\text{CeO}_2$  powder changes as a function of temperature [86]. No extra peaks corresponding to any other secondary phases were observed.

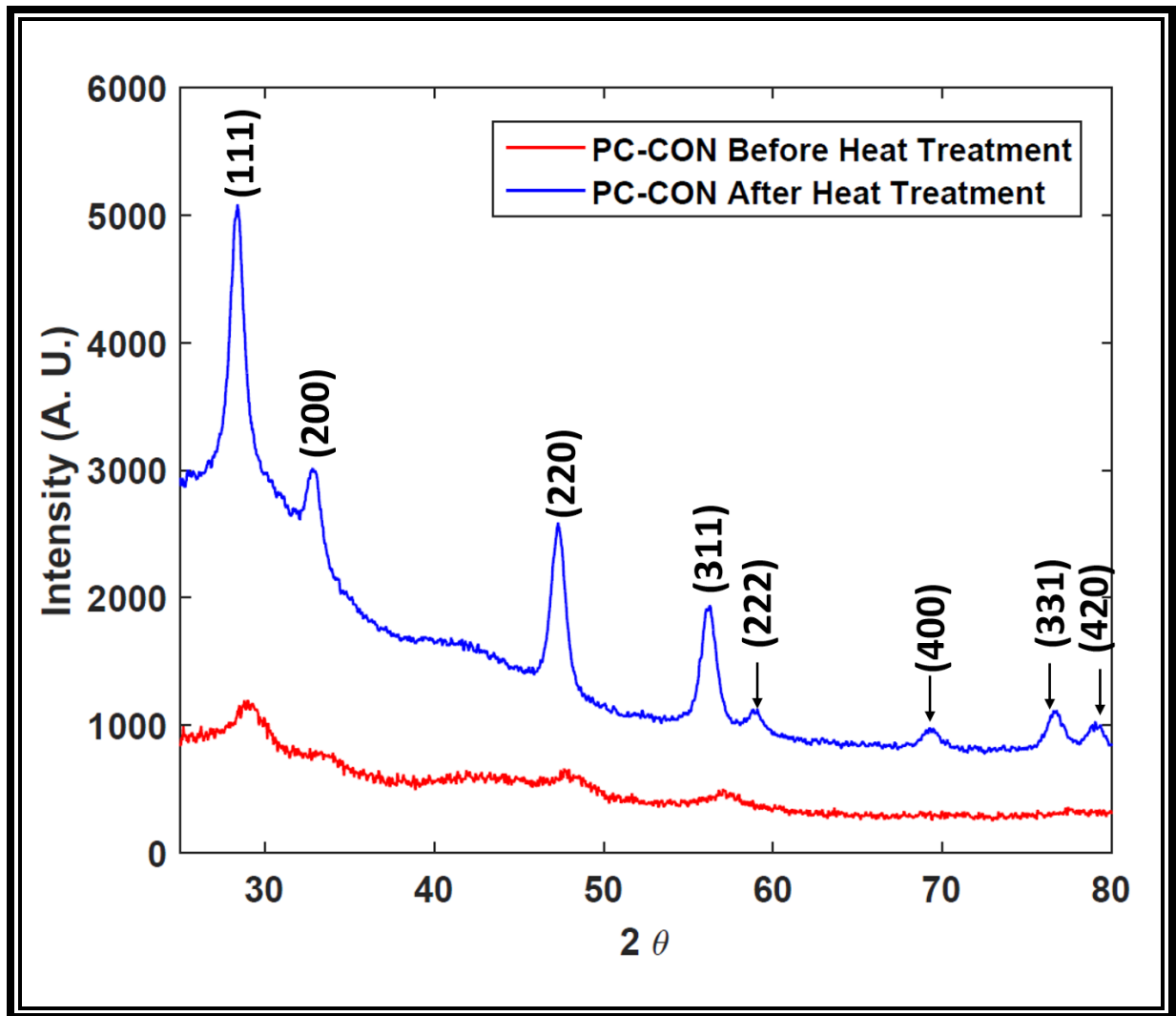


Figure 3.4: XRD results for PC-CON before and after heat treatment.

## Nanowire Modified Carbon Fibers for Enhanced Electrical Energy Storage

The XRD scanning result of the ZnO nanowires on carbon cloth is shown in Figure 3.5. The asterisk (\*) marked peak represents carbon of rhombohedra crystal structure. The scan result matched with the standard card JCPDS (01-075-0444) and has lattice parameters of  $a=2.29597$ ,  $b=2.29597$  and  $c=10.15404$ . The rest of the peaks represent zinc oxide which matched with the standard card JCPDS (01-070-8070). The lattice parameters for hexagonal zinc oxide are  $a=3.24890$ ,  $b=3.24890$  and  $c=5.20490$ . No other peaks were found which indicates the sample has only zinc oxide and carbon.

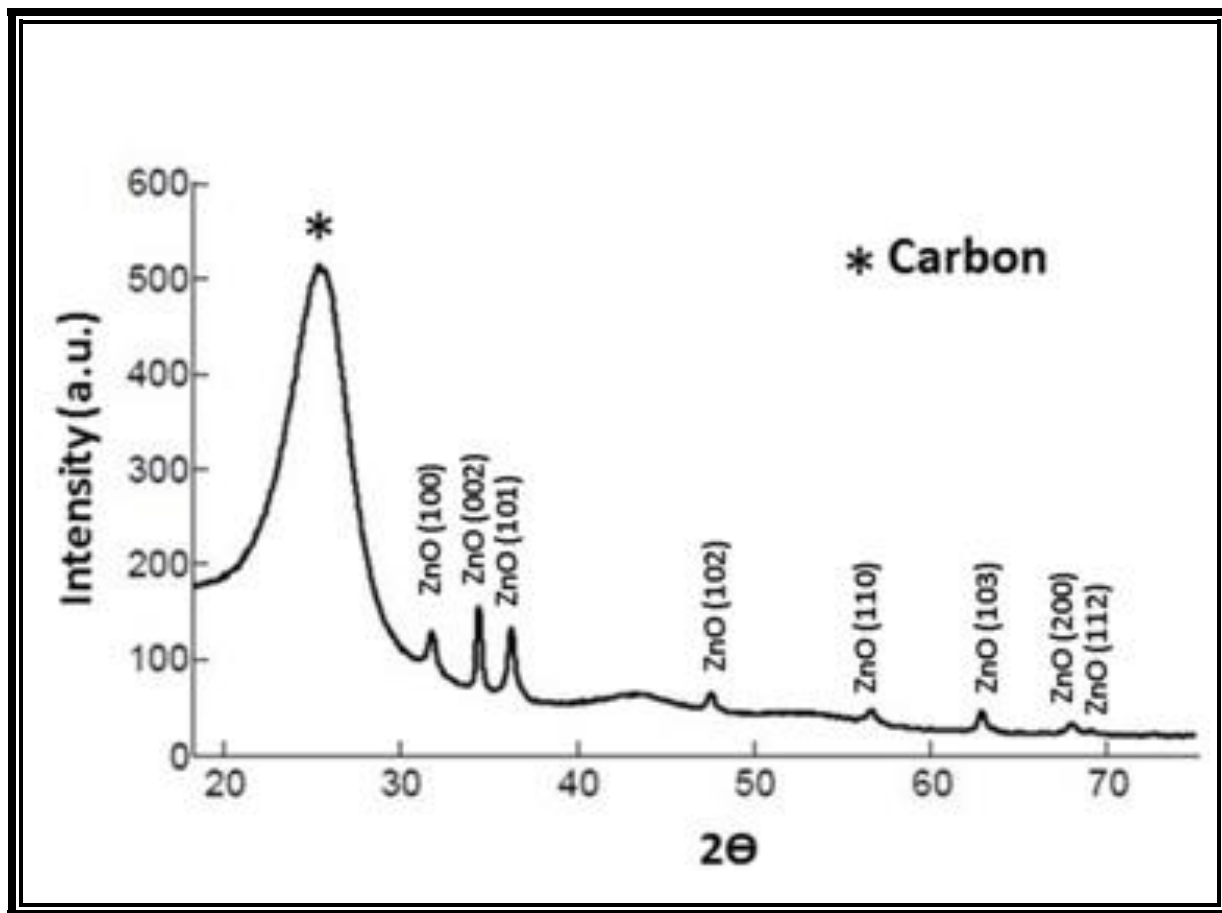


Figure 3.5: XRD result for ZnO NWs coated carbon cloth. Asterisk (\*) peak is for carbon. The rest of the peaks belong to ZnO.

### 3.1.4 Thermogravimetric Analysis (TGA)

#### High-performance Porous Carbon/CeO<sub>2</sub> Nanoparticles Hybrid Super-capacitors for Energy Storage

Another characterization performed on the materials was thermogravimetric analysis (TGA) to quantify the amount of CeO<sub>2</sub> nanoparticles present in the PC-CON sample using TG 209 F1 Iris. The ramp rate was 20° C/minute up to 1000° C in presence of oxygen and the temperature was kept at 1000° C for 30 minutes. The TGA profile presents a sharp weight loss at around 350° C and this sharp weight loss is accompanied by a heat release which can be observed in the temperature profile. Due to the presence of oxygen, all porous carbon started to oxidize at this point and during the hold time all porous carbon got oxidized leaving the CeO<sub>2</sub> particles only. The amount for CeO<sub>2</sub> particle calculated is around 44 wt % of the PC-CON composites.

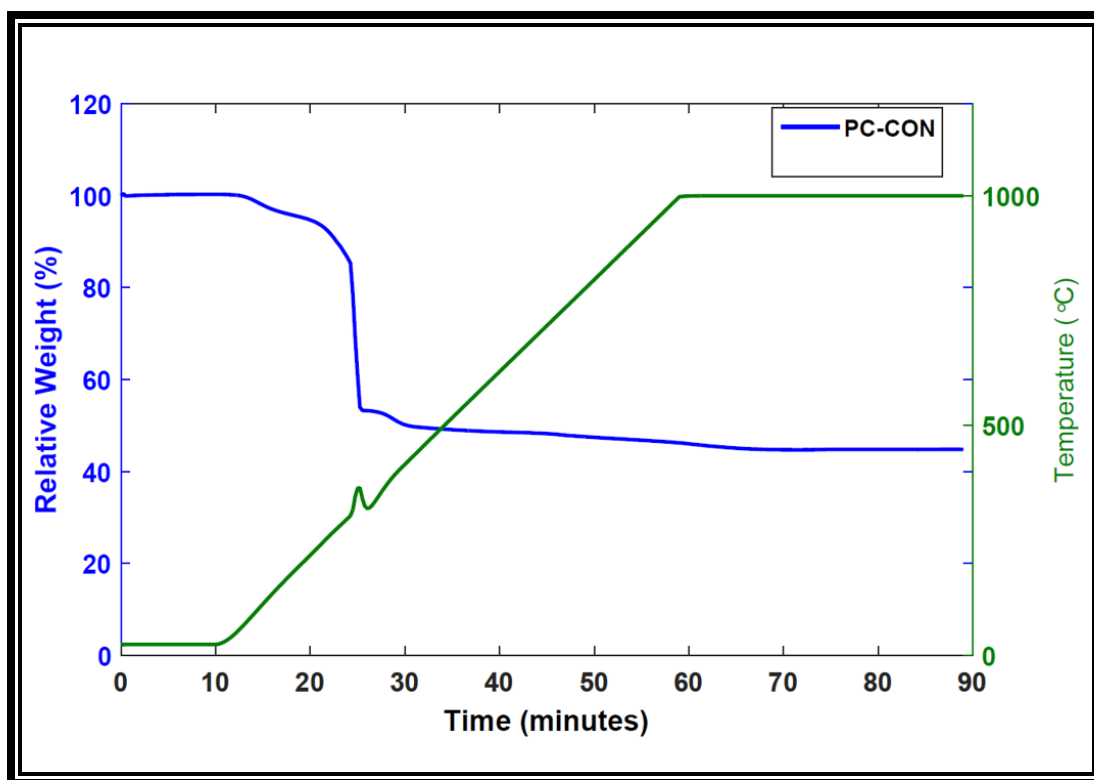


Figure 3.6: TGA of PC-CON sample.

### 3.1.5 X-ray Photoelectron Spectroscopy (XPS)

#### High-performance Porous Carbon/CeO<sub>2</sub> Nanoparticles Hybrid Super-capacitors for Energy Storage

In order to determine the chemical composition and oxidation state of the electrode materials before and after the electrochemical testing, X-ray photoelectron spectroscopy (XPS) measurements were carried out in the region of 0-1200 eV. The deconvoluted XPS spectra of the Ce 3d core electrons for the before and after testing electrodes are shown in Figure 3.7. For both spectra, the first four well resolved peaks in the range of 880-901 eV correspond to Ce 3d<sub>5/2</sub>, whereas the last two peaks in the range of 907-917 eV correspond to 3d<sub>3/2</sub>. Although, most of the Ce were in Ce<sup>+4</sup> state, which was also confirmed by XRD analysis, the presence of Ce<sup>+3</sup> is clearly revealed from the XPS spectra of the before and after testing electrode.

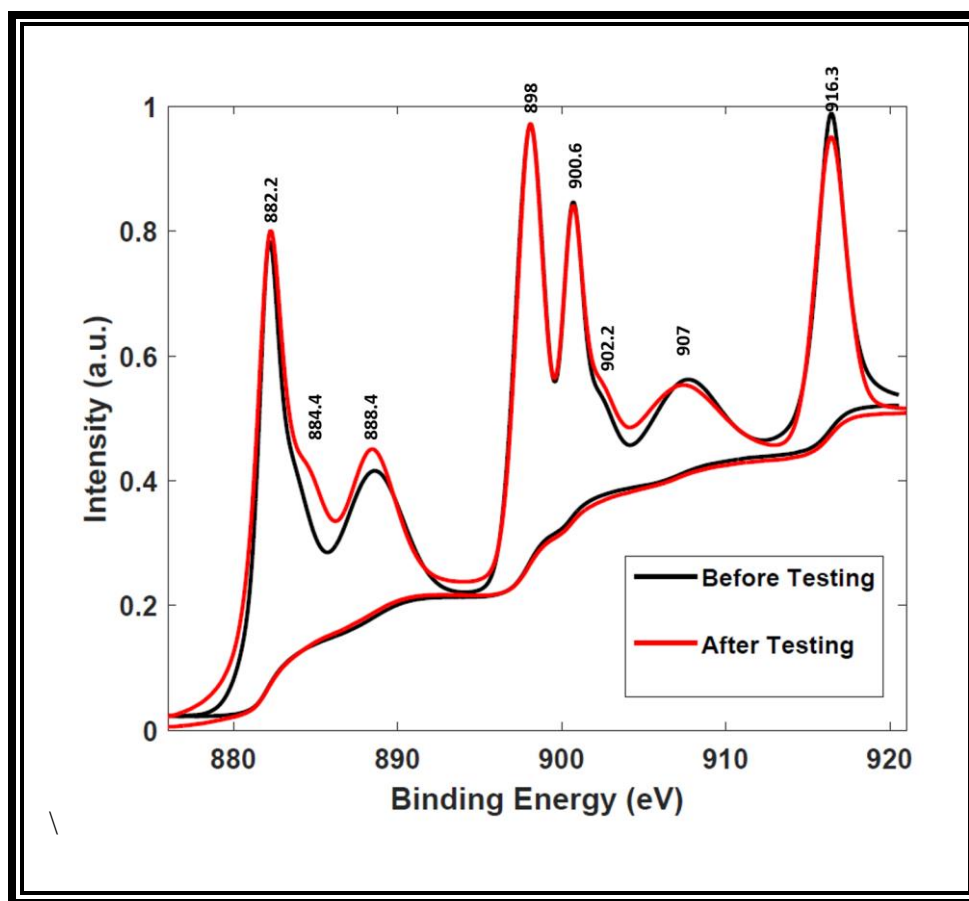


Figure 3.7: High resolution XPS spectrum of Ce 3d for before and after testing electrodes.

From XRD result, it was clear that  $\text{CeO}_2$  possesses a cubic fluorite structure (space group:  $Fm-3m$ ). The  $\text{Ce}^{+4}$  cation are surrounded by  $\text{O}^{2-}$  anions in the cubic crystal, each of which is coordinated to four  $\text{Ce}^{+4}$  cation. The shoulder satellite peak at  $\sim 884.4$  eV and a tiny peak at  $\sim 902.2$  eV in the Ce 3d spectrum, corresponding to  $\text{Ce}^{+3}$  state, suggests the presence of oxygen vacancies in  $\text{CeO}_2$ . The quantitative investigation revealed that the concentration of  $\text{Ce}^{+3}$  in the before testing sample was  $\sim 13.6\%$  and found to be lower than the concentration of  $\text{Ce}^{+3}$  ( $\sim 13\%$ ) in the case of after testing sample. From the electrochemical testing result, it was found that after several cycles of testing the specific capacitance drops a little, which can be attributed to the lower amount of oxygen vacancies in  $\text{CeO}_2$ .

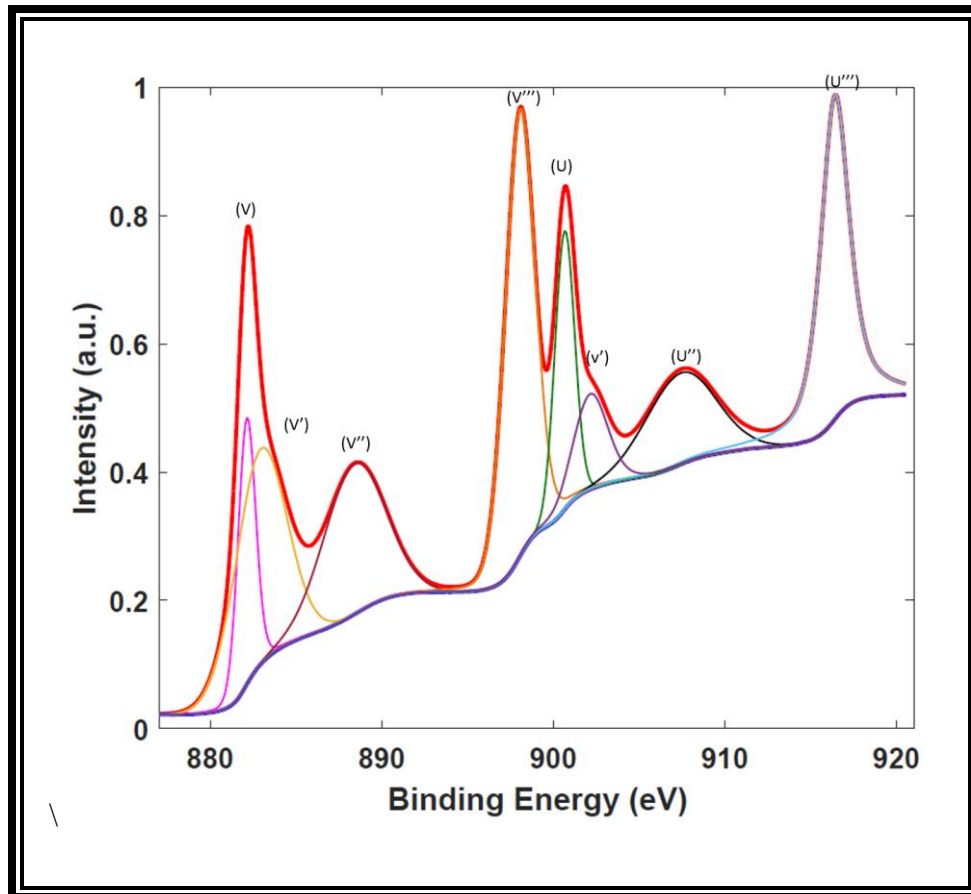


Figure 3.8: XPS Ce 3d spectra of before testing electrode.

The quantitative analysis for the concentration of  $\text{Ce}^{+3}$  in before and after testing samples has been done. As shown in Figure 3.8 and 3.9, high resolution XPS spectra of Ce3d core were deconvoluted by mean of Gaussian-Lorentzian shape fitting using XPS peak fit software. The Ce 3d XPS spectra exhibit multiple states which arise from different Ce 4f level occupancies in the final state and can be marked according to the convention established by Burroughs et al. [87], where V and U refer to the  $3d_{5/2}$  and  $3d_{3/2}$  spin-orbital components.

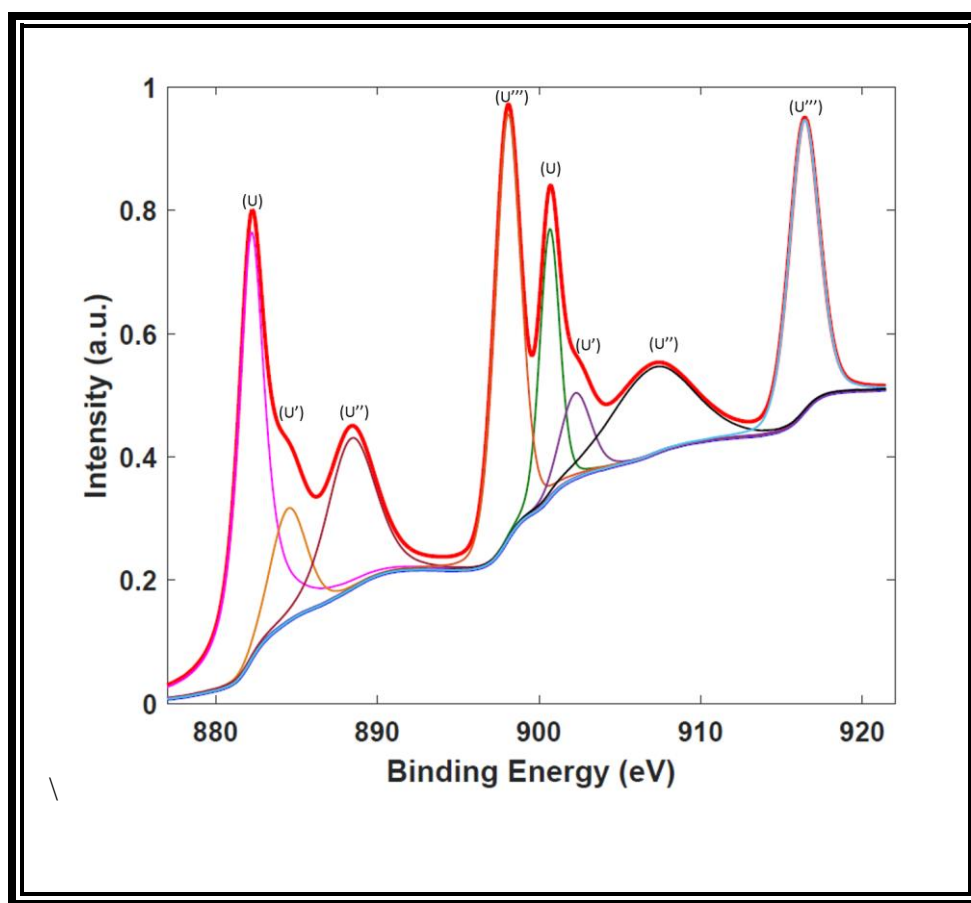


Figure 3.9: XPS Ce 3d spectra of after testing electrode.

The peaks labelled as U, U'', U''', V, V'', and V''' are corresponding to the features of  $\text{Ce}^{4+}$ , whereas; peaks referred to V' and U' are corresponding to  $\text{Ce}^{+3}$  was calculated by taking the ratio of the integrated peak areas corresponding to the  $\text{Ce}^{+3}$  to the total area under the whole Ce 3d

spectrum. Our estimate of  $Ce^{+3}$  concentrations in before and after testing samples was determined using the following equation [88]:

$$Ce^{+3} = \frac{A_{vo} + A_{v'} + A_{uo} + A_{u'}}{A_{vo} + A_{v'} + A_{uo} + A_{u'} + A_v + A_{v''} + A_{v'''} + A_u + A_{u''} + A_{v'''}}$$

where, A denotes the area of the corresponding peaks marked as the subscript in the spectrum. The relatively higher concentration of  $Ce^{+3}$  suggests the higher oxygen vacancies in the samples.

### 3.2 Testing and Discussion

Three different techniques, i.e., cyclic voltammetry, galvanostatic charge-discharge testing and electrochemical impedance spectroscopy, were utilized for evaluating the electrochemical performance of the super-capacitor. A potentiostat galvanostat from EZ-stat was utilized for the first two techniques and a HP 4284A LCR meter at 1 V<sub>rms</sub> with a parallel equivalent circuit setup which has a frequency range from 100 Hz to 1 MHz was used for the impedance data. The EZ-stat as shown in 3.10 has a testing software which has the capability to perform cyclic voltammetry and galvanostatic charge-discharge testing using different parameters.

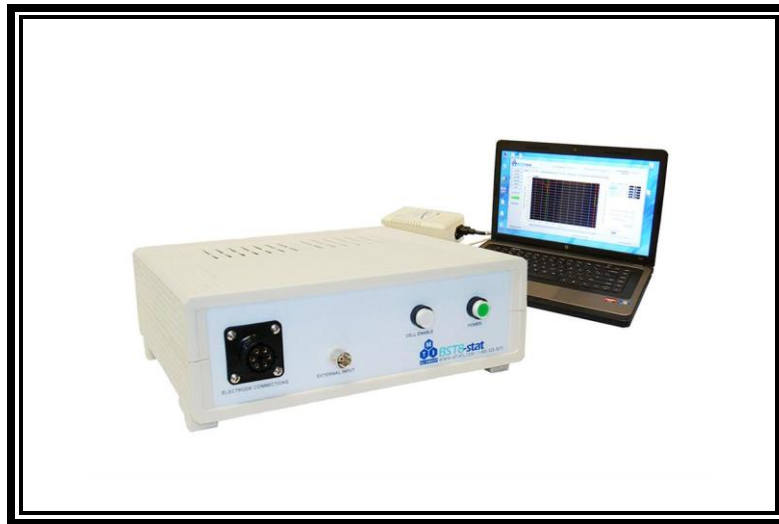


Figure 3.10: EZ-stat for electrochemical testing.



In order to determine the impedance and phase angle value the following LCR meter as shown in Figure 3.11 was used for the electrochemical impedance spectroscopy.



Figure 3.11: LCR meter used for electrochemical impedance spectroscopy.

### 3.2.1 Cyclic Voltammetry (CV)

Due to the versatility of cyclic voltammetry, this testing technique is widely used for electrochemical measurement but most of the time it is laboratory cell evaluation. This is an accurate technique for lab scale which enables:

- Pseudo-capacitive and qualitative studies
- Understanding the kinetics by scanning a huge range of scan rate
- Determination of voltage window

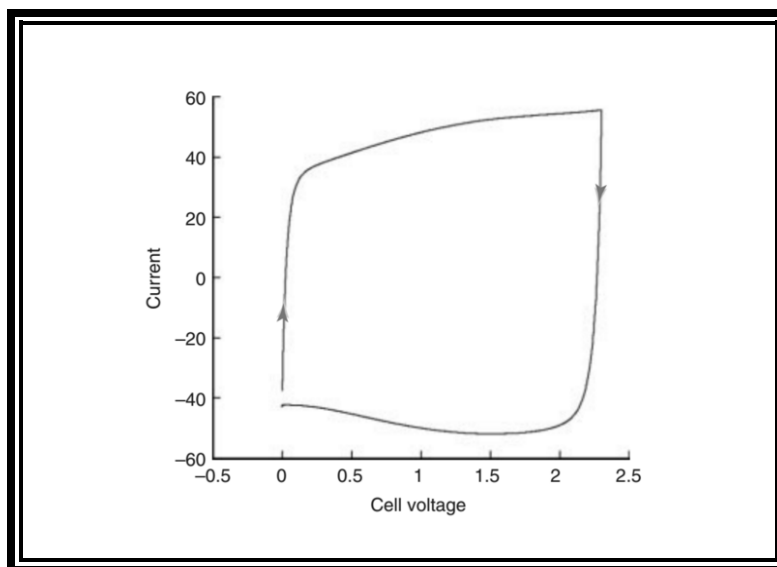


Figure 3.12: Cyclic voltammetry of an EDLC super-capacitor [21].

A linear voltage ramp is applied to an electrode between two voltage limits and the resulting current is measured. The applied voltage is as follows:

$$V(t) = V_0 + vt \text{ for } V \leq V_1$$

$$V(t) = V_0 - vt \text{ for } V \geq V_2$$

where,  $v$  is the scan rate ( $\text{V s}^{-1}$ ) and  $V_1$  and  $V_2$  are the two voltage boundaries. A typical  $i$ - $V$  curve obtained from this CV technique for super-capacitor and Figure 3.12 shows the cyclic voltammetry obtained from an EDLC super-capacitor with organic electrolyte [21].

### High-performance Porous Carbon/CeO<sub>2</sub> Nanoparticles Hybrid Super-capacitors for Energy Storage

Thi After fabricating coin cell super-capacitor using porous carbon/CeO<sub>2</sub> nanoparticle hybrid, cyclic voltammetry was performed to evaluate the electrochemical performance of the fabricated electrode. 0-2.2V was used as the voltage window and different scan rate was used for getting the CV curves.

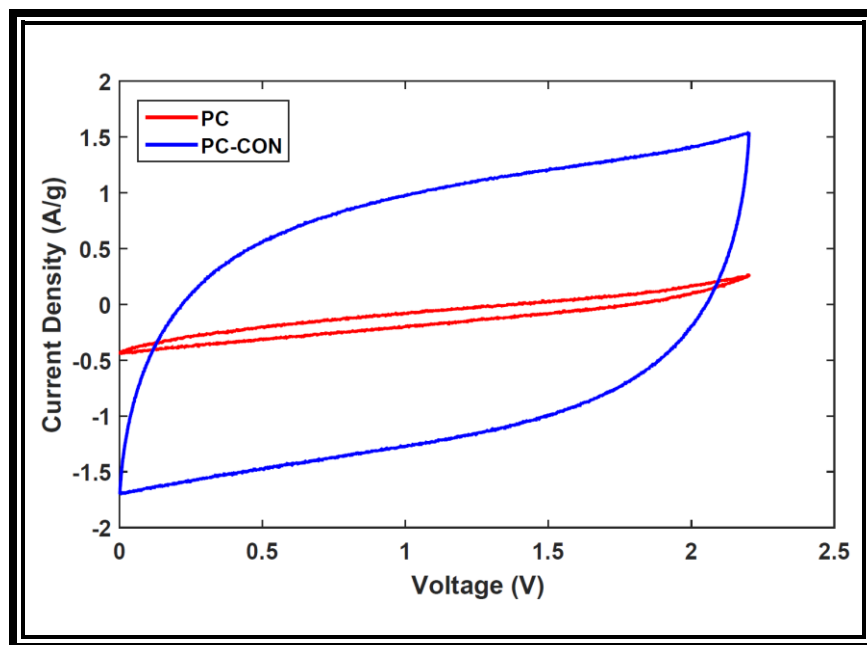


Figure 3.13: CV curves of PC and PC-CON at a scan rate of 50 mV/s.

Figure 3.13 shows the CV curves of the two samples at a scan rate of 50 mV/s in the potential window of 0~2.2 V and the area under the CV curve for PC-CON sample is larger than the PC sample which suggests that the PC-CON sample has higher specific capacitance [89]. The peak current density of PC-CON electrode is ~6 times higher than the PC electrode, indicating PC electrode delivered negligible capacitance. The evidently observed quasi rectangular shape of the CV of PC-CON electrode indicates the existence of dual behavior of electric double layer and pseudo-capacitance nature of the electrode [90]. The absence of oxidation and reduction peaks in the PC-CON electrode suggests that the super-capacitor is charged and discharged at a pseudo constant rate over the complete voltammetric cycles [16, 91].

Similar CV curve was obtained for 100 mV/s scan rate. The area of each CV curve for each sample was increased and the curves distorted more from the rectangular nature. Figure 3.14 shows the CV curves at 100mV/s scan rate.

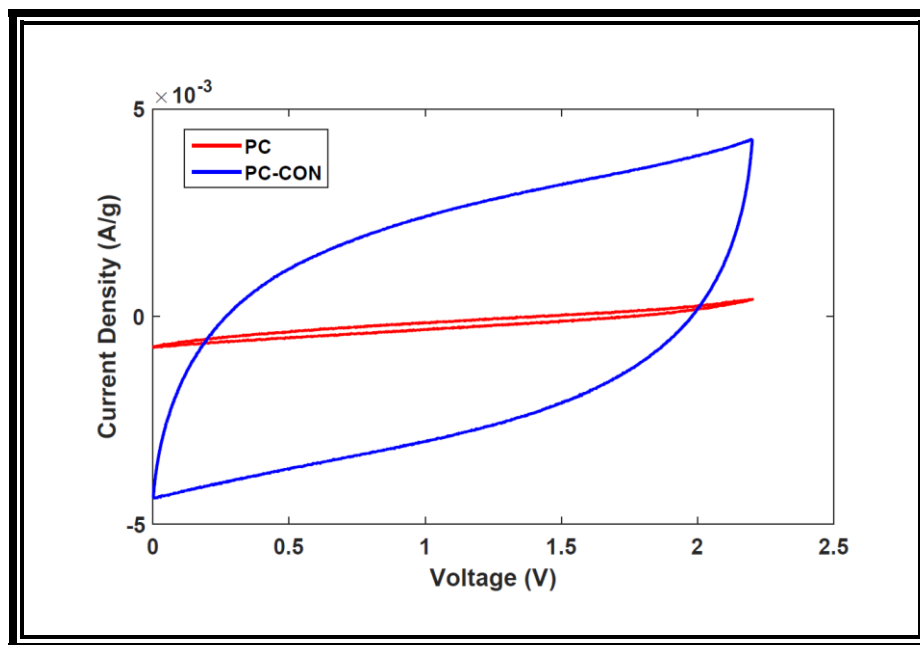


Figure 3.14: CV curves of PC and PC-CON at a scan rate of 100 mV/s.

Figure 3.15 shows the CV curves of PC-CON electrode at different potential scan rates. At lower potential scan rates, PC-CON electrode showed almost perfectly rectangular shapes, representing an ideal capacitive behavior. With increasing potential scan rate, the CV curves are significantly distorted due to the limited ion incorporation into the active material; only the outer surface or subsurface is utilized for charge storage [16].

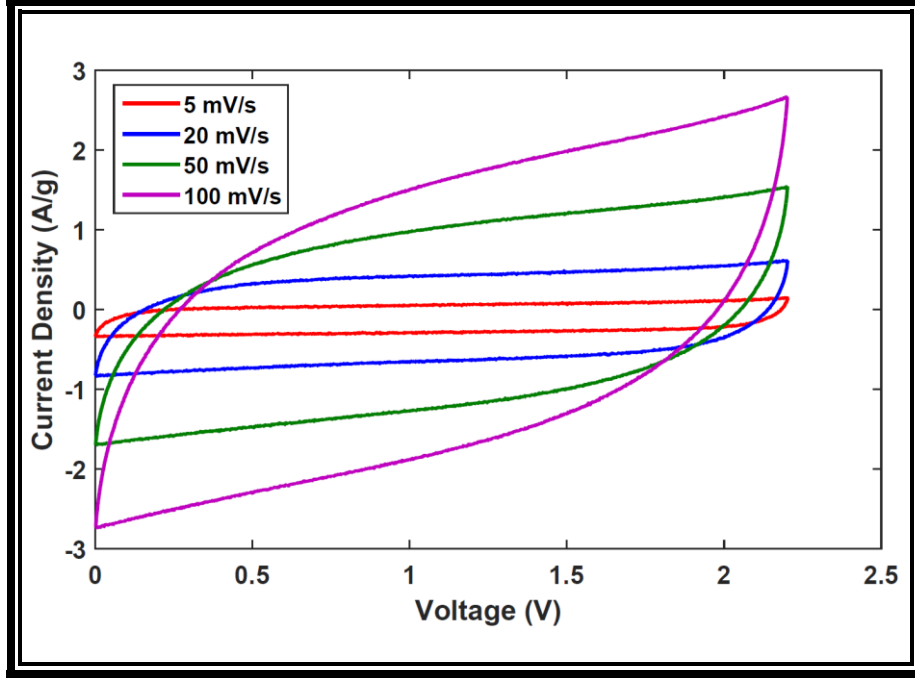
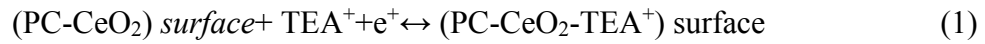
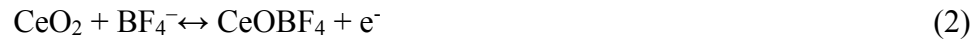


Figure 3.15: CV curves of PC-CON at different scan rates.

Paragraphs The non-faradic reaction of  $\text{CeO}_2$  may be due to the formation of double layer at the electrode/electrolyte interfaces during insertion/de-insertion of positive ions ( $\text{TEA}^+$ ) and the reaction is described by equation (1) as follows;



Moreover, the observed faradic reaction process causes a slight deviation of rectangular shape in the CV curves for all potential scan rates due to the reversible reactions of  $\text{Ce}^{3+}/\text{Ce}^{4+}$  associated with  $\text{BF}_4^-$  anions. The equation for the possible reversible process can be explained as follows (2);



The PC-CON sample could provide faster transport of electron/ion and more pathways for these charge carriers, thus leading to rapid and reversible reactions as described by equation 1 and 2 and therefore to ideal rectangular CV curves (particularly at low scan rates). Furthermore, the porous carbon acts as an efficient current collector. Thus, it can be implied that the porous carbon network may improve not only the conductivity of the hybrid but also the charge transfer rate of

the PC-CON electrodes due to enriched interface between CeO<sub>2</sub> and porous carbon during hybridization. With such an orderly nano/micro hybrid structures, the CeO<sub>2</sub> nanoparticle with porous carbon showed an outstanding capacitive behavior, while maintaining high capacitance at high cycling rates.

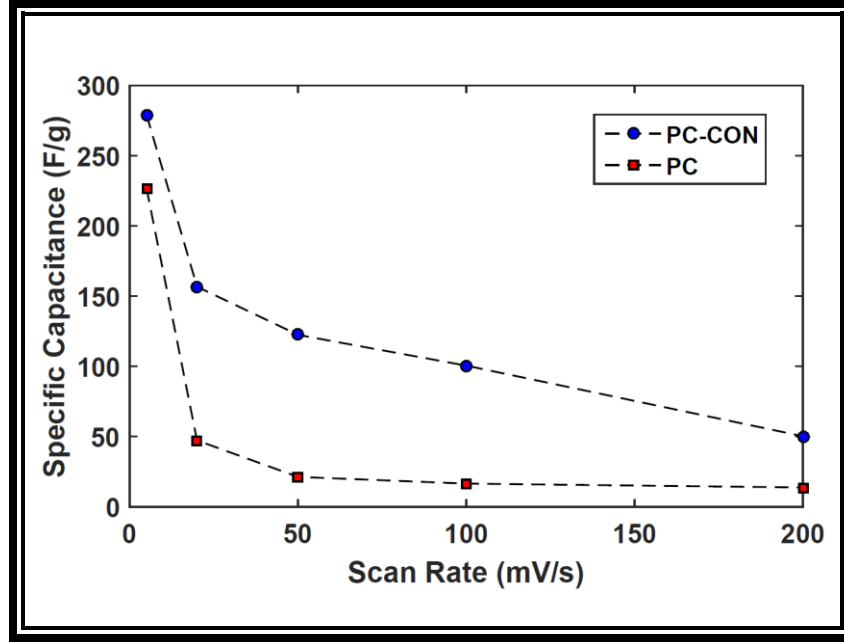


Figure 3.16: Average specific capacitance of PC and PC-CON at different scan rates.

Figure 3.16 compares the average specific capacitance of PC and PC-CON samples as a function of scan rates and the specific capacitance was calculated from the CV curves using the following equation [92]:

$$C_s = \frac{1}{vw\Delta V} \int_{V_a}^{V_c} iVdV$$

where,  $\Delta V$  (V) is the applied potential window ( $V_a$  to  $V_c$ ),  $v$  ( $\text{mV s}^{-1}$ ) is the scan rate, and  $w$  (g) is the weight of the active material. In the scan rate range investigated, the PC-CON electrode yielded substantially higher specific capacitances than PC electrode. For example, the specific capacitance for the PC-CON electrode was 280 F/g at scan rate of 5 mV/s, which was more than

that of PC electrode (226 F/g at scan rate of 5 mV/s). Compared to bare PC, the PC-CON electrode not only exhibits higher specific capacitance at high rates of between 20-200 mV/s, but also presents better rate capability.

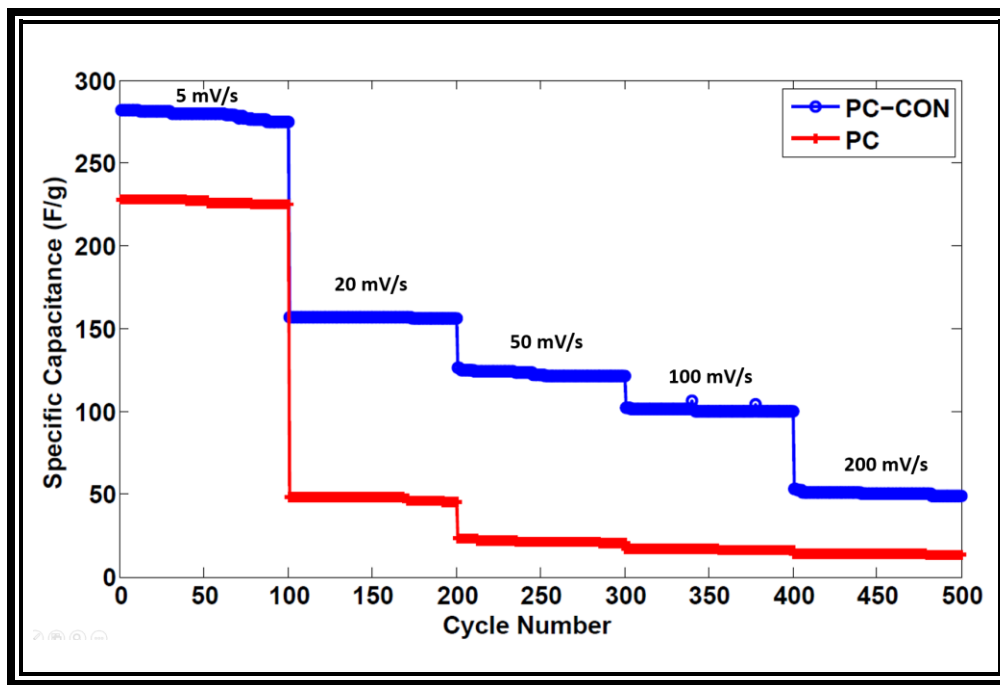


Figure 3.17: Cycling performance of PC and PC-CON electrodes at different scan rates.

To evaluate the durability of the PC and PC-CON electrodes, cyclic voltammetry was carried out to characterize long term charge discharge at scan rate ranges 5-200 mV/s for 500 cycles and the PC-CON electrode displayed remarkable electrochemical stability up to 500 cycles at each scan rate (Figure 3.17). As previously mentioned, the specific capacitance decreases with the increase of potential scan rates due to limited ion incorporation into the active material.

### 3.2.2 Galvanostatic Charge-discharge Testing

This testing technique is different from cyclic voltammetry and in this case, constant current sweep is applied to the cell while the voltage is measured. This technique is widely used

from laboratory to industry. Another name of this technique is chronopotentiometry and different parameters can be accessed throughout this technique such as

- Resistance
- Capacitance
- Cyclability

Following equation can describe the voltage variation during galvanostatic charge discharge testing:

$$V(t) = Ri + \frac{t}{C}i (V)$$

Voltage variation of a typical super-capacitor due to a constant current is represented in Figure 3.18. Capacitance is calculated from the discharge slope of the curve; for a pseudo-capacitor, when the discharge slope is not linear, the capacitance is usually calculated by integrated the current over the discharge time [21].

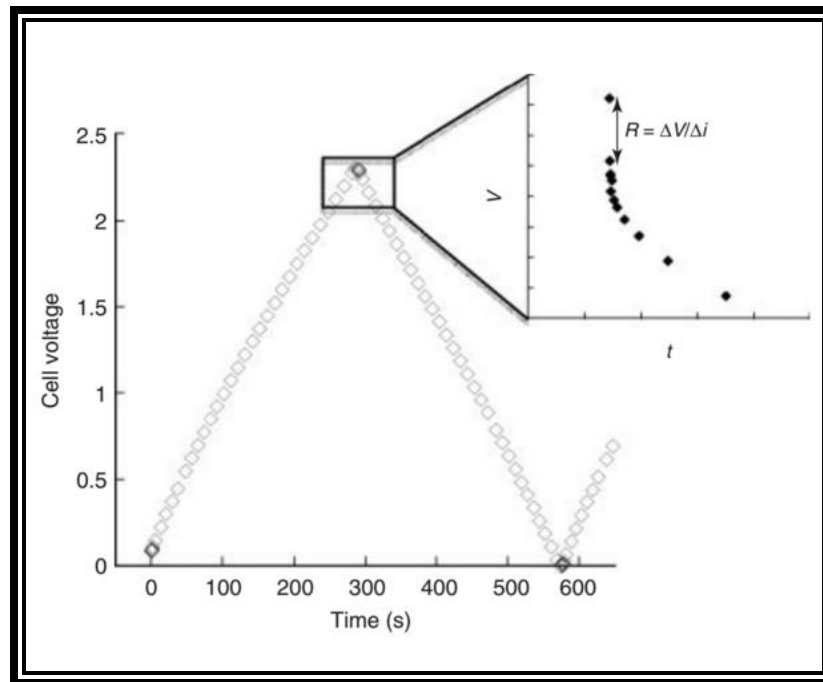


Figure 3.18: Galvanostatic charge discharge curve for a super-capacitor. Inset: zoom-in of the current inversion region [17].



Following are the equations used for calculating specific capacitance for a super-capacitor using galvanostatic charge discharge curve:

$$C = I \frac{\partial t}{\partial V}$$

$$C = \frac{I \Delta t}{\Delta V}$$

where,  $I$  is the constant current,  $\Delta t$  is the discharge time, and  $\Delta V$  is the voltage window.

Equivalent series resistance can be deducted from the voltage drop ( $V_{drop}$ ) occurring over the current inversion ( $\Delta I$ ) using the following equation; it is illustrated in the inset of Figure 3.18:

$$R = \frac{V_{drop}}{\Delta I} (\Omega)$$

When there is inversion or interruption of current, the voltage drop is directly linked to the resistance of the cell. The cyclability of a super-capacitor can also be determined repeating the capacitance and resistance measurement over cycling.

### **High-performance Porous Carbon/CeO<sub>2</sub> Nanoparticles Hybrid Super-capacitors for Energy Storage**

Figure 3.12 shows the charge-discharge curves for PC and PC-CON sample. As per the figure, the discharging time of PC-CON electrode was increased in comparison with PC electrode at both high and low current densities; indicating that the PC-CON hybrid provided higher charge capacity, which was consistent with CV curves. In addition, the voltage-time profile for the charging and discharging of PC-CON electrode was linear and symmetric, a sign of high Coulombic efficiency and excellent reversibility. Conversely, the discharge profiles consist of two parts: a resistive component because of the sudden voltage drop representing the voltage change due to the equivalent series resistance (ESR) and a capacitive component related to the voltage change due to the change in energy within the capacitor. It was shown from the figure that the PC-CON electrode displayed much lower ESR than the PC electrode at a constant current density which is further confirmed by electrochemical impedance spectroscopy (EIS), as shown in Figure 3.19 and 3.20.

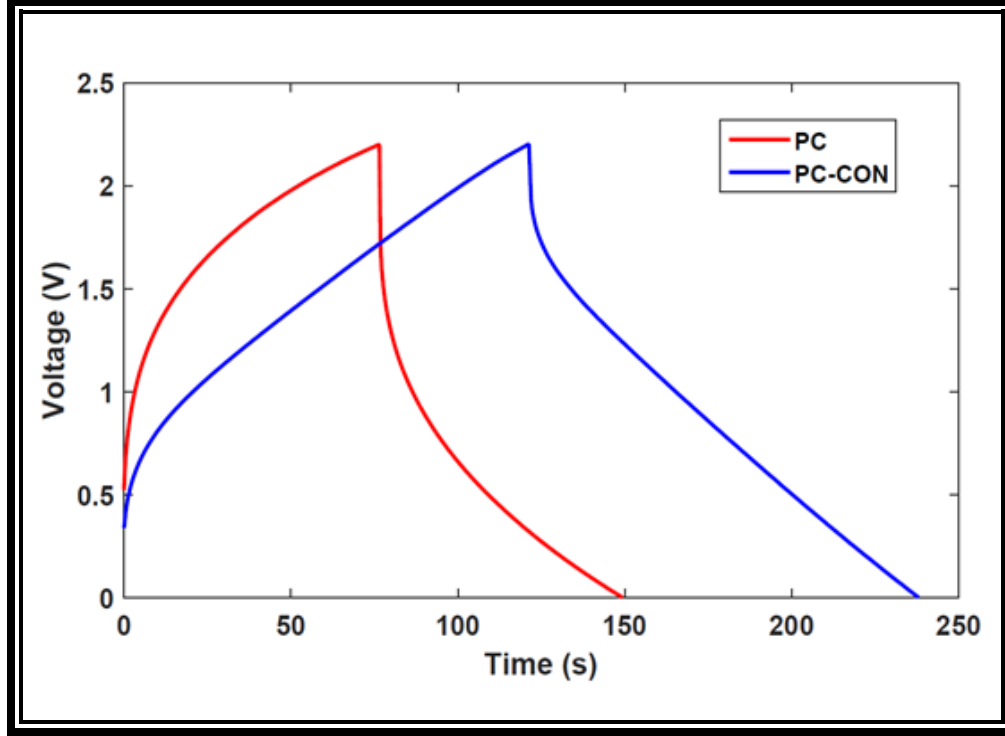


Figure 3.19: Galvanostatic charge/discharge curves of PC and PC-CON at a current density of 0.5 A/g.

Figure 3.20 shows the voltage-time profile of PC-CON electrode at different current densities of 0.5 and 1 A/g. As the current density increased, the discharging time becomes less.

### Nanowire Modified Carbon Fibers for Enhanced Electrical Energy Storage

Six cycles of galvanostatic charging-discharging curves for all four samples at 56  $\mu$ A are shown in figure 3.21 (e-h) within the potential window of 0-0.5 V. Capacitance for the four fiber super-capacitors or nanowire hybrid fiber super-capacitors originates either at the electrolyte/fiber interface or electrolyte/nanowire interface which is indicated by the typical triangular nature of the curves. The charging-discharging curves for all four samples showed very symmetric nature indicating good electrochemical capacitive property and high reversibility, consistent with earlier CV observation. Specific capacitance for the super-capacitors can be calculated by the following equation [93],

$$C_s = \frac{4I \Delta t}{m \Delta V} \quad (1)$$

where  $I$  is the discharging current,  $t$  is the discharging time,  $V$  is the discharging voltage, and  $m$  is the mass of active material in the electrodes.

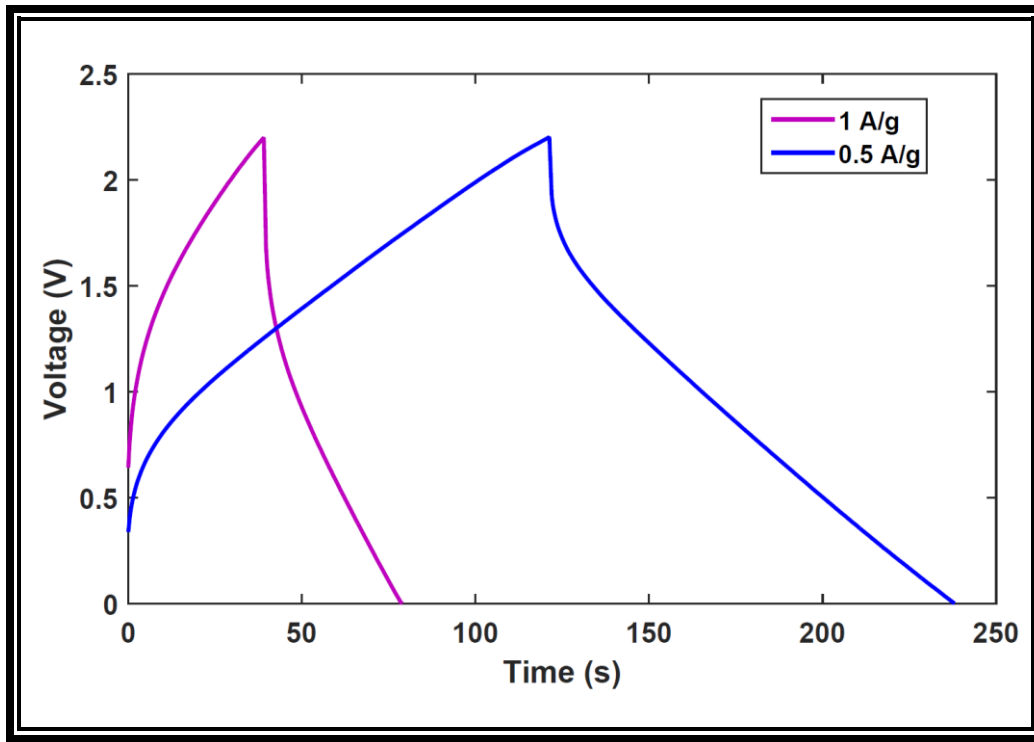


Figure 3.20: Galvanostatic charge/discharge curves of PC-CON at different current densities.

Specific capacitance for the samples was calculated from the discharge slope of the galvanostatic charge discharge curve [40]. Carbon fiber coated with Au (CF-Au) has a specific capacitance value of 2.35 F/g which is about 7% higher than that of bare carbon fiber (CF) (2.2 F/g). ZnO NWs on carbon fiber could provide more surface area for the pseudo-capacitance of the electrodes, therefore, provided 16% higher specific capacitance (2.55 F/g) than CF. Highest specific capacitance value was obtained from ZnO NWs on carbon fiber coated with gold which showed about 65.9% higher value (3.65 F/g) than CF. We also measured specific capacitance in flexible/twisted condition for all the samples but no apparent change was observed which confirms highly flexible nature of the electrodes. To improve the value of the specific capacitance of the

electrochemical capacitor further optimization might be done, i.e., matching the pore sizes and ion size of the electrolyte, controlling the density of ZnO NWs..

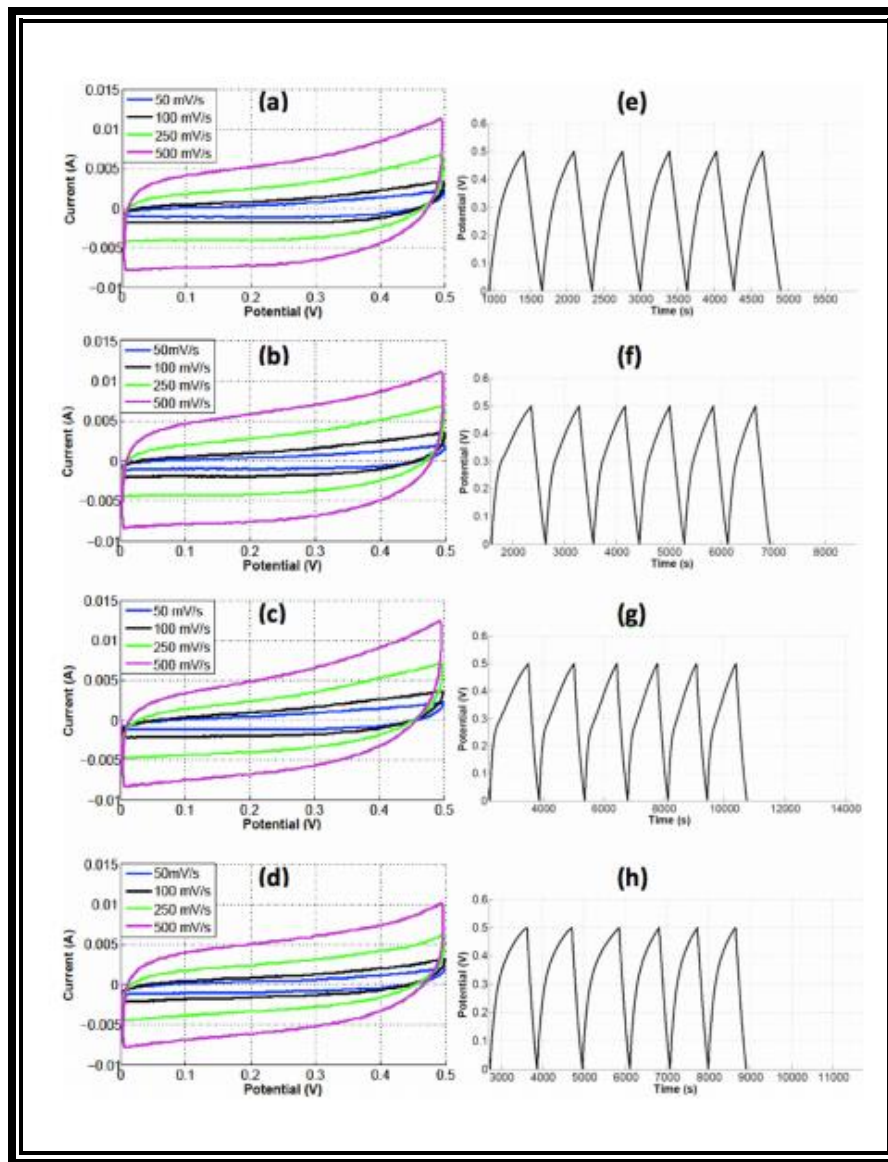


Figure 3.21: Typical cyclic voltammograms of (a) CF (b) CF-Au (c) CF-ZnO (d) CF-ZnO-Au electrode super-capacitor & galvanostatic charge discharge curve at  $56 \mu\text{A}$  within a voltage window of 0-0.5 V for (e) CF (f) CF-Au (g) CF-ZnO (h) CF-ZnO-Au electrode super-capacitor.

### 3.2.3 Electrochemical Impedance Spectroscopy

Electrochemical Impedance Spectroscopy (EIS) was also conducted to understand the transport characteristics of the charge carriers within the electrode. This electrochemical technique can take measurements under steady-state conditions that allow acquisition time high enough to get accurate measurements and can be carried out by controlling either the current or the voltage which enables to measure either current or voltage. Figure xx shows the signal type used for EIS. Voltage ( $V_s$ ) is set at required point and a small amplitude of sinusoidal signal is overlaid and carried out at several frequencies ( $f, Hz$ ),  $\partial v$ , and  $\partial i$  are the amplitudes of the voltage and the current respectively.

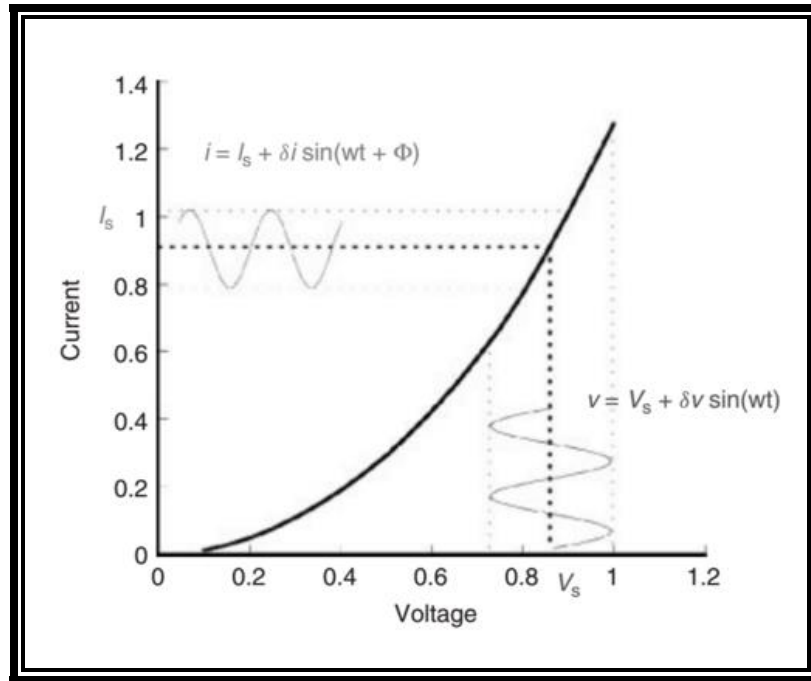


Figure 3.22: Stationary polarization curve (black bold line). A sinusoidal voltage is imposed over the steady state voltage and the resulting current is measured. A measurement is made at different frequency ( $f = \frac{\omega}{2\pi}$ ) [21].

Stationary conditions ( $\frac{\partial i}{\partial t} \rightarrow 0$ ) should be reached before launching the experiment to get highly reliable measurements). While the signal is small, there exist a linear relation between the current and the voltage at each frequency pulsation:

$$V = Zi(V)$$

where,  $V$  is the voltage,  $i$  is the current,  $Z$  is the impedance.

In complex notation,  $V$  and  $i$  can be expressed as:

$$V(\omega) = \delta v \exp(j\omega t)(V)$$

$$i(\omega) = \delta i \exp[j(\omega t + \Phi)](A)$$

Therefore, previous equation can be written as follows:

$$Z(\omega) = \frac{\delta v}{\delta i} \exp(-j\Phi)(\Omega)$$

where,  $Z(\omega)$  is the complex impedance and the impedance can also be expressed as

$$Z(\omega) = Z_{Re} + j Z_{Im}(\Omega)$$

with the impedance modulus as

$$\Phi = \arctan(Z_{Im}/Z_{Re})$$

where,  $Z_{Re}$  and  $Z_{Im}$  are the real and imaginary parts of  $Z(\omega)$ .

A complex electrochemical system can be simplified using this technique. Equivalent circuit can be formed using this technique which helps to study electrochemical cell. Moreover, along with understanding the physical analysis and behavior of a system, EIS also brings clues to understand the reaction kinetics [21].

The impedance spectra in Figure 3.23, which represents the EIS for PC-CON sample, exhibits an arc in the high frequency (up to 1 MHz) region and a sloped line in the low frequency (up to 20 Hz) region. This EIS pattern can be fitted by an equivalent circuit shown in Figure 3.24. The equivalent circuit consists of bulk solution resistance  $R_s$ , the charge transfer resistance  $R_{ct}$ , the Warburg resistance ( $W$ ) related to the diffusion of ions and the constant phase element (CPE) to account for the double layer capacitance. The semicircle pattern for the PC-CON sample confirms the existence of pseudo-capacitive interactions and the vertical shape at the low frequency region

indicates a pure capacitive behavior. Moreover,  $R_s$  and  $R_{ct}$  can be obtained from the Nyquist plot, where the semicircle intercepts the real axis at  $R_s$  and  $R_s+R_{ct}$ , respectively. The results clearly demonstrate that the  $\text{CeO}_2$  nanoparticles improve the conductivity of the electrode, facilitating the charge-transfer of the composites.

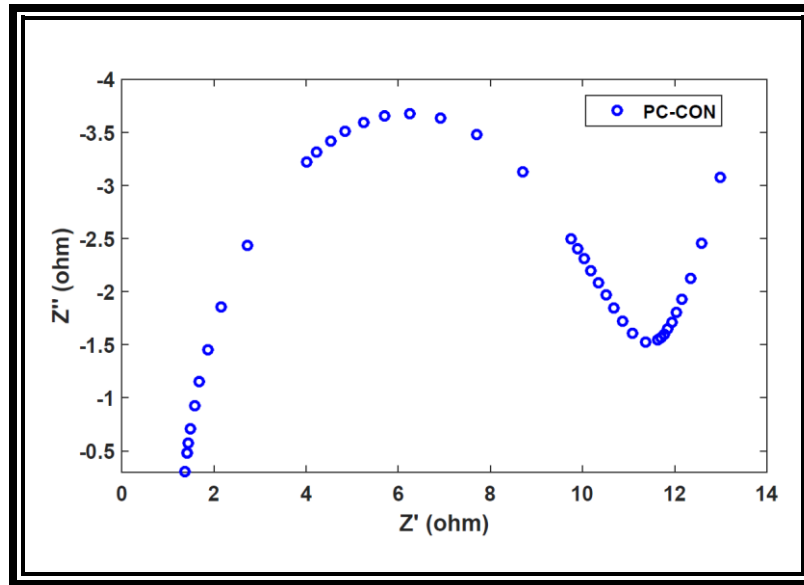


Figure 3.23: Nyquist plot for PC-CON sample.

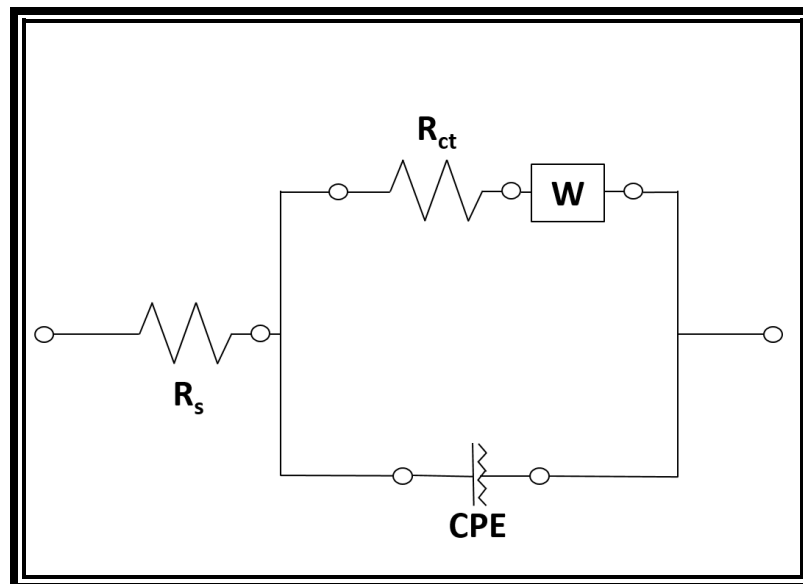


Figure 3.24: PC-CON equivalent circuit of EIS.

The impedance spectra in Figure 3.25, which represents the EIS for PC sample, exhibits an arc shape throughout frequency region. For the porous carbon sample, both bulk solution resistance and charge transfer resistance values are higher than PC-CON sample. Comparing the two nyquist plot, it is clear that the CeO<sub>2</sub> nanoparticles improve the conductivity of the electrode, facilitating the charge-transfer of the composites.

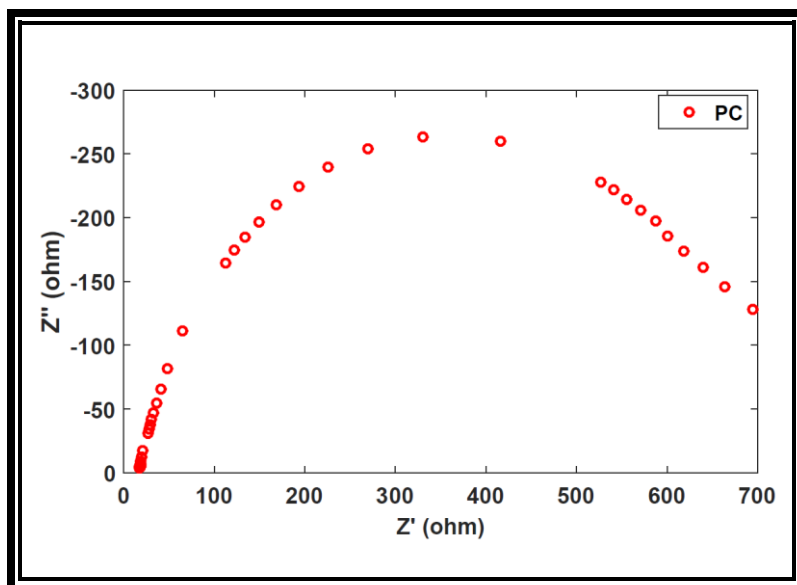


Figure 3.25: Nyquist plot for PC-CON sample.



## **Chapter 4: Lithium Ion Battery**

This chapter is intended to describe all the characterization procedures which were performed to determine the morphology, crystal information, and gravimetric analysis of the samples after the chemical synthesis for the electrode materials of LIBs. Scanning Electron Microscopy (SEM) and Transmission Electron Microscopy (TEM) were performed to see the morphology and acquire information regarding the particle sizes of the sample. X-ray Diffraction was also performed to determine the crystal structure of the sample. Later, Fourier Transformation Infrared Spectroscopy (FTIR) was also carried out to know regarding the functional groups present in the sample.

The next portion of this chapter discusses the principles of the electrochemical testing procedures. 8-channel battery analyzer from MTI Corp. was used for evaluating the LIB performance. Later, all results from these testing are presented and discussed to for understanding the electrochemical kinetics of the LIBs.

### **4.1 Characterization**

#### **4.1.1 Scanning Electron Microscopy (SEM)**

##### **Microwave Exfoliated Graphene Oxide/TiO<sub>2</sub> Nanowire Hybrid for High Performance Lithium Ion Battery**

Hitachi S-4800 Scanning Electron Microscope used to characterize the samples. The surface morphology of the MEGO is shown in Figure 3(a) and the surface topography is curvy and rough, indicating high surface area of the MEGO. As indicated by Figure 3 (c) and (d), TiO<sub>2</sub> nanowires are uniformly grown on MEGO with an average diameter of 200 nm and length of 3  $\mu$ m. Because of the wavy nature of MEGO, TiO<sub>2</sub> nanowires growth followed its surface topography, indicating the MEGO morphology was maintained after the nanowire growth. Figure 3(b) shows the morphology of the pristine PC (CAS No 7440-44-0) purchased from ACS Material.

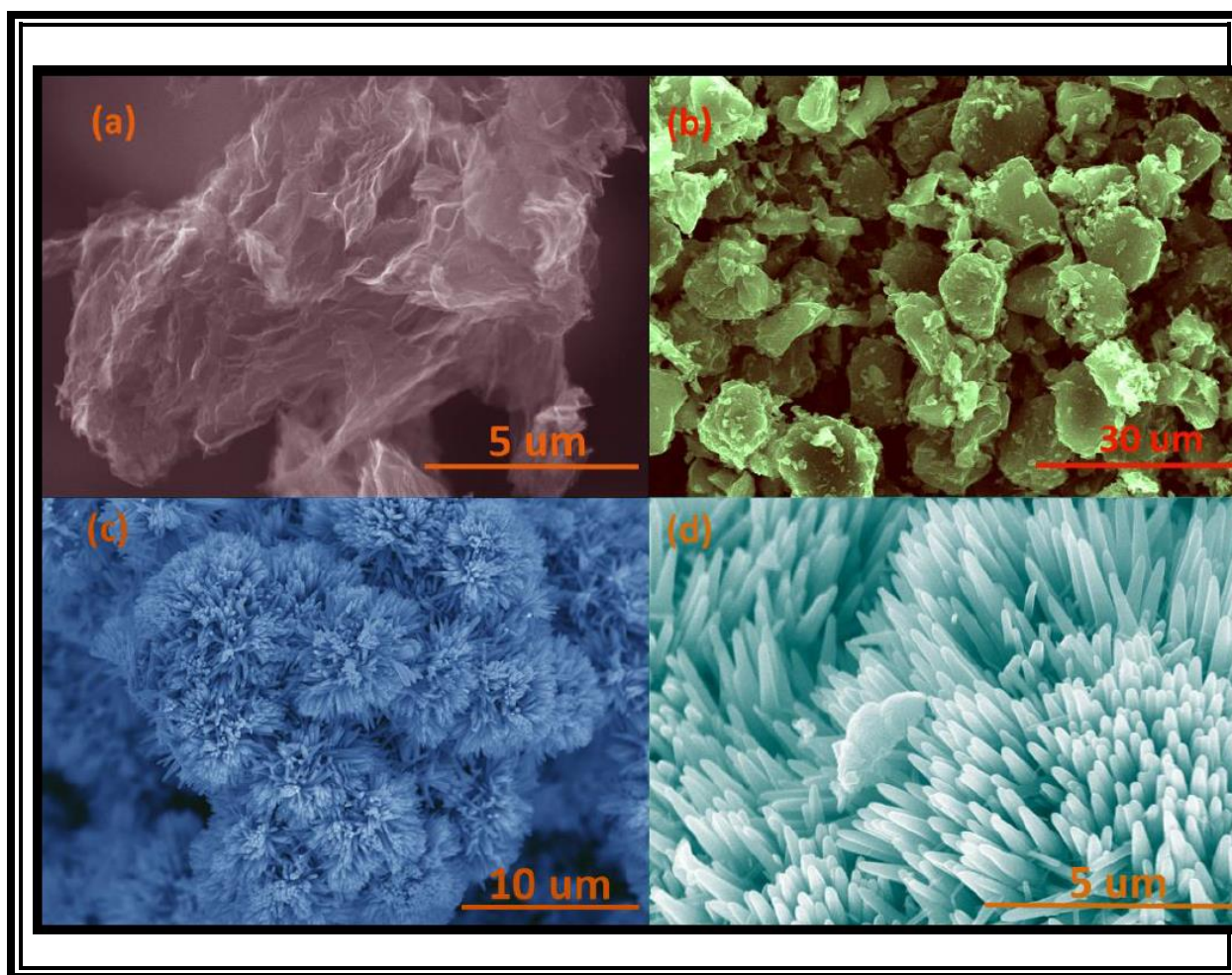


Figure 4.1: SEM image of (a) MEGO, (b) PC, (c-d) MEGO-TON hybrid.

### Investigation of modified graphene for energy storage applications

The surface morphology of GA and GA with ZnO nanowire is shown in Figure 4. Wrinkled topography of GA with high surface area can be understood from the low and high magnification images (Figure 4.2 (a-b)). The pore size of the thermally reduced virgin GA is approximately 5~20  $\mu\text{m}$ , as estimated from the images. Note that all of the GA samples shown in Figure 4 were freeze-dried from GO aqueous solution with a concentration of 30 mg/mL. The single layer nature of the synthesized graphene was demonstrated previously thus will not be discussed here [94]. As indicated by Figure 4.2 (c) and (d), ZnO nanowires are grown uniformly throughout the GA with an average diameter of 30nm and length of 1  $\mu\text{m}$ . Because of the wavy nature of GA, ZnO nanowires growth followed its surface topography, indicating the aerogel morphology was

maintained after the nanowire growth. This is also validated by the evidence that the shape and volume of GAs before and after nanowire growth did not change.

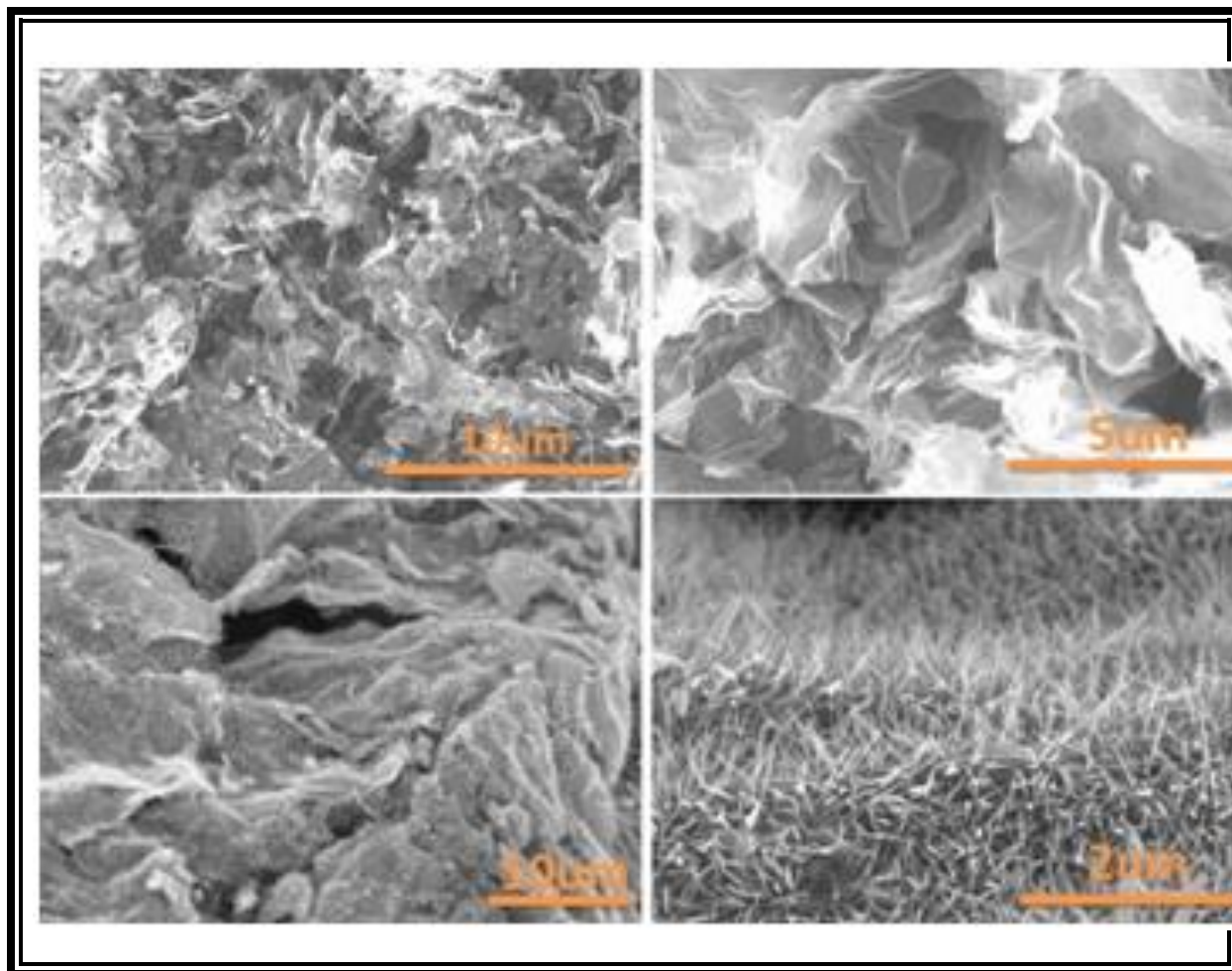


Figure 4.2: SEM images (a-b) Graphene Aerogel, (c-d) Graphene Aerogel with ZnO nanowire.

#### 4.1.2 X-ray Diffraction (XRD)

##### Microwave Exfoliated Graphene Oxide/TiO<sub>2</sub> Nanowire Hybrid for High Performance Lithium Ion Battery

XRD analysis on the MEGO-TON hybrid utilizing a XRD (B8 Discover, Bruker) is shown in Figure 4. All the peaks matched with the standard diffraction data of rutile TiO<sub>2</sub> (PDF file #01-086-0147,  $P4_2/mnm$ ,  $a = b = 4.594 \text{ \AA}$  and  $c = 2.958 \text{ \AA}$ ). XRD patterns exhibited strong diffraction

peaks at  $27^\circ$ ,  $36^\circ$  and  $55^\circ$  indicating  $\text{TiO}_2$  in the rutile phase. No extra peaks corresponding to any other secondary phases were observed [85].

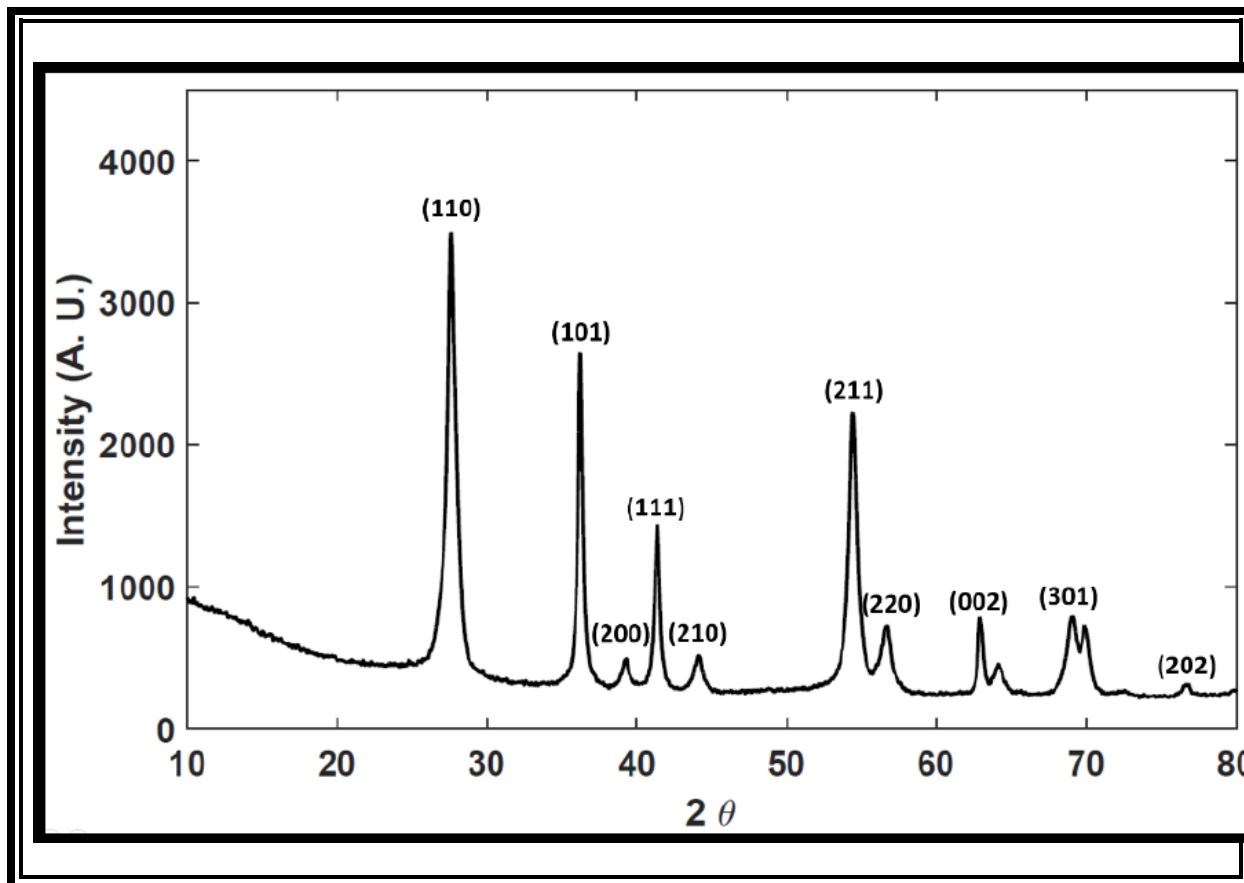


Figure 4.3: XRD result for MEGO-TON hybrid.

### Investigation of modified graphene for energy storage applications

XRD patterns were obtained to confirm the crystal structures of GA and nanowires. After the freeze drying process, graphene oxide contains water molecules along with some surface functional groups ( $-\text{OH}$ ,  $-\text{COOH}$  etc.) [95]. During reduction of graphene oxide, it loses water molecules upon heating to  $200^\circ\text{C}$  and gets fully rid of the functional group by heating up to  $1000^\circ\text{C}$ . As graphene has 2D crystal structure, there should not be any XRD peak for graphene. However, during the freeze drying and thermal reduction process, the exfoliated GO sheets are

thermodynamically instable; they tend to stack with each other for a more stable state. The peak of GA at around 23 degrees showed the evidence of this stacking phenomenon.

Unlike the thermally reduced graphene sample reported elsewhere, the 2-theta peak of graphene typically has value of 26 degree; the 2-theta peak of the GA studied here is around 22 degrees, indicating a large space in between the sheets. This is because the graphene is synthesized from freeze-drying, where the morphology and spacing between graphene sheets are maintained after thermal reducing. Typically, graphene is reduced from graphene oxide powder, where the graphene is free to stacking back to each other after the water vapor and surface functional groups are removed. The enhanced spacing between graphene sheets could benefit the lithium ion diffusion, leading to better charge and discharge capability in LIB. Note the GA/ZnO also showed peaks belong to, all peaks match the standard card of these materials and no peaks from impurity phase were shown.

#### **4.1.3 Fourier Transformation Infrared Spectroscopy (FTIR)**

Fourier transform infrared (FTIR) spectra were obtained by using a Perkin-Elmer, Spectrum 100, Universal ATR Sampling Accessory with the range of 650–3650  $\text{cm}^{-1}$  in transmittance mode. Figure 5 shows the neat FTIR spectra of GO and MEGO. The FTIR of GO shows the presence of C=O stretching at 1728  $\text{cm}^{-1}$ , graphene sheet aromatic C=C stretching at 1622  $\text{cm}^{-1}$ , broad O–H stretching at 3400  $\text{cm}^{-1}$ , C–OH bending at 1368  $\text{cm}^{-1}$ , C–O stretching at 1045  $\text{cm}^{-1}$ , and C–OH stretching at 1222  $\text{cm}^{-1}$ . The FTIR spectrum of GO revealed the presence of oxygen containing functional groups in it such as –COOH, –OH, epoxide and alcoxide.

On the other hand, the FTIR spectrum of MEGO shows the presence of C=O stretching at 1734  $\text{cm}^{-1}$ , graphene sheet aromatic C=C stretching at 1628  $\text{cm}^{-1}$  which may have overlapped with other absorptions leading to a slightly broader absorption centered at 1576  $\text{cm}^{-1}$ . Moreover, the presence of absorption band ranging from 950 to 1350  $\text{cm}^{-1}$  is due to the presence of epoxy and alcoxy groups in the MEGO. Usually, the epoxy and alcoxy stretching absorption (C–O) are seen at 1288 and 1076  $\text{cm}^{-1}$  respectively. All of these absorption bands of PRGO IR spectra indicate

the presence of very low amount of oxygen containing functional groups in it compared to the GO sample. The absence of O-H stretching  $3400\text{cm}^{-1}$ , C-OH bending at  $1368\text{ cm}^{-1}$ , C-O stretching at  $1045\text{cm}^{-1}$  and C-OH stretching at  $1222\text{ cm}^{-1}$  all indicates that the MEGO contains no or very low  $-\text{COOH}$  and  $-\text{OH}$  functional groups [96].

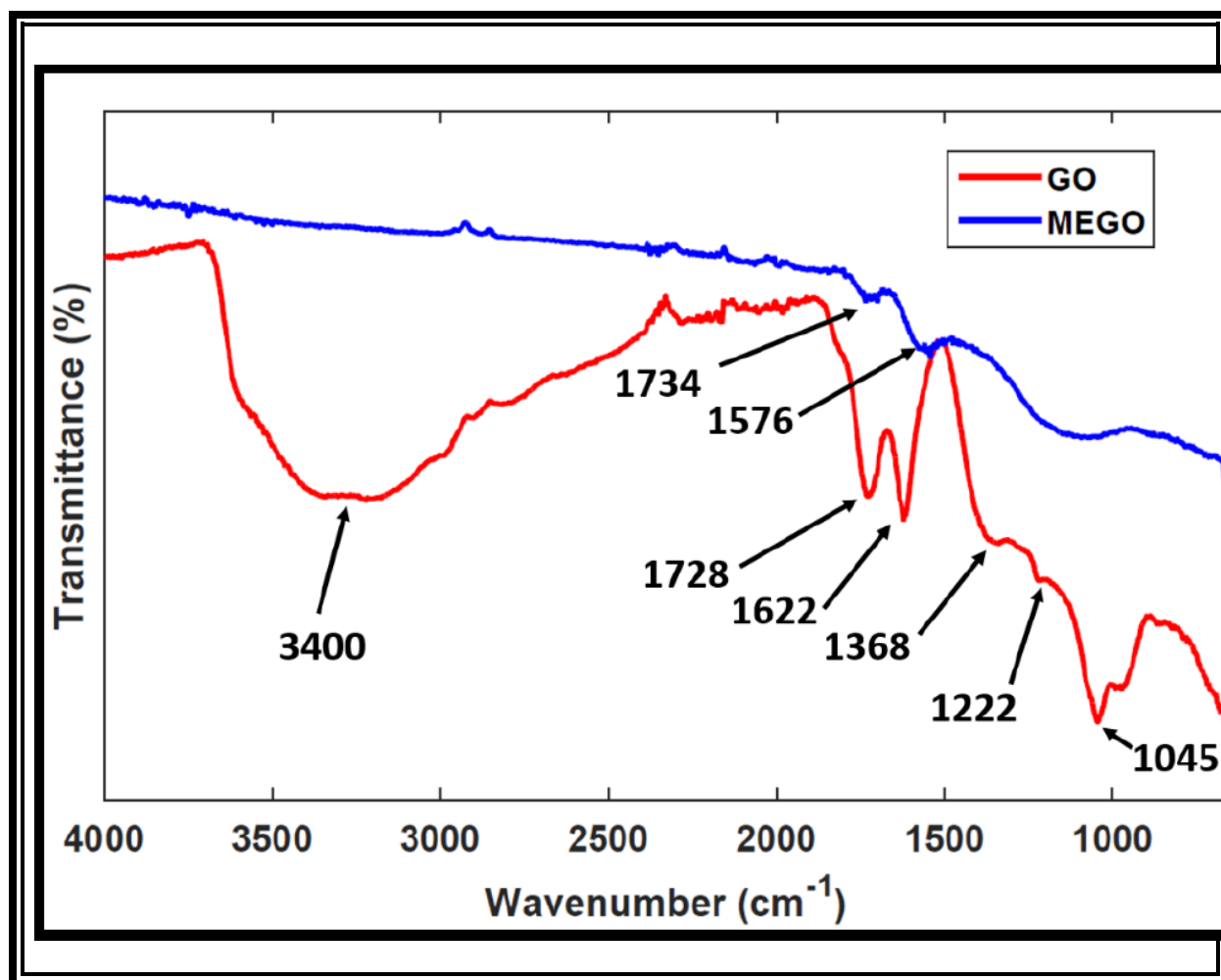


Figure 4.4: FTIR spectra of GO and MEGO.



## 4.2 Testing and Discussion

A eight-channel battery analyzer from MTI Corp. was used to analyze small coin cell from 6.0 mA to 3000 mA, up to 5V. Cylindrical cells can also be analyzed using this testing facility. Each channel of the analyzer has independent constant-current and constant-voltage source, which can be programmed and controlled by computer software. This system provides most applications in battery testing fields such as electrode materials research, battery performance test, small-scale battery formation, capability grading, battery pack testing.

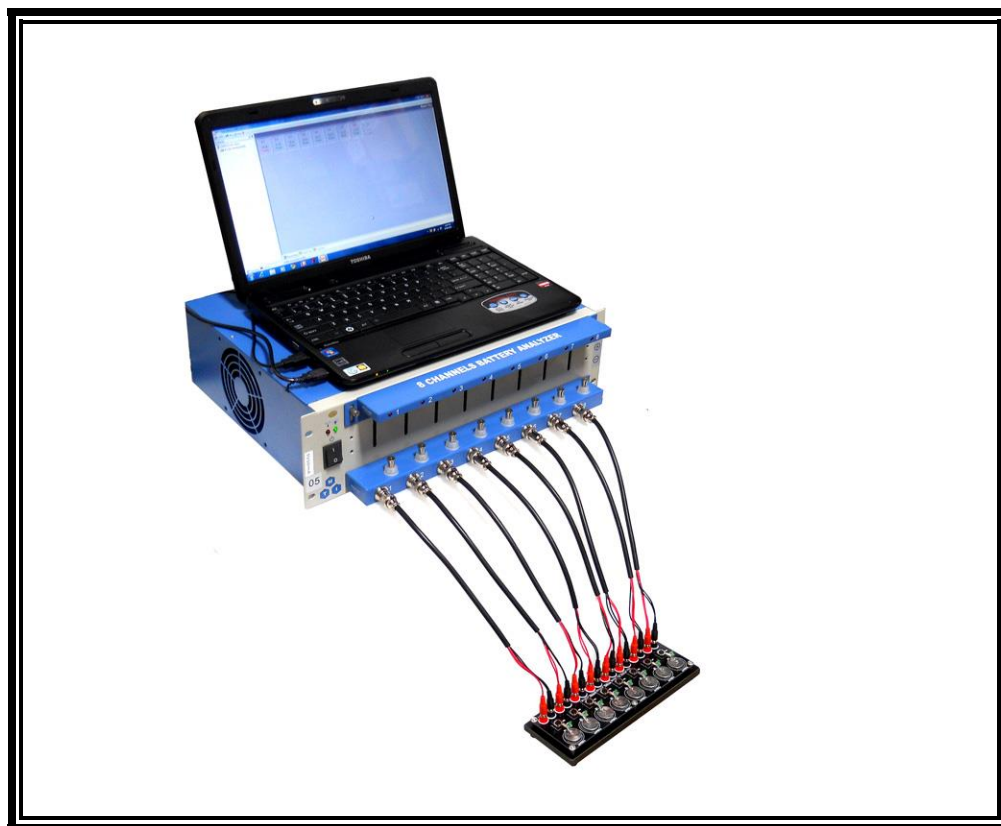


Figure 4.5: MTI 8-channel battery analyzer.

### 4.2.1 Microwave Exfoliated Graphene Oxide/TiO<sub>2</sub> Nanowire Hybrid for High Performance Lithium Ion Battery

To evaluate the electrochemical performance of the electrodes, we investigated the Li-ion insertion/extraction properties in PC and MEGO-TiO<sub>2</sub> hybrid materials using MTI eight-channel

battery analyzer. Figure 4.5 (a) shows the galvanostatic charge-discharge curves for PC electrode within the voltage window 0.01 to 2 V in the 1<sup>st</sup>, 2<sup>nd</sup>, 25<sup>th</sup>, and 40<sup>th</sup> cycles; Figure 4.5 (b) shows the similar curves for MEGO-TiO<sub>2</sub> hybrid electrode within the same voltage window in the 1<sup>st</sup>, 2<sup>nd</sup>, 25<sup>th</sup>, and 40<sup>th</sup> cycles. The current density for both electrodes was maintained at 100mA/g, 200mA/g, 300mA/g, and 500 mA/g respectively for 40 cycles. The current density was shifted for every 5 cycles. Note that no obvious voltage plateau was observed for both cases. The significantly high value of capacity in the first discharge is caused largely by the decomposition of the non-aqueous electrolyte and the formation of solid electrolyte interface (SEI) layer on the electro-active materials. This would also likely to protect the electrodes partly and improve the stability of cyclic performance [97, 98]. Figure 4.5 (c) shows the cyclic performance for PC and MEGO-TON hybrid electrode. As mentioned before, the cycling stability of PC and MEGO-TON hybrid electrodes were measured at varied current density within the range of 100-500 mA/g for 40 cycles. For both sample, the specific capacity decreased with the increase of current density. With the increase in cycle numbers lithium storage performance of PC electrode drops. After 11<sup>th</sup> cycle, specific capacity for PC anode was 78 mAh/g then reduced to 72 mAh/g after 35<sup>th</sup> cycle at the same current density (300 mA/g). On the contrary, the specific capacity of MEGO-TON anode was 109 mAh/g then became 111 mAh/g after 35<sup>th</sup> cycle at similar current density. For the first 20 cycles at current density 100, 200, 300, and 500 mAh/g the specific capacity of MEGO-TON sample was respectively 38%, 38%, 39%, and 56% higher than PC anode. For the next 20 cycles, the specific capacity for MEGO-TON sample was respectively 17%, 40%, 55%, and 80% higher than PC sample at similar order of current density. Note that, with the percentage increment of specific capacity for MEGO-TON sample becomes more at higher current density. This increment is due to the TiO<sub>2</sub> nanowires, because all other testing parameters for both batteries are same and same testing parameter is used. It can be explained that charge-discharge cycles create more space to facilitate Li-ion diffusion, augmenting the specific capacity for MEGO-TON anode as the cycle number increases. Lower capacity in the beginning resulted from the incomplete reaction and irreversible lithium loss due to the formation of solid electrolyte interface.



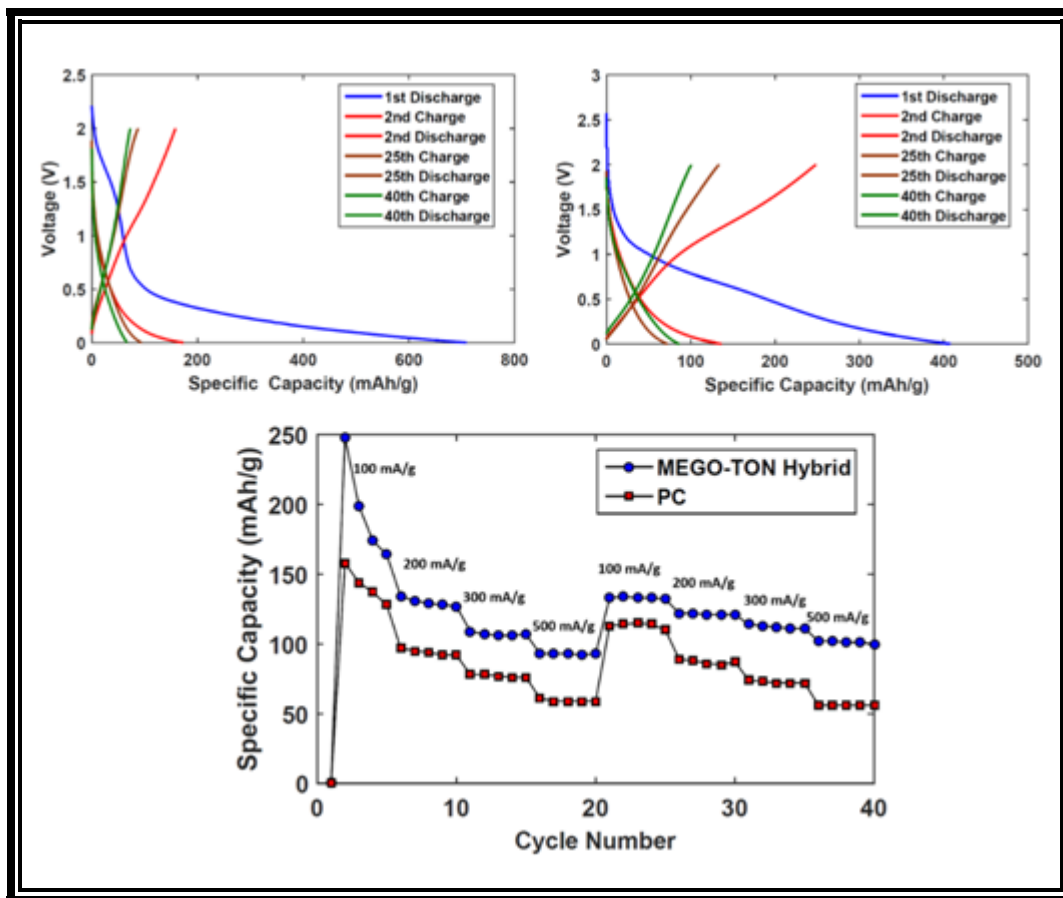


Figure 4.6: Measurements of capacity and rate capability, (a) charge/discharge curve for PC electrode, (b) charge/discharge curve for MEGO-TON hybrid electrode, (c) comparison of specific capacity of the two anode materials as a function of cycle number: PC and MEGO-TON anode were cycled at 100mA/g, 200mA/g, 300mA/g, and 500 mA/g current density respectively for 40 cycles.

Previously, it was shown that graphene electrode has lower performance than graphene/metal oxide nanowire hybrid electrode because metal oxide nanowires prevent the graphene sheets from agglomerating, preserving high surface area which is favorable for Li-ion storage [5]. Though the PC's porous structure helps for high rate performance by facilitating ion transport, it can be anticipated from the electrochemical results of MEGO-TON hybrid sample that the  $\text{TiO}_2$  nanowires provide better elastic buffer space for Li-ion during intercalation/deintercalation, which prevents cracking or crumbling of the electrodes retaining the

original properties. Moreover, graphene has high electrical conductivity which benefits the MEGO-TON hybrid electrode in achieving low resistance and electronic/ionic conductivity, therefore leading to a higher specific capacity. Finally, MEGO-TON hybrid electrode provides large electrode/electrolyte contact area and short path length for Li-ion diffusion with good stability, thus further facilitates the Li-ion transport. All above-mentioned reasons are expected to be responsible for the improved anodes with excellent energy storage capacity, cycling stability, and Coulombic efficiency.

#### **4.2.2 Porous carbon/CeO<sub>2</sub> composites for Li-ion battery application**

To evaluate the electrochemical performance of the anodes an eight-channel battery analyzer from MTI Corporation was used. Figure 4.6 (a) and (b) shows the galvanostatic charge-discharge curves for PC and PC/CON anodes respectively at the voltage window between 0.01 to 2 V in the 1st, 2nd, 10th and 30th cycles. The significantly high value of capacity in the first discharge is caused largely by the decomposition of the non-aqueous electrolyte and the formation of solid electrolyte interface (SEI) layer on the electroactive materials [97]. This is also would likely to protect the electrodes partly and improve the stability of cyclic performance [97, 99]. The current density used for the PC electrodes is 100 mA/g while for PC/CON electrode it was varied from 100mA/g, 200 mA/g, 300 mA/g and 500mA/g in a cyclic manner. It can be seen that while the electrode with only PC shows a capacity of 64 mAh/g at the 30th cycle, the PC/CON electrode retained capacity around 100 mAh/g after that cycle. Fig. 18 (c) compares the specific capacity of the PC and PC/CON electrodes as a function of cycle number from 2nd cycle to the 40th cycle at different current densities. The capacity of PC electrode decreased from 164 mAh/g to 77 mAh/g while PC/CON showed a higher capacity of 195 mAh/g in the 2<sup>nd</sup> cycle and it went down to 146 mAh/g and then successively to 90 mAh/g with further increase in current densities. However, when the current density was returned to the 100 mA/g the electrode recovered to 113 mAh/g capacity. After the 40th cycle, PC/CON electrode showed significantly higher capacity (104

mAh/g) over the PC electrode (77 mAh/g) although it was measured at five times higher current density (500 mA/g).

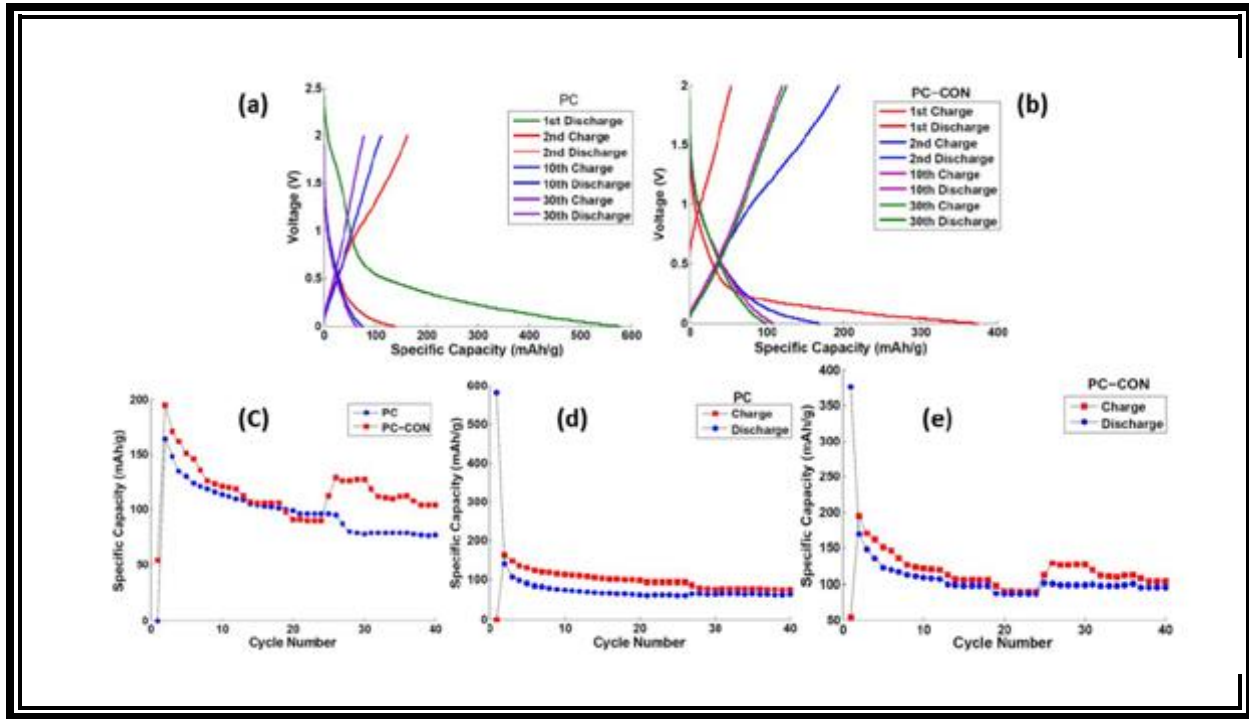


Figure 4.7: Measurements of capacity and rate capability, (a) charge/discharge curve for PC anode, (b) charge/discharge curve for PC-CON anode, (c) comparison of specific capacity of the two anode materials as a function of cycle number: PC anode was cycled at 100 for 40 cycles; PC-CON was varied among 100mA/g, 200mA/g, 300mA/g and 500mA/g consecutively after every 5 cycles (d) cycling performance of PC anode at 100mA/g for 40 cycles (e) specific capacity of PC-CON at 100mA/g, 200mA/g, 300mA/g and 500mA/g consecutively after every 5 cycles.

#### 4.2.3 Investigation of modified graphene for energy storage applications

Two types of LIBs were prepared with GA and GA with ZnO nanowires as working electrode respectively. To evaluate the electrochemical performance of the anodes, an 8 channel battery analyzer from MTI Corporation was used. Figure 4.7 shows galvanostatic charge discharge curves for the two kinds of working electrode and cycle performance comparison between the two kinds of anodes. For both cases  $\text{LiCoO}_2$  cathode was used as counter electrode. Figure 4.7 (a) and (b) show galvanostatic charge-discharge curves for GA and GA with ZnO nanowire anodes

respectively at current density 100 mA/g and voltage window between 0.01 to 3.7 volts in the 1<sup>st</sup>, 5<sup>th</sup>, 10<sup>th</sup> and 20<sup>th</sup> cycles. Note that no obvious voltage plateau was observed for both cases. The 1<sup>st</sup> charge capacity of graphene anode (690 mAh/g) is way higher than that of GA/ZnO NW anode (249 mAh/g) and same trend was found in discharge capacity. With the increase of cycle numbers lithium storage performance of GA anode drops. Coulombic efficiency of GA/ZnO NW electrode was always found above 98% and its lithium storage performance increased with the increase of cycles. The 20<sup>th</sup> discharge-charge capacities are 245 and 240 mAh/g for GA, 298 and 295 mAh/g for GA/ZnO NW electrode. The GA anode loses its reversibility where the GA/ZnO NW anode gains reversibility with cycle numbers. More importantly, the GA/ZnO NW anode exhibits a much better cycling performance than the GA anode (Figure 4.7c). It can be seen that the reversible capacity of GA decreases from 690 to 245 mAh/g up to 20 cycles. On the contrary, capacity of GA/ZnO NW electrode was around 249 mAh/g after 1<sup>st</sup> cycle which slightly falls after that and then it gradually increases and goes above the GA anode's capacity with time. Obviously, this is due to the ZnO nanowires since all other assembling parameters for both the batteries were same and same testing parameter is used. It can be explained this way that charge discharge cycles create more space for better Li-ion diffusion augmenting the specific capacitance in GA/ZnO NW as the cycle number increases. Therefore, there is an excellent synergistic effect between ZnO nanowires and graphene aerogel in the anode which becomes more acute with cycles and performs a vital play in the excellent cycling performance of GA/ZnO NW anode. Lower capacity in the beginning was resulted from the incomplete reaction and irreversible lithium loss because of the formation of solid electrolyte interface (SEI) layer.

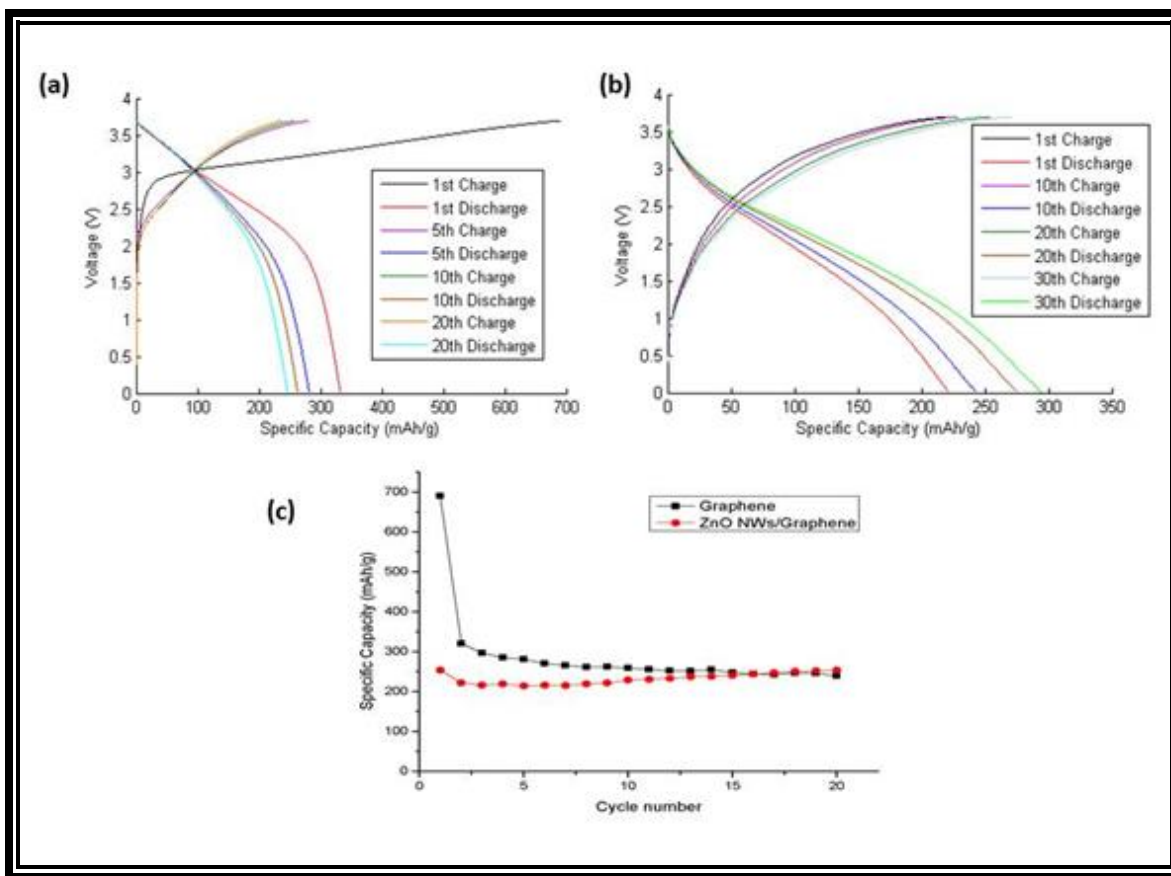


Figure 4.8: Measurements of capacity and rate capability. (a) charge/discharge curve for GA anodes (b) charge/discharge curve for GA with ZnO nanowires anode (c) comparison of specific capacity of the two anode materials as a function of cycle number.

The obtained result indicates that aligned ZnO nanowires on graphene aerogel provide better properties, i.e., capacity, Coulombic efficiency, rate capability and cycling stability for LIB than GA. Reasons for the improved performance of the developed GA/ZnO NW anode material can be a few. Firstly, aligned nanowires between graphene sheets prevent the graphene sheets from agglomerating, preserving high surface area which is favorable for Li-ion storage. Secondly, graphene has good electrical conductivity which benefits the anode in achieving low resistance and electronic/ionic conductivity, therefore leading to a higher specific capacity [9, 100]. Thirdly, GA/ZnO nanowires provide elastic buffer space for Li-ion during intercalation/de-intercalation which prevents cracking or crumbling of the anodes retaining the original properties. Finally,

GA/ZnO NW anode provides large electrode/electrolyte contact area and short path length for Li-ion diffusion with good stability, thus maximize the Li-ion transport. The above mentioned reasons are expected to be responsible for the improved anodes with excellent energy storage capacity, cycling stability and Coulombic efficiency.

## Chapter 5: Conclusion

This chapter summarizes all the works on the electrochemical devices, i.e. super-capacitors and lithium ion batteries. It states the present research problem for the development of electrode devices for these devices and solutions stated in this research. The characterization and testing techniques are also mentioned in this section. At last, the research outcome was stated.

The following content in this chapter contains material from published journal articles made with the help of the author in collaboration with his colleges. The following articles are: *Investigation of modified graphene for energy storage applications* [5], *Nanowire modified carbon fibers for enhanced electrical energy storage*[17], *High-performance porous carbon/CeO<sub>2</sub> nanoparticles hybrid super-capacitors for energy storage* [101], *Porous carbon/CeO<sub>2</sub> composites for Li-ion battery application* [7], and *Microwave Exfoliated Graphene Oxide/TiO<sub>2</sub> Nanowire Hybrid for High Performance Lithium Ion Battery*[102].

### 5.1 Super-capacitor

#### 5.1.1 High-performance Porous Carbon/CeO<sub>2</sub> Nanoparticles Hybrid Super-capacitors for Energy Storage

Energy storage/harvesting research is indispensable in today's research world which faces challenges such as environmental problems and the depletion of fossil fuels. Thus there is a need for better energy systems with enhanced performance from current available technology. Super capacitors which use hybrid carbon-metal oxide electrodes may provide a solution which results in enhanced energy and power density, cyclic stability and life. Here, a method has been presented which uses a simple one-step low temperature hydrothermal process to fabricate PC-CON electrodes. This hybrid electrode combination allows for the hybridization of the best attributes of each singular electrode material. SEM, TEM and HRTEM images confirmed the formation of crystalline nanoparticles in the hydrothermal reaction. Only porous carbon and CeO<sub>2</sub> were found in the XRD analysis. Based on the electrochemical results, it seems that PC-CON hybrid

electrodes have promising future for electrochemical energy storage with up to 500% of specific capacitance enhancement. This simple method can be utilized for making high performance super-capacitor for next generation aerospace, automobile and electronic applications.

### **5.1.2 Nanowire Modified Carbon Fibers for Enhanced Electrical Energy Storage**

Multifunctional structural energy storage devices are one of the key research interests of recent time to obtain load bearing and energy storage capability in one structure. It has been demonstrated nanowire carbon fiber hybrid could provide better mechanical strength than bare carbon fiber for composites. In this pilot research project, we have incorporated the same nanowire hybrid carbon fiber for electrode materials to examine its electrochemical properties for potential structural energy applications. A low temperature hydrothermal method has been utilized to synthesize ZnO nanowires on carbon fiber cloth and sputtered for high performance super-capacitor electrode. SEM images demonstrated good coverage of uniformly distributed nanowires all over carbon fiber cloth. XRD analysis result confirmed existence of carbon and ZnO only. The growth of nanowires has a positive synergistic effect which helps pathways for better ion diffusion incrementing electrode-electrolyte contact area. Based on the obtained result and previous report, it is obvious that ZnO NWs on carbon fiber has a promising future for structural energy storage with appropriate solid electrolyte. This simple method can be utilized for making high performance structural super-capacitor for next generation aerospace, automobile and electronic application.

## **5.2 Lithium Ion Battery**

### **5.2.1 Microwave Exfoliated Graphene Oxide/TiO<sub>2</sub> Nanowire Hybrid for High Performance Lithium Ion Battery**

Energy storage devices, i.e., battery and super-capacitors, are the bases for green energy solutions. A simple method of graphene oxide exfoliation was utilized through microwave radiation and a low-temperature hydrothermal method was employed to synthesize MEGO-TON hybrid material for high performance LIB electrode. SEM image demonstrated that the porous



structure was obtained after microwave treatment and nanowires are uniformly distributed on the exfoliated graphene oxide surface after thermal reduction. Highest 80% improvement of specific capacity was found from MEGO-TON hybrid electrode compared to the as purchased PC electrode material in terms of capacitance and cycle stability. The growth of nanowires has a positive synergistic effect that prevents graphene agglomeration and provides pathways for Li-ion insertion/extraction increasing electrode-electrolyte contact area. This simple method can be utilized in a larger scale for high-performance LIBs.

### **5.2.2 Porous carbon/CeO<sub>2</sub> composites for Li-ion battery application**

In summary, a single step hydrothermal synthesis technique was utilized to synthesize Ceria nanoparticles on porous carbon to develop a high performance LIB anode material. The growth and presence of Ceria was confirmed using SEM, XRD and TEM. Electrodes with bare PC and PC/CON was prepared and tested using a battery analyzer. The PC/CON electrode showed significantly higher specific capacity and better capacity retention up to forty cycles. The investigation shows the potential of using metal oxide nanoparticles on carbonaceous materials as an intriguing way of improving the performance of Li ion batteries.

### **5.2.3 Investigation of modified graphene for energy storage applications**

In summary, energy storage devices such as battery and super capacitor are receiving increasing attention due to their high specific energy density and fast charge and discharge capability. A low temperature hydrothermal method has been utilized to synthesize GA/ZnO NW for high performance LIB anode while graphene aerogel was synthesized by freeze drying method. SEM image demonstrated that the porous structure was maintained after thermal reduction and nanowires are uniformly distributed on the aerogel surface. XRD analysis showed that the spacing between the graphene sheets is higher than reduced graphene powder due to the morphology of the aerogel. Excellent performance was found from GA/ZnO NW anode compared to GA anode in terms of capacitance and cycle stability. The growth of nanowires has a positive synergistic effect which prevents graphene agglomeration and provides pathways for better Li-ion diffusion

incrementing electrode-electrolyte contact area. This simple method can be utilized commercially for making high performance anodes for LIBs.

## References

1. Liu, M., et al., *Development of MnO<sub>2</sub>/porous carbon microspheres with a partially graphitic structure for high performance supercapacitor electrodes*. Journal of Materials Chemistry A, 2014. **2**(8): p. 2555-2562.
2. Panwar, N., S. Kaushik, and S. Kothari, *Role of renewable energy sources in environmental protection: a review*. Renewable and Sustainable Energy Reviews, 2011. **15**(3): p. 1513-1524.
3. Stigka, E.K., J.A. Paravantis, and G.K. Mihalakakou, *Social acceptance of renewable energy sources: A review of contingent valuation applications*. Renewable and Sustainable Energy Reviews, 2014. **32**: p. 100-106.
4. Twidell, J. and T. Weir, *Renewable energy resources*. 2015: Routledge.
5. Shuvo, M.A.I., et al., *Investigation of modified graphene for energy storage applications*. ACS applied materials & interfaces, 2013. **5**(16): p. 7881-7885.
6. Wang, D., et al., *Self-assembled TiO<sub>2</sub>-graphene hybrid nanostructures for enhanced Li-ion insertion*. ACS nano, 2009. **3**(4): p. 907-914.
7. Karim, H., et al. *Porous carbon/CeO<sub>2</sub> composites for Li-ion battery application*. in *SPIE Smart Structures and Materials+ Nondestructive Evaluation and Health Monitoring*. 2015. International Society for Optics and Photonics.
8. Shuvo, M.A.I., et al. *Nanowire-graphene hybrids for lithium-ion-battery*. in *SPIE Smart Structures and Materials+ Nondestructive Evaluation and Health Monitoring*. 2013. International Society for Optics and Photonics.
9. Wu, Z.-S., et al., *Graphene anchored with Co<sub>3</sub>O<sub>4</sub> nanoparticles as anode of lithium ion batteries with enhanced reversible capacity and cyclic performance*. ACS nano, 2010. **4**(6): p. 3187-3194.
10. Lu, L., et al., *A review on the key issues for lithium-ion battery management in electric vehicles*. Journal of power sources, 2013. **226**: p. 272-288.
11. Rajib, M., et al., *Temperature influence on dielectric energy storage of nanocomposites*. Ceramics International, 2015. **41**(1): p. 1807-1813.
12. Mendoza, M., et al., *Development of lead-free nanowire composites for energy storage applications*. ISRN Nanomaterials, 2012. **2012**.
13. Rajib, M., et al., *Enhanced Energy Storage of Dielectric Nanocomposites at Elevated Temperatures*. International Journal of Applied Ceramic Technology, 2015.
14. Tang, H., Y. Lin, and H.A. Sodano, *Enhanced energy storage in nanocomposite capacitors through aligned PZT nanowires by uniaxial strain assembly*. Advanced Energy Materials, 2012. **2**(4): p. 469-476.
15. Tang, H., et al., *Nanocomposites with increased energy density through high aspect ratio PZT nanowires*. Nanotechnology, 2011. **22**(1): p. 015702.
16. Yang, L., et al., *Hierarchical network architectures of carbon fiber paper supported cobalt oxide nanonet for high-capacity pseudocapacitors*. Nano letters, 2011. **12**(1): p. 321-325.
17. Shuvo, M.A.I., et al., *Nanowire modified carbon fibers for enhanced electrical energy storage*. Journal of Applied Physics, 2013. **114**(10): p. 104306.
18. Shuvo, M.A.I., et al. *Multifunctional composites for energy storage*. in *SPIE Smart Structures and Materials+ Nondestructive Evaluation and Health Monitoring*. 2014. International Society for Optics and Photonics.

19. Wang, Y.G., H.Q. Li, and Y.Y. Xia, *Ordered whiskerlike polyaniline grown on the surface of mesoporous carbon and its electrochemical capacitance performance*. Advanced Materials, 2006. **18**(19): p. 2619-2623.
20. Halper, M.S. and J.C. Ellenbogen, *Supercapacitors: A brief overview*. The MITRE Corporation, McLean, Virginia, USA, 2006: p. 1-34.
21. Lu, M., F. Beguin, and E. Frackowiak, *Supercapacitors: materials, systems and applications*. 2013: John Wiley & Sons.
22. Hu, S., R. Rajamani, and X. Yu, *Flexible solid-state paper based carbon nanotube supercapacitor*. Applied Physics Letters, 2012. **100**(10): p. 104103.
23. Noked, M., et al., *Composite carbon nanotube/carbon electrodes for electrical double-layer super capacitors*. Angew Chem Int Ed Engl, 2012. **51**(7): p. 1568-71.
24. Nishide, H., *Toward flexible batteries*. surfaces, 2008. **4**(10).
25. Armand, M. and J.-M. Tarascon, *Building better batteries*. Nature, 2008. **451**(7179): p. 652-657.
26. Simon, P. and Y. Gogotsi, *Materials for electrochemical capacitors*. Nature materials, 2008. **7**(11): p. 845-854.
27. Conway, B., *Electrochemical supercapacitors: scientific fundamentals and technological applications (POD)*. 1999: Kluwer Academic/plenum. New York.
28. Miller, J.R. and P. Simon, *Electrochemical capacitors for energy management*. Science Magazine, 2008. **321**(5889): p. 651-652.
29. Kötzt, R. and M. Carlen, *Principles and applications of electrochemical capacitors*. Electrochimica Acta, 2000. **45**(15): p. 2483-2498.
30. Burke, A., *R&D considerations for the performance and application of electrochemical capacitors*. Electrochimica Acta, 2007. **53**(3): p. 1083-1091.
31. Hung, K., et al., *Wide-temperature range operation supercapacitors from nanostructured activated carbon fabric*. Journal of Power Sources, 2009. **193**(2): p. 944-949.
32. Winter, M. and R.J. Brodd, *What are batteries, fuel cells, and supercapacitors?* Chemical reviews, 2004. **104**(10): p. 4245.
33. Pech, D., et al., *Ultrahigh-power micrometre-sized supercapacitors based on onion-like carbon*. Nature nanotechnology, 2010. **5**(9): p. 651-654.
34. Bae, J., et al., *Fiber Supercapacitors Made of Nanowire-Fiber Hybrid Structures for Wearable/Flexible Energy Storage*. Angewandte Chemie International Edition, 2011. **50**(7): p. 1683-1687.
35. Zhang, L.L., R. Zhou, and X. Zhao, *Graphene-based materials as supercapacitor electrodes*. Journal of Materials Chemistry, 2010. **20**(29): p. 5983-5992.
36. Wang, Y., et al., *Supercapacitor devices based on graphene materials*. The Journal of Physical Chemistry C, 2009. **113**(30): p. 13103-13107.
37. Yu, A., et al., *Ultrathin, transparent, and flexible graphene films for supercapacitor application*. Applied Physics Letters, 2010. **96**(25): p. 253105-253105-3.
38. Li, X., et al., *Transfer of large-area graphene films for high-performance transparent conductive electrodes*. Nano letters, 2009. **9**(12): p. 4359-4363.
39. Wang, D.-W., et al., *Electrochemical interfacial capacitance in multilayer graphene sheets: Dependence on number of stacking layers*. Electrochemistry Communications, 2009. **11**(9): p. 1729-1732.
40. Hu, L., et al., *Highly conductive paper for energy-storage devices*. Proceedings of the National Academy of Sciences, 2009. **106**(51): p. 21490-21494.

41. Kaempgen, M., et al., *Printable thin film supercapacitors using single-walled carbon nanotubes*. Nano letters, 2009. **9**(5): p. 1872-1876.
42. Hu, L., et al., *Stretchable, porous, and conductive energy textiles*. Nano letters, 2010. **10**(2): p. 708-714.
43. Peng, C., et al., *Carbon nanotube and conducting polymer composites for supercapacitors*. Progress in Natural science, 2008. **18**(7): p. 777-788.
44. Lee, S.W., et al., *Carbon nanotube/manganese oxide ultrathin film electrodes for electrochemical capacitors*. ACS nano, 2010. **4**(7): p. 3889-3896.
45. Hou, Y., et al., *Design and synthesis of hierarchical MnO<sub>2</sub> nanospheres/carbon nanotubes/conducting polymer ternary composite for high performance electrochemical electrodes*. Nano letters, 2010. **10**(7): p. 2727-2733.
46. Fan, L.-Z. and J. Maier, *High-performance polypyrrole electrode materials for redox supercapacitors*. Electrochemistry communications, 2006. **8**(6): p. 937-940.
47. Carlberg, J. and O. Inganäs, *Poly (3, 4-ethylenedioxythiophene) as Electrode Material in Electrochemical Capacitors*. Journal of the Electrochemical Society, 1997. **144**(4): p. L61-L64.
48. Ryu, K.S., et al., *Poly (ethylenedioxythiophene)(PEDOT) as polymer electrode in redox supercapacitor*. Electrochimica acta, 2004. **50**(2): p. 843-847.
49. Hu, C.-C., et al., *Design and tailoring of the nanotubular arrayed architecture of hydrous RuO<sub>2</sub> for next generation supercapacitors*. Nano letters, 2006. **6**(12): p. 2690-2695.
50. Shinomiya, T., V. Gupta, and N. Miura, *Effects of electrochemical-deposition method and microstructure on the capacitive characteristics of nano-sized manganese oxide*. Electrochimica acta, 2006. **51**(21): p. 4412-4419.
51. Wu, M.-S., *Electrochemical capacitance from manganese oxide nanowire structure synthesized by cyclic voltammetric electrodeposition*. Applied Physics Letters, 2005. **87**(15): p. 153102-153102-3.
52. Chen, P.-C., et al., *Flexible and transparent supercapacitor based on InO nanowire/carbon nanotube heterogeneous films*. Applied Physics Letters, 2009. **94**: p. 043113.
53. Hu, L., H. Wu, and Y. Cui, *Printed energy storage devices by integration of electrodes and separators into single sheets of paper*. Applied Physics Letters, 2010. **96**(18): p. 183502-183502-3.
54. Lin, Y., G. Ehlert, and H.A. Sodano, *Increased interface strength in carbon fiber composites through a ZnO nanowire interphase*. Advanced Functional Materials, 2009. **19**(16): p. 2654-2660.
55. Qin, Y., X. Wang, and Z.L. Wang, *Microfibre–nanowire hybrid structure for energy scavenging*. Nature, 2008. **451**(7180): p. 809-813.
56. Wan, Q., et al., *Fabrication and ethanol sensing characteristics of ZnO nanowire gas sensors*. Applied Physics Letters, 2004. **84**(18): p. 3654-3656.
57. Weintraub, B., Y. Wei, and Z.L. Wang, *Optical Fiber/Nanowire Hybrid Structures for Efficient Three-Dimensional Dye-Sensitized Solar Cells*. Angewandte Chemie, 2009. **121**(47): p. 9143-9147.
58. Goldberger, J., et al., *ZnO nanowire transistors*. The Journal of Physical Chemistry B, 2005. **109**(1): p. 9-14.
59. Wang, Z.L. and J. Song, *Piezoelectric nanogenerators based on zinc oxide nanowire arrays*. Science, 2006. **312**(5771): p. 242-246.

60. Huggins, R., *Advanced batteries: materials science aspects*. 2008: Springer Science & Business Media.
61. Wu, H., et al., *Engineering empty space between Si nanoparticles for lithium-ion battery anodes*. Nano letters, 2012. **12**(2): p. 904-909.
62. Goodenough, J.B. and Y. Kim, *Challenges for rechargeable Li batteries*. Chemistry of Materials, 2009. **22**(3): p. 587-603.
63. Nitta, N., et al., *Li-ion battery materials: present and future*. Materials Today, 2015. **18**(5): p. 252-264.
64. Scrosati, B., *Recent advances in lithium ion battery materials*. Electrochimica Acta, 2000. **45**(15): p. 2461-2466.
65. Wakihara, M., *Recent developments in lithium ion batteries*. Materials Science and Engineering: R: Reports, 2001. **33**(4): p. 109-134.
66. Yoo, E.J., et al., *Large reversible Li storage of graphene nanosheet families for use in rechargeable lithium ion batteries*. Nano letters, 2008. **8**(8): p. 2277-2282.
67. Geim, A.K., *Graphene: status and prospects*. Science, 2009. **324**(5934): p. 1530-1534.
68. Si, Y. and E.T. Samulski, *Exfoliated graphene separated by platinum nanoparticles*. Chemistry of Materials, 2008. **20**(21): p. 6792-6797.
69. Fang, Y., et al., *Self-assembly of cationic polyelectrolyte-functionalized graphene nanosheets and gold nanoparticles: a two-dimensional heterostructure for hydrogen peroxide sensing*. Langmuir, 2010. **26**(13): p. 11277-11282.
70. Balandin, A.A., *Thermal properties of graphene and nanostructured carbon materials*. Nature materials, 2011. **10**(8): p. 569-581.
71. Meyer, J.C., et al., *The structure of suspended graphene sheets*. Nature, 2007. **446**(7131): p. 60-63.
72. Chen, S.Q. and Y. Wang, *Microwave-assisted synthesis of a Co<sub>3</sub>O<sub>4</sub>-graphene sheet-on-sheet nanocomposite as a superior anode material for Li-ion batteries*. J. Mater. Chem., 2010. **20**(43): p. 9735-9739.
73. Wu, Z.S., et al., *Graphene anchored with Co<sub>3</sub>O<sub>4</sub> nanoparticles as anode of lithium ion batteries with enhanced reversible capacity and cyclic performance*. Acs Nano, 2010. **4**(6): p. 3187-3194.
74. Wang, H., et al., *Mn<sub>3</sub>O<sub>4</sub>-Graphene Hybrid as a High Capacity Anode Material for Lithium Ion Batteries*. arXiv preprint arXiv:1009.3923, 2010.
75. Zhou, G., et al., *Graphene-wrapped Fe<sub>3</sub>O<sub>4</sub> anode material with improved reversible capacity and cyclic stability for lithium ion batteries*. Chemistry of Materials, 2010. **22**(18): p. 5306-5313.
76. Arico, A.S., et al., *Nanostructured materials for advanced energy conversion and storage devices*. Nature materials, 2005. **4**(5): p. 366-377.
77. Sakamoto, J.S. and B. Dunn, *Hierarchical battery electrodes based on inverted opal structures*. Journal of Materials Chemistry, 2002. **12**(10): p. 2859-2861.
78. Liu, J., et al., *Carbon/ZnO nanorod array electrode with significantly improved lithium storage capability*. The Journal of Physical Chemistry C, 2009. **113**(13): p. 5336-5339.
79. Padmanathan, N. and S. Selladurai, *Shape controlled synthesis of CeO<sub>2</sub> nanostructures for high performance supercapacitor electrodes*. RSC Adv., 2014. **4**(13): p. 6527-6534.
80. Li, C., et al., *Controllable preparation and properties of composite materials based on ceria nanoparticles and carbon nanotubes*. Journal of Solid State Chemistry, 2008. **181**(10): p. 2620-2625.

81. Shuvo, M.A.I., et al., *Investigation of modified graphene for energy storage applications*. ACS Applied Materials & Interfaces, 2013.
82. Jian, L., et al., *Review of electrochemical capacitors based on carbon nanotubes and graphene*. Graphene, 2012. **2012**.
83. Li, J., et al., *Review of Electrochemical Capacitors Based on Carbon Nanotubes and Graphene*. 2012.
84. Marcano, D.C., et al., *Improved synthesis of graphene oxide*. ACS nano, 2010. **4**(8): p. 4806-4814.
85. Kumar, A., A.R. Madaria, and C. Zhou, *Growth of aligned single-crystalline rutile TiO<sub>2</sub> nanowires on arbitrary substrates and their application in dye-sensitized solar cells*. The Journal of Physical Chemistry C, 2010. **114**(17): p. 7787-7792.
86. Maensiri, S., et al., *Egg white synthesis and photoluminescence of platelike clusters of CeO<sub>2</sub> nanoparticles*. Crystal growth & design, 2007. **7**(5): p. 950-955.
87. Burroughs, P., et al., *Satellite structure in the X-ray photoelectron spectra of some binary and mixed oxides of lanthanum and cerium*. Journal of the Chemical Society, Dalton Transactions, 1976(17): p. 1686-1698.
88. Škoda, M., et al., *Sn interaction with the CeO<sub>2</sub> (111) system: Bimetallic bonding and ceria reduction*. Applied Surface Science, 2008. **254**(14): p. 4375-4379.
89. Chen, Y.-C., et al., *Highly flexible supercapacitors with manganese oxide nanosheet/carbon cloth electrode*. Electrochimica Acta, 2011. **56**(20): p. 7124-7130.
90. Arul, N.S., et al., *Fabrication of CeO<sub>2</sub>/Fe<sub>2</sub>O<sub>3</sub> composite nanospindles for enhanced visible light driven photocatalysts and supercapacitor electrodes*. Journal of Materials Chemistry A, 2015. **3**(29): p. 15248-15258.
91. Lang, X., et al., *Nanoporous metal/oxide hybrid electrodes for electrochemical supercapacitors*. Nature Nanotechnology, 2011. **6**(4): p. 232-236.
92. Wu, Z., et al., *Electrostatic induced stretch growth of homogeneous  $\beta$ -Ni (OH)<sub>2</sub> on graphene with enhanced high-rate cycling for supercapacitors*. Scientific reports, 2014. **4**.
93. Stoller, M.D. and R.S. Ruoff, *Best practice methods for determining an electrode material's performance for ultracapacitors*. Energy & Environmental Science, 2010. **3**(9): p. 1294-1301.
94. Lin, Y., et al., *Superhydrophobic functionalized graphene aerogels*. ACS applied materials & interfaces, 2011. **3**(7): p. 2200-2203.
95. Moon, I.K., et al., *Reduced graphene oxide by chemical graphitization*. Nature communications, 2010. **1**: p. 73.
96. Yang, T., et al., *Cyanobacterium metallothionein decorated graphene oxide nanosheets for highly selective adsorption of ultra-trace cadmium*. Journal of Materials Chemistry, 2012. **22**(41): p. 21909-21916.
97. Pang, H. and C. Chen, *Facile synthesis of cerium oxide nanostructures for rechargeable lithium battery electrode materials*. RSC Advances, 2014. **4**(29): p. 14872-14878.
98. Cui, L.-F., et al., *Carbon– silicon core– shell nanowires as high capacity electrode for lithium ion batteries*. Nano Letters, 2009. **9**(9): p. 3370-3374.
99. Liu, H., et al., *Highly ordered mesoporous NiO anode material for lithium ion batteries with an excellent electrochemical performance*. Journal of Materials Chemistry, 2011. **21**(9): p. 3046-3052.
100. Jiang, C., E. Hosono, and H. Zhou, *Nanomaterials for lithium ion batteries*. Nano Today, 2006. **1**(4): p. 28-33.

101. Shuvo, M.A.I., et al. *High-performance porous carbon/CeO<sub>2</sub> nanoparticles hybrid supercapacitors for energy storage*. in *SPIE Smart Structures and Materials+ Nondestructive Evaluation and Health Monitoring*. 2015. International Society for Optics and Photonics.
102. Shuvo, M.A.I., et al., *Microwave exfoliated graphene oxide/TiO<sub>2</sub> nanowire hybrid for high performance lithium ion battery*. *Journal of Applied Physics*, 2015. **118**(12): p. 125102.



## **Vita**

Mohammad Arif Ishtiaque Shuvo was born on 7th May 1987 in Khulna, Bangladesh. He is the second child of Mr. Mohammad Zuadul Karim Shapan and Mrs. Shahana Karim. He is married to Ms. Antara Badhan. Mr. Shuvo completed his high school from Comilla Cadet College, Bangladesh in 2005. Mr. Shuvo earned his Bachelor's Degree in Mechanical Engineering from Islamic University of Technology in 2009. He obtained his Masters degree in Mechanical Engineering in 2012 from UTEP. His thesis was titled "Graphene Structures for Energy Storage Applications". In spring 2013, he enrolled in the Engineering Doctoral program working towards his PhD in Energy Science. While pursuing his degree, he worked under direct supervision of Dr. Yirong Lin for developing unique architectural electrode materials for next generation energy storage devices by optimizing the performance and lifetime of the device. His dissertation title is "Hybrid Nano-structures for Enhanced Energy Storage Devices". In addition, his research focused on energy storage has been published in several peer reviewed journals, conference papers, and book chapters. During his degree, He received Alternate Sponsor Fellowship from Pacific Northwest National Laboratory and George A. Khutilek Memorial Graduate Fellowship from UTEP graduate school. He is going to join Intel Corporation as a Process TD Engineer.

Permanent address: 32 G.N. Bank Road  
Khulna, Bangladesh, 9100

This dissertation was typed by Mohammad Arif Ishtiaque Shuvo.